# Earth Observing-1 Advanced Land Imager : Imaging Performance On-Orbit

D.R. Hearn

31 December 2002

## Lincoln Laboratory

MASSACHUSETTS INSTITUTE OF TECHNOLOGY

*LEXINGTON, MASSACHUSETTS*

20030220 044

The ESC Public Affairs Office has reviewed this report, and it is releasable to the National Technical Information Service, where it will be available to the general public, including foreign nationals.

This technical report has been reviewed and is approved for publication.

FOR THE COMMANDER

Gary Tutungian
Administrative Contracting Officer
Plans and Programs Directorate
Contracted Support Management

# ABSTRACT

This report analyzes the on-orbit imaging performance of the Advanced Land Imager (ALI) on the Earth Observing-1 satellite. The pre-flight calibrations are first summarized. The methods used to reconstruct and geometrically correct the image data from this push-broom sensor are described. The method used here does not refer to the position and attitude telemetry from the spacecraft. Rather, it is assumed that the image of the scene moves across the focal plane with a constant velocity, which can be ascertained from the image data itself. Next, an assortment of the images so reconstructed is presented. Color images sharpened with the 10-m panchromatic band data are shown, and the algorithm for producing them from the 30-m multispectral data is described.

The approach taken for assessing spatial resolution is to compare the sharpness of features in the on-orbit image data with profiles predicted on the basis of the pre-flight calibrations. A large assortment of bridge profiles is analyzed, and very good fits to the predicted shapes are obtained. Lunar calibration scans are analyzed to examine the sharpness of the edge-spread function at the limb of the moon. The darkness of the space beyond the limb is better for this purpose than anything that could be simulated on the ground. From these scans, we find clear evidence of scattering in the optical system, as well as some weak ghost images. Scans of planets and stars are also analyzed. Stars are useful point sources of light at all wavelengths, and delineate the point-spread functions of the system. From a quarter-speed scan over the Pleiades, we find that the ALI can detect 6th magnitude stars.

The quality of the reconstructed images verifies the capability of the ALI to produce Landsat-type multispectral data. The signal-to-noise and panchromatic spatial resolution are considerably superior to those of the existing Landsat sensors. The spatial resolution is confirmed to be as good as it was designed to be. In addition, these results indicate that the pre-flight spatial calibrations provided a full and accurate description of the imaging properties of the instrument.

**This Page Intentionaly
Left Blank**

# ACKNOWLEDGMENTS

**This Page Intentionaly
Left Blank**

# TABLE OF CONTENTS

**This Page Intentionaly
Left Blank**

# LIST OF ILLUSTRATIONS

# LIST OF ILLUSTRATIONS
## (Continued)

**Figure
No.**

**Page**

# LIST OF ILLUSTRATIONS
## (Continued)

# LIST OF ILLUSTRATIONS
## (Continued)

# LIST OF ILLUSTRATIONS
## (Continued)

**Figure**
**No.**                                                                                              **Page**

**This Page Intentionaly
Left Blank**

# LIST OF TABLES

xv

# 1. INTRODUCTION

The Advanced Land Imager (ALI) is the primary instrument aboard the Earth Observing–1 (EO-1) spacecraft of NASA's New Millennium Program. Its purpose is to validate advanced technologies for the acquisition of multispectral images of the earth consistent with the requirements of the Landsat program. The ALI is a push-broom imaging system, with nine multispectral bands at a ground-sampling distance (GSD) of 30 meters, and a Panchromatic band with a 10 m GSD. For a full description of the ALI instrument, see Bicknell, et al. (1999)[1, 2].

EO-1 was successfully launched on November 21, 2000. It was soon orbiting "in formation" with Landsat-7, passing over the same points on the earth one minute later than Landsat-7. Since November 26, 2000, the ALI has been acquiring images from orbit. The typical Data Collection Event (DCE) includes 24 seconds of image data. For the first year on-orbit, approximately eight DCE's occured per day.

The ALI was extensively calibrated at Lincoln Laboratory prior to launch. In particular, the imaging performance of the instrument with respect to spatial resolution and detector lines of sight have been reported by Hearn [3, 4].

This report describes the post-launch spatial resolution performance of the ALI. The method chosen to assess this performance is to compare on-orbit image data with what can be predicted for those data from the pre-launch measurements. The following sections first summarize the pre-launch calibrations. Our procedures for processing the on-orbit image data are described in the next section. The main analyses of imaging performance are presented in sections describing bridge profiles, lunar scans, and planetary and stellar scans. As will be seen by the concluding section, the imaging performance of the ALI has amply met all expectations for the instrument.

# 2. PRE-FLIGHT CALIBRATIONS

Prior to integration of the ALI with the EO-1 spacecraft, full performance calibrations of the instrument were performed at Lincoln Laboratory. The instrument was in a thermal vacuum chamber, at nominal on-orbit operating conditions for these calibrations. In addition to end-to-end system measurements obtained in this way, subsystem measurements were employed in order to form the most complete estimates of all instrument calibration parameters.

Pre-launch imaging calibrations made use of an imaging collimator with a 3.2° field-of-view [5]. To estimate the spatial transfer functions (STF's a.k.a. MTF's) and point spread functions, knife edges were slowly scanned across the focal plane of the collimator in the horizontal and vertical directions (corresponding to cross-track and in-track directions on-orbit). The data sampling frequency provided approximately 70 samples across either the width or height of each detector scanned.

## 2.1 SPATIAL TRANSFER FUNCTIONS AND POINT-SPREAD FUNCTIONS

The knife-edge scans were performed across a large number of detectors within each spectral band and each sensor chip assembly (SCA). From the knife-edge scan data, spatial transfer functions were estimated as follows: First, the edge-scan profiles of all individual detectors were shifted to co-align the central edge crossing location. Next, a line-spread function (LSF) was derived for each detector by numerically differentiating the edge-spread functions. (This was done in the Fourier Transform domain, first filtering out spatial frequencies beyond the diffraction cutoff.) The Fourier Transform of the LSF is then a one-dimensional slice through the estimated two-dimensional STF. The one-dimensional STF was averaged for all of the valid detector data of each band and SCA combination.

A two-dimensional estimated wavefront error (WFE) for the ALI optical system had been formed, based on interferograms made with a laser unequal-path interferometer (LUPI). From the WFE model, and a model of each type of detector, a theoretical point-spread function (PSF) and STF was computed for each band and SCA combination of the knife-edge scans. A careful comparison of these theoretical STF's with the many STF estimates derived from the knife-edge scans led to a set of calibration parameters from which we derived our best pre-launch estimate of the STF of the complete instrument. Numerical values of the STF for each band, near the center of the detector array, are summarized in our report [3].

## 2.2 DETECTOR LINES-OF-SIGHT

Accurate reconstruction of images requires that the line of sight (LOS) of each detector be known. We break down the LOS problem into two parts, relative and absolute. The relative LOS relates each detector's LOS to those of all of the other detectors. The absolute part relates the detector LOS's to the

optical axes of the instrument, and those axes to the reference axes of the spacecraft and its attitude control system, mediated by a reference cube mirror on the instrument. Our pre-launch calibration estimated the LOS of each detector in relation to the ALI reference cube. From this information, we have been able to reconstruct *system-corrected* images from on-orbit data. It is beyond the scope of this work to produce geo-referenced images. To do so would require the application of position and attitude telemetry from the spacecraft, as well as knowledge of the geoid and digital elevation models of the earth.
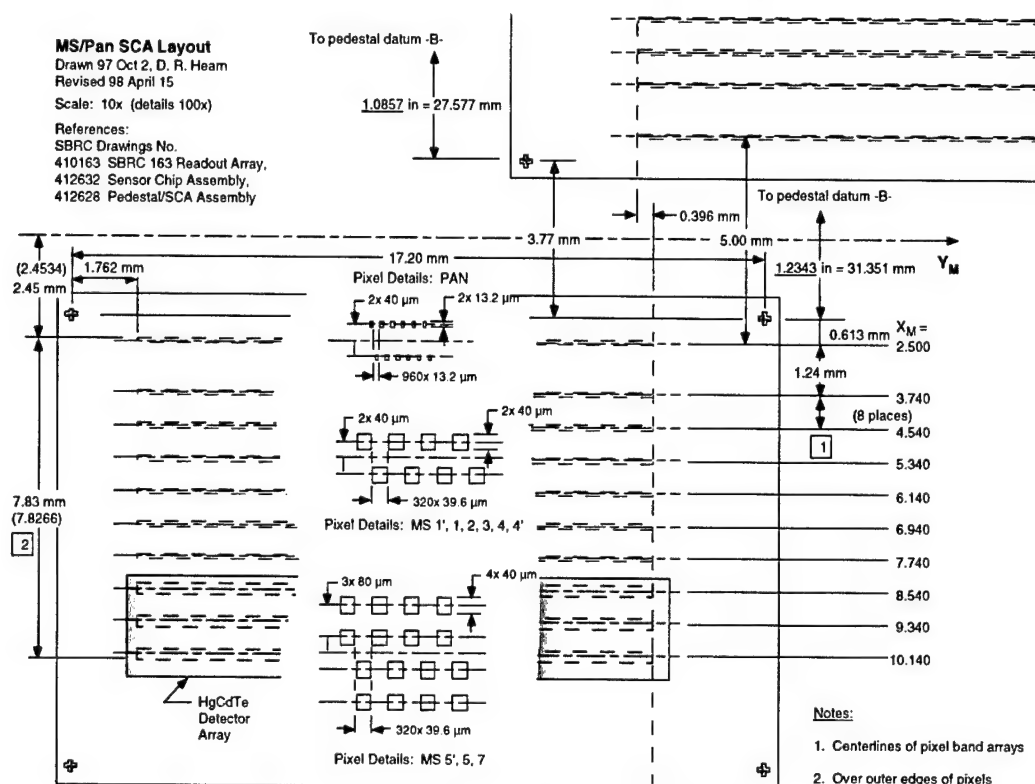


*Figure 1.  Arrangement of the ALI detectors on the focal plane.*

To estimate the relative lines of sight of the detectors, a Ronchi ruling target was placed at the focus of the collimator. Three static "images" of the ruling were obtained with the ALI, at Ronchi orientations of 0°, 60°, and 120°. These data were not two-dimensional images in the usual sense, but merely records of the optical intensity seen by each of the detectors staggered across the focal plane of the ALI. The problem can be better understood by examining Figure 1. A model of the LOS of each detector was constructed, using parameters to describe the position of the detector within the SCA, the location of the SCA on the focal plane, the focal length of the optical system, and the optical distortions of the system.

The recorded intensities in the images were fitted with intensities computed from the model, by adjusting the LOS parameter values.

The absolute LOS vectors were estimated from the relative LOS estimates, combined with theodolite measurements obtained by sighting through the optical system and to the ALI reference cube. As we reported previously [4], the LOS for each detector is contained in a data file, expressed as an apparent position on the focal plane, and an effective focal length of the optical system.

# 3. ON-ORBIT IMAGES OF EARTH

A clear subjective assessment of the quality of the images obtained from the ALI on-orbit is provided by visual examination of those images, once they have been reconstructed. Apart from a known problem of detector cross-talk (or "leaky pixels"), extensively discussed elsewhere [6, 7], the images are almost entirely free of noticeable artifacts. In this section, we describe the processing of the image data, from raw, level 0, through radiometrically corrected (level 1R), to system-corrected, re-sampled level 1G data. Following that, we show a number of representative browse images as evidence of the high quality of the ALI data. More quantitative assessments of the ALI imaging performance will be found in following sections.

## 3.1 IMAGE PROCESSING

At Lincoln Laboratory, processing of the ALI image data begins from the Level 0 data files, in Hierarchical Data Format (HDF), as received on tape from Goddard Space Flight Center (GSFC). Processing is done on either a Silicon Graphics workstation computer, or on a desktop computer. All developmental software has been written in IDL (Interactive Data Language). Processing a normal 24-second DCE, from Level 0 to JPEG browse images, requires approximately 15 to 20 minutes on the workstation and not much longer on a 500 MHz G4 Macintosh.

Data are also processed at GSFC through the radiometric calibration "pipeline," written in the C language at Lincoln Laboratory. One set of scene data takes approximately two minutes to go through this pipeline.

### 3.1.1 Radiometric Correction

Radiometric calibration of the image data is basically straightforward, once the calibration constants have been determined [6]. For each DCE, dark data are collected for short periods with the instrument aperture cover closed, before and after the image exposure. The dark readings for each detector are averaged, then these offsets are subtracted from the image data readings. Next, the image readings (in DN, or encoder steps) are multiplied by the radiometric response coefficients to yield Level 1R data, in radiometric units. The response coefficients were initially from the pre-flight calibration, but were subsequently updated from in-flight calibration data. The values are also multiplied by a scaling factor of 300, to permit them to be stored compactly in integer format without loss of information.

To simplify later processing, half of the data are shifted by whole numbers of frames, to align the parts of the images sampled by odd and even detectors. (The odd and even detectors are staggered on the focal plane by 80 $\mu$m in the case of the silicon detectors, and by up to 240 $\mu$m for the HgCdTe detectors.)

7

The radiometrically calibrated data are written to HDF files, one for each SCA. Each file contains the data for all bands.

The foregoing description is sufficient for 95% of the detector data. For band 3 of SCA 3, and band 2 of SCA 4 however, much more effort is needed to compensate for detector cross-talk. Also, for a handful of defective detectors, readings from neighboring detectors are substituted to suppress distracting artifacts. The radiometric calibration process is more fully discussed by Mendenhall [6, 7].

### 3.1.2 Image Speed Estimation

To reconstruct the image of the scene, the relative motion of the ALI lines of sight across the scene, or equivalently, the motion of the optical image across the focal plane, must be known. Knowing the current ALI frame rate, the relative motion per frame can be estimated from the spacecraft position and attitude data, recorded once per second in the telemetry data files.

For normal images however, we have taken a different approach which has worked quite well. We make the assumption that the image moves across the focal plane at a *constant velocity*. The nominal speed is 0.04 mm/frame (multispectral). The nominal direction is perpendicular to the detector rows (*i. e.* yaw angle zero). We take advantage of the fact that neighboring SCA's overlap by 10 multispectral and 30 panchromatic detectors. Hence there are three strips of the image that are sampled twice at different times. The image speed and yaw angle are estimated by maximizing the cross-correlation between those successive samples. Those image speed and yaw estimates are then inputs to the re-sampling procedure.

### 3.1.3 Geometric Re-sampling

The first step in the construction of a Level 1G image from Level 1R data is to reverse any integral-frame shifts that may have been applied up to that point. Geometric re-sampling starts from detector samples that are synchronous in time. Next, the detector line-of-sight data is read into memory from the LOS calibration parameter file [4]. A destination image array, either multispectral or panchromatic, is created for each SCA. For each pixel in the destination image array, a corresponding detector, frame coordinate in the source image data array is computed from the detector LOS, image speed, and yaw parameters. Extra rows of fill data are provided at the beginning and end of the destination arrays, to allow for the different in-track placements of the various bands and SCA's.

The re-sampling is done in two steps; first, in the in-track ($X$, or frame) coordinate, then in the cross-track ($Y$, or detector) coordinate. The first step takes care of the separation of odd and even detectors and SCA's in the $X$ direction. That separation prohibits a simple one-step bilinear interpolation. Either linear or cubic spline interpolations may be used. This two-step procedure works well in this case, since the output image coordinates are practically parallel to the input data coordinates. The procedure would not work so well if the output image were significantly rotated, however.

8

As with the Level 1R processing, a separate Level 1G output file is written in HDF format for each SCA. The multispectral files contain the co-registered image data for all nine MS bands.

### 3.1.4 Browse Image Creation

To make the re-sampled images more accessible for viewing and printing, special browse images are created from the Level 1G files. The browse images of multispectral data are made from any three selected spectral bands to be mapped into the 24-bit RGB color space of computer displays. Panchromatic browse images are simply 8-bit gray-scale data. The user can include all of the data from the DCE, or a selected range of frames. In each case, the Level 1G files of all four SCA's are read. We combine them by omitting five MS (or 15 Pan) edge pixels from each of two neighboring SCA's in the abutted browse image. If the speed and yaw parameters have been accurately estimated, we find that the transition from one SCA to the next is rarely discernable in the browse image. This testifies to the accuracy of both the geometric and the radiometric calibrations.

A set of expected radiance ranges in each of the bands is an input to the browse image procedure. These are intended to represent the minimum and maximum scene radiance in each spectral band. The output levels are scaled from 0 to 255 as follows: Output is proportional to the logarithm of the ratio between input radiance and minimum radiance. The proportionality is adjusted to output 255 at maximum radiance. Thus we attempt to preserve the full dynamic range, but enhance contrast at the low radiances. This is usually referred to as "gamma correction."

The browse images are written to output files in either JPEG or TIFF format. These files can be opened in standard image-editing programs, such as Adobe PhotoShop. In that program, the user can easily zoom in and out, pan, scroll, and select regions of interest. From such a program, the image can be printed, within the limitations of the printer.

PhotoShop has good facilities for adjusting the color balance, brightness, contrast, etc. of the image. In order to produce true-color images with a minimum of guesswork, ranges of in-band radiance have been computed in MODTRAN for a set of solar zenith angles and surface reflectances. Given the zenith angle and a range of reflectances for a DCE, an IDL procedure returns the radiance range array to use as input to the browse image procedure. Using a maximum reflectance of 40%, and moving the minimum radiance to 80% of the zero-reflectance value, we usually find that the browse image shows the full range of reflected radiances, without saturation or clipping at either end. This practice compensates for atmospheric path radiance. The maximum reflectance level could be set higher, in order to capture details of cloud formations, but we are usually most interested in land details. Finally, in PhotoShop, the "Image > Adjust > Levels…" dialog can be used to stretch the output ranges to produce the desired brightness, contrast, and color balance. Normally, only the top and bottom "RGB" limits need to be adjusted.

## 3.2 SAMPLE IMAGES

In this section we attempt to show a small selection of browse images from ALI observations. Limitations of the small paper format and the reproduction process preclude a full appreciation of the depth and resolution of the ALI images from this report. The typical multispectral ALI image is 1250 pixels wide by 5400 pixels long, in 9 bands. In the 6.5 x 8 inch space of this page, we can show less than 10% of a scene at 100 pixels per inch. Nevertheless, we can show samples of the images to convey an idea of their quality.

### 3.2.1 Oahu

Early in the EO-1 mission, the ALI scanned over the middle of the island of Oahu, Hawaii. In Figure 2, we show a multispectral browse image of the island, where red, green, and blue (RGB) represent bands 3, 2, and 1, respectively. Since those bands approximate the red, green, and blue of human vision, we call this a "true color" image, though we do not warrant the reproduced colors to be photometrically accurate! The multispectral image resolution is 30 m. A portion of the panchromatic (10 m resolution) image, showing Pearl Harbor, is seen in Figure 3.

*Figure 2. True-color ALI image of Oahu, acquired 19 December 2000.*

11

*Figure 3. Panchromatic image of Pearl Harbor, from the same DCE as Figure 2.*

### 3.2.2  Washington, D. C.

Another panchromatic image, taken by the ALI on 1 December 2000, shows the central area of Washington, D. C. (Figure 4). The area shown is approximately 11 km across.

12

*Figure 4. Panchromatic ALI image of Washington, D. C., acquired 1 December 2000.*

### 3.2.3  Cape Canaveral

A portion of the ALI multispectral image of Cape Canaveral, Florida is shown in Figure 5. The spectral bands shown here are 4, 3, and 2 for red, green, and blue. (For brevity, we refer to it as a "4-3-2" image.) Since chlorophyll strongly reflects the near-infrared of band 4, healthy vegetation appears red in 4-3-2 images. This is a presentation very frequently used for Landsat images.

13

*Figure 5. False-color(4, 3, 2) ALI image of Cape Canaveral, Florida, acquired 13 January 2001.*

### 3.2.4  Yuma, Arizona

In Figure 6 we show a portion of the true-color (3-2-1) image of Yuma, Arizona, acquired on 23 January 2001. It shows many green fields where vegetables are grown through the winter. It also shows the Colorado River and the Imperial Canal taking water to the Imperial Valley of California.

*Figure 6. True-color ALI image of Yuma, Arizona, acquired 23 January 2001.*

### 3.2.5 Lake Frome, Australia

In Figure 7, we present images of Lake Frome, South Australia in several different band selections. In the true-color image (bands 3-2-1), the dry lake bed appears in very light shades of gray. The SWIR bands 7-5-5' however, show dramatic variations as shades of blue, probably indicating the presence of water just below the surface [8].



*Figure 7. Multispectral images of Lake Frome, South Australia. The spectral bands represented by red, green, and blue, respectively, are indicated at the top of each image*

### 3.2.6 Southern Alps, New Zealand

The unusual image seen partially in Figure 8 is a 7-4-2 image over the South Island of New Zealand. It shows parts of the Rolleston Range, Lake Coleridge, and the Rakaia River. In this presentation, snow on the mountain peaks appears light blue, while clouds near the peaks are white. Vegetation is light green.

*Figure 8. False-color (7, 4, 2) ALI image of the Southern Alps, South Island, New Zealand, acquired 10 January 2001.*

### 3.2.7 New York City

A false-color (4-3-2) image of New York City, taken 14 April 2001, appears in Figure 9. It shows many bridges, which we have used to analyze the on-orbit image sharpness (see Section 4).

*Figure 9. False-color(4-3-2) ALI image of New York City, acquired 14 April 2001.*

## 3.3 PAN-SHARPENED COLOR IMAGES

The panchromatic (Pan) band basically spans the visual spectral range, as do multispectral (MS) bands 1, 2, and 3. We can take advantage of the fact that our visual perceptions are much more sensitive to brightness changes than color changes to produce Pan-sharpened color images, with a ground sampling distance (GSD) of 10 meters. These are also called "10-m color" images. This is similar to the approach taken in NTSC television, in which the *chroma* signal is transmitted with much less resolution than the *luma* signal.

In order to achieve the maximum resolution for the 10-m color images, we begin with Level 1R non-resampled data. For computational efficiency, only the data from a selected range of SCA's and frames are processed. The MS bands 1, 2, and 3 are first frame-shifted to achieve approximate band-to-band registration. Next, they are up-sampled to 10 m resolution to match the Pan data. Edge features of these three MS bands and the Pan band are found by the application of a Sobel filter. The band and SCA registrations are fine-tuned by shifting pixels by 10 m (ground) increments to find the highest cross-correlation of the edge images.

Once the bands are registered as well as they can be, a 24-bit RGB image is formed from the MS bands, in the same fashion as for the usual browse images (see Section 3.1.4). It is then converted to the HSV (hue, saturation, value) color space. The value array is then replaced with one formed from the Pan image. The full color image is then converted back to the RGB color space, and written to a file in TIFF format. This image has the full spatial resolution of the Pan image, though the hue and saturation of the pixels derive from the 30 m MS image. The TIFF format is used for output to avoid the artifacts that can result from the lossy JPEG compression.

Some examples of Pan-sharpened ALI images produced as described here are seen in the following figures. Figure 10 is a small section of the image in Figure 6. Figure 11 is a color version of Figure 3. To show the level of detail in this image, an enlarged portion is shown in Figure 12. Numerous airplanes can be found in this image. The battleship Missouri and the Arizona Memorial can also be recognized. In Figure 13, we show the airport at Kandahar, Afghanistan, on 9 October, 2001. The black spots on the runway and taxiway are bomb craters.

*Figure 10.  Pan-sharpened image of Yuma Arizona.*

23

*Figure 11. Pan-sharpened image of Pearl Harbor.*

*Figure 12. Enlargement of a portion of Figure 11.*

*Figure 13. Pan-sharpened image of the airport at Kandahar, Afghanistan, on 9 October, 2001.*

# 4. BRIDGE PROFILES

## 4.1 ANALYSIS PROCEDURE

Images of bridges are useful for testing the spatial resolution of the instrument. They are usually straight, narrow strips, with uniformly dark water on either side. If the true ground scene is simple enough, we can model the radiance distribution as a set of parallel, uniform stripes. The response of the instrument to such a simple scene is easy to calculate from the calibrated spatial transfer function (STF, Section 2.1). This expected response is then compared with the actual response in the scene data to validate the on-orbit imaging performance. The starting point for these analyses is the radiometrically-calibrated, but not re-sampled, Level 1R data.

To analyze an image of a bridge, we first select a rectangular region of interest (ROI) around the bridge that shows parallel regions of nearly-uniform radiance. The sides of the rectangle are parallel and perpendicular to the axis of the bridge. Within this region, the radiance readings in the Level 1R data are mapped into rotated coordinates aligned with the bridge. Since bridges appear at random orientation angles in the images, this generally provides a set of radiance samples closely spaced in the direction perpendicular to the bridge axis. As an example, the white outline seen in Figure 14 is the ROI to be analyzed.
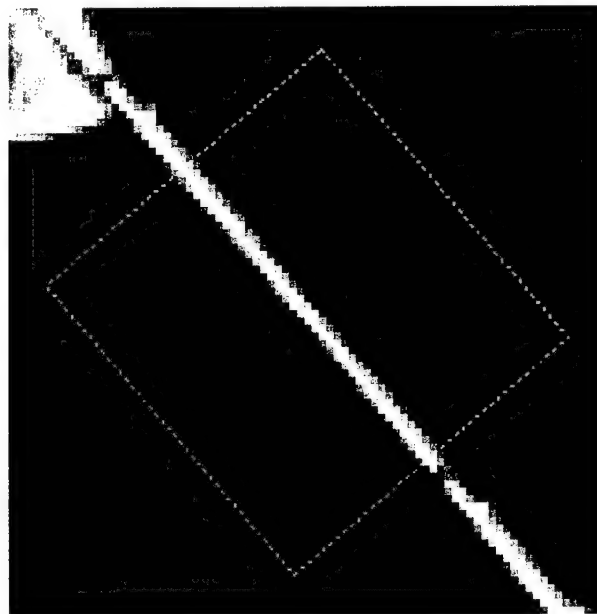


*Figure 14. Rectangular region of interest across the Bronx Whitestone bridge, New York City, in the Pan image acquired 20 March 2001.*

27

We fit the observed radiance profile with an expected system response as follows. The scene radiance profile within the ROI is modeled as a step function. The dynamic spatial transfer function (DSTF) is computed from the calibrated static STF by multiplying the static STF by a sinc function in the scan direction to account for the image motion during the frame integration time [see 3, p. 15]. A one-dimensional slice of the DSTF in the direction perpendicular to the bridge axis is interpolated from the two-dimensional DSTF. This interpolation is done with fine enough sampling to ensure full coverage of the spatial data range when inverse-transformed. The one-dimensional dynamic STF is multiplied by the Fourier Transform of the radiance step function, and the result is inverse-transformed to yield the expected response profile. (This is equivalent to convolving the radiance step function with the instrument line-spread function.)

The foregoing calculations are performed in an iterative process, which begins with a manual estimate of the angle of the bridge, the radiances and relative focal plane step locations in the profile. This set of parameters is iteratively adjusted to minimize the mean squared difference between the raw profile data and the expected profile. This process invokes the "CURVEFIT" linearized least-squares (Levenberg-Marquardt) procedure of IDL.

The fitting is actually done in two passes. Initially, all of the detector samples (pixels) in the ROI are fitted. Using the resulting model parameters, upper and lower limit functions are computed. The limit functions represent the expected response, shifted up or down by five times the noise-equivalent radiance level, and left or right by 0.3 times the detector width. Next, pixels whose radiance values are within the limits band are identified as "good." The fitting process is repeated, using only the "good" pixel subset within the ROI.

## 4.2   RESULTS OF FITTING

Figure 15 shows the Pan radiance profile of the Bronx Whitestone Bridge corresponding to the ROI shown in Figure 14, as crosses for the individual readings. The red curve is the expected response of the ALI Pan band to the fitted step-function radiance model, shown by the green dotted lines. In this case, the high bridge radiance is followed by a lower radiance, representing the shadow of the bridge on the water. The pixels outside the "good" band are shown as green diamonds. The relative projected area of a single detector across the bridge axis is indicated by the dashed trapezoid.
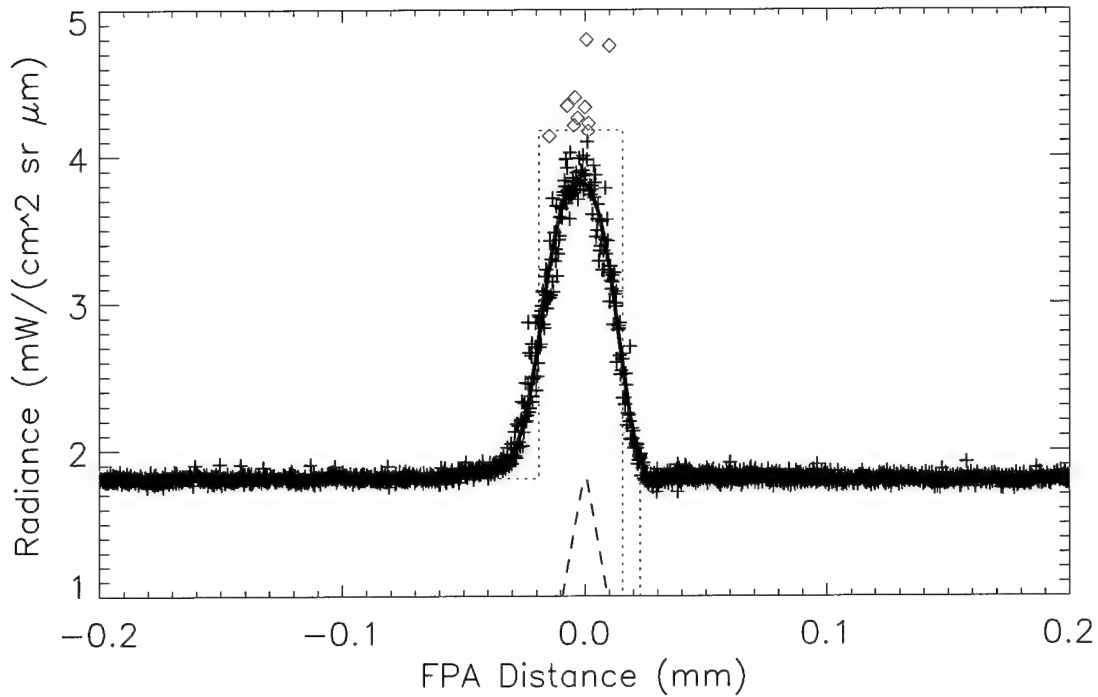
28

*Figure 15. Fitted Pan profile of the Bronx Whitestone bridge, as seen in Figure 14.*

Fitted profiles of the same bridge for bands 3 and 5 are shown in Figure 16 and Figure 17, respectively. These results are fully representative of the VNIR and SWIR multispectral (MS) band fits for this bridge observation. The shadow observable in the Pan band is too narrow to be seen or fitted in the MS bands. In addition to that, the water is very dark to begin with for the longer wavelengths.

Qualitatively, the computed spatial response of the ALI appears to provide an excellent fit to the observed radiance samples for this bridge observation. The $\chi^2$ value indicated by `curvefit` for the Pan band was 1.82, for 2,380 degrees of freedom (DOF). For bands 3 and 5, we found $\chi^2$ values of 1.11 (260 DOF) and 0.78 (261 DOF). We do not ascribe great significance to these $\chi^2$ values, or to the formal parameter errors also returned by `curvefit`. Those values are only as good as the estimate of noise that was made prior to the fitting. The noise estimates were based on dark noise observed during a single data collection, and represent averages over an entire SCA in each band. They do not take into account possible spatial noise arising from focal plane contamination.
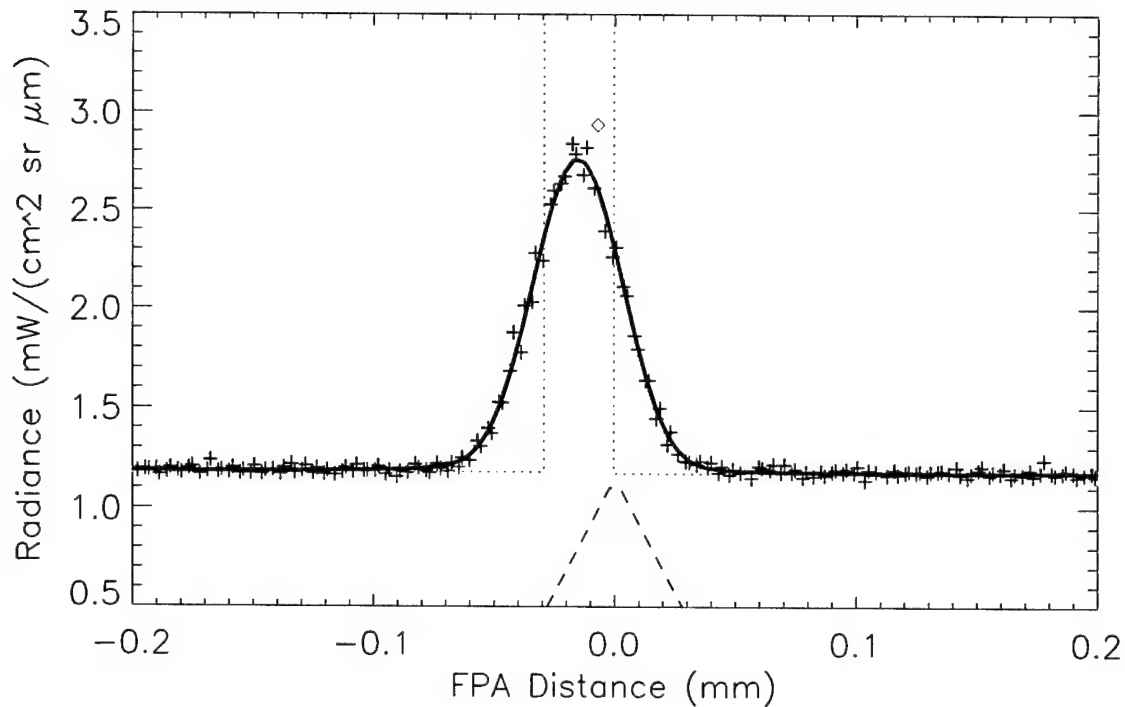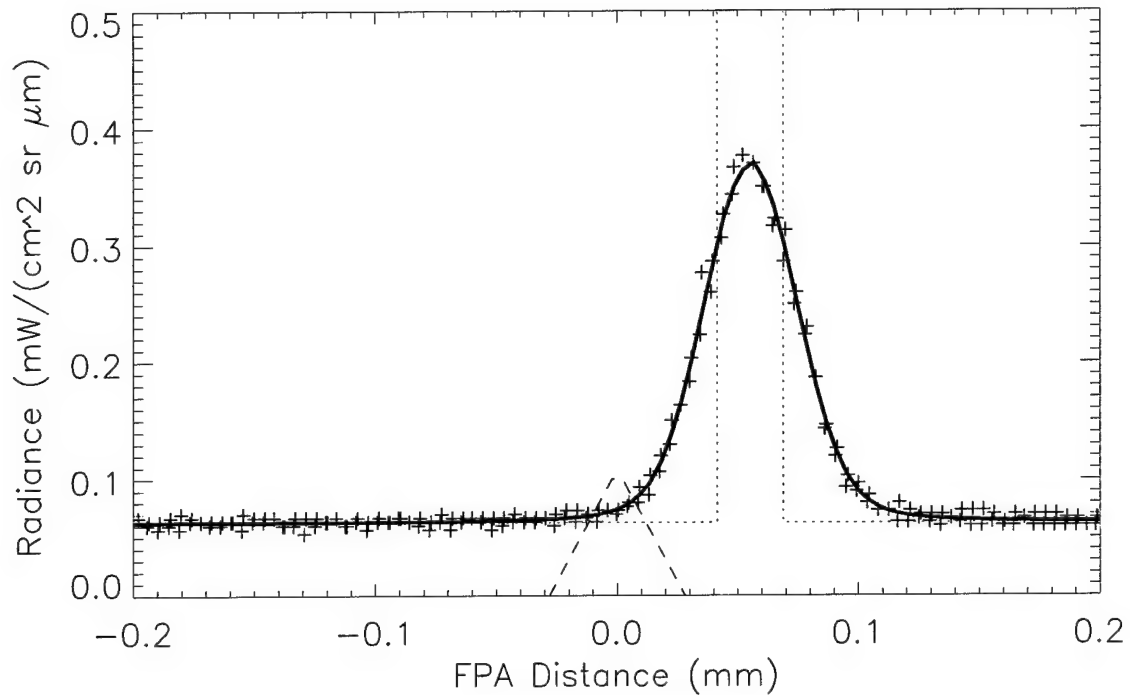
*Figure 16. Fitted profile of the Bronx Whitestone bridge in band 3.*

The angle between the axis of the Bronx Whitestone Bridge and the scan axis (ground track) of the ALI was 40.13°. The apparent width of the bridge image on the focal plane was 34.62 ± 0.13 μm. The bridge image crossed SCA 1. At a nominal slant range of 711 km, and with the ALI focal length of 942.76 mm, the corresponding width of the bridge is 26.11 m (85 ft 8 in). The reported width of this 6-lane bridge is 77 feet (see http://www.nycroads.com/crossings/bronx-whitestone/). It is not clear whether the 77 feet is the overall width, or just the roadway width. In any case, the 9-foot difference is only one third of one Pan pixel. Widths and angles fitted for the MS bands are consistent with the Pan result, but less precise because of the larger detectors. Very similar results were obtained for a second observation of New York City on 2001 April 14.

Finally, the apparent overall position shift from one band to another is under investigation. It may be an artifact produced by the software that extracted the subset of data near the bridge. It could also be the result of an error in the frame (sampling) rate, which was supposed to be set so that a given ground point would be sampled in successive bands exactly 20 frames apart. Finally, it could be caused by relative optical distortion from one band to another.

*Figure 17. Fitted profile of the Bronx Whitestone bridge in band 5.*

The cloud-free observations of New York City on 2001 March 20 and April 14 provide a wealth of opportunities to fit bridge profiles in different SCA's and at different angles to the track. The fits to the Bronx Whitestone Bridge just described were for SCA 1. In Figure 18 we show the image of the Earle Naval Pier in SCA 2 from the same March 20 DCE. This pier structure extends approximately 3.5 km into Sandy Hook Bay from the New Jersey shore. The pier is at 13.24° from the EO-1 track. A simple fit to the Pan data for the two main features in the ROI of Figure 18 is presented in Figure 19. Only two stripes of elevated radiance above the background water were assumed. The $\chi^2$ value of 2.75 for 4,048 DOF might be improved if shadow stripes were used as well. Nevertheless, the fit looks very good as is.

31
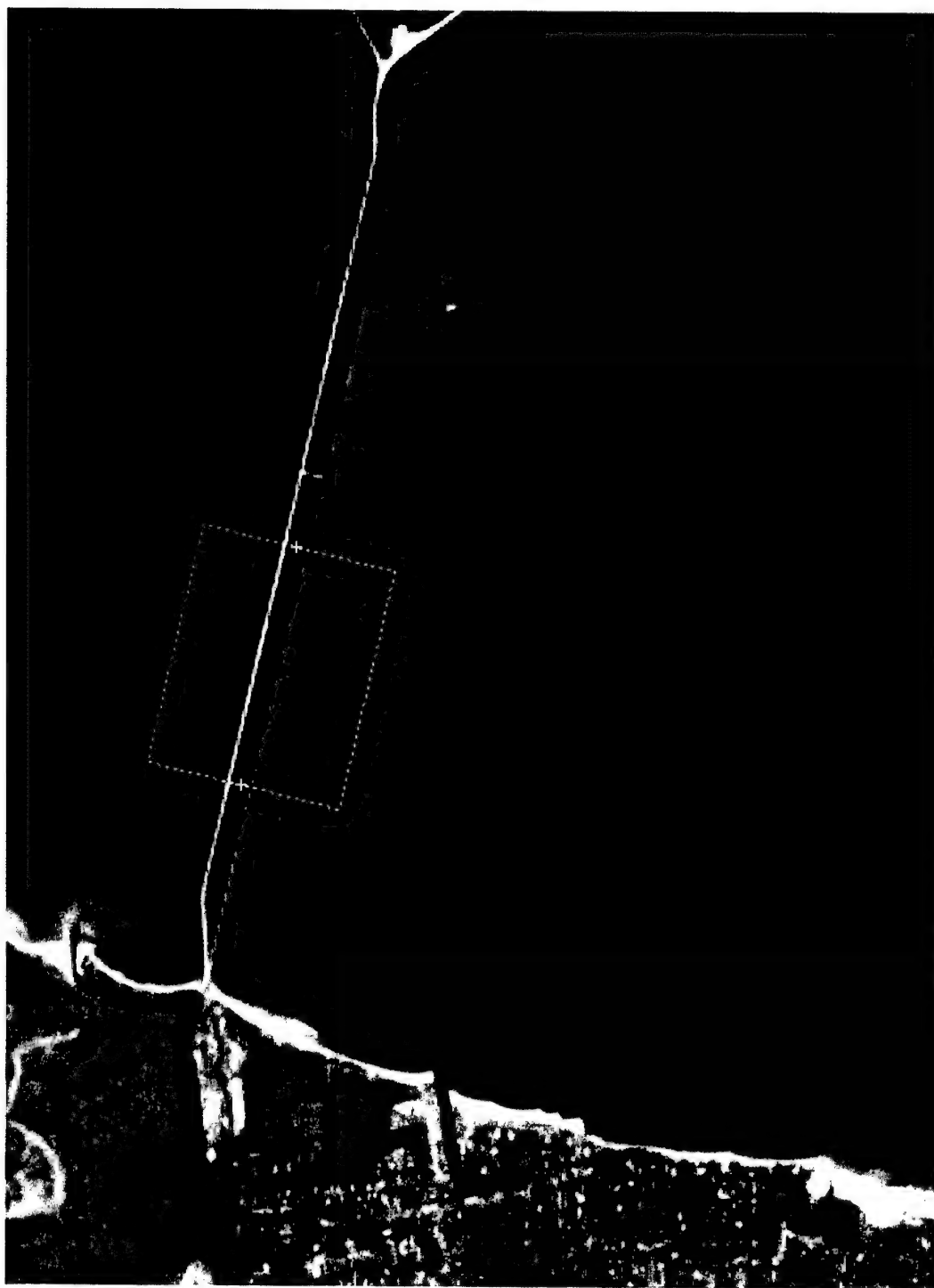
*Figure 18. Panchromatic image of the Earle Naval Pier, Sandy Hook Bay, observed 2001 March 20.*
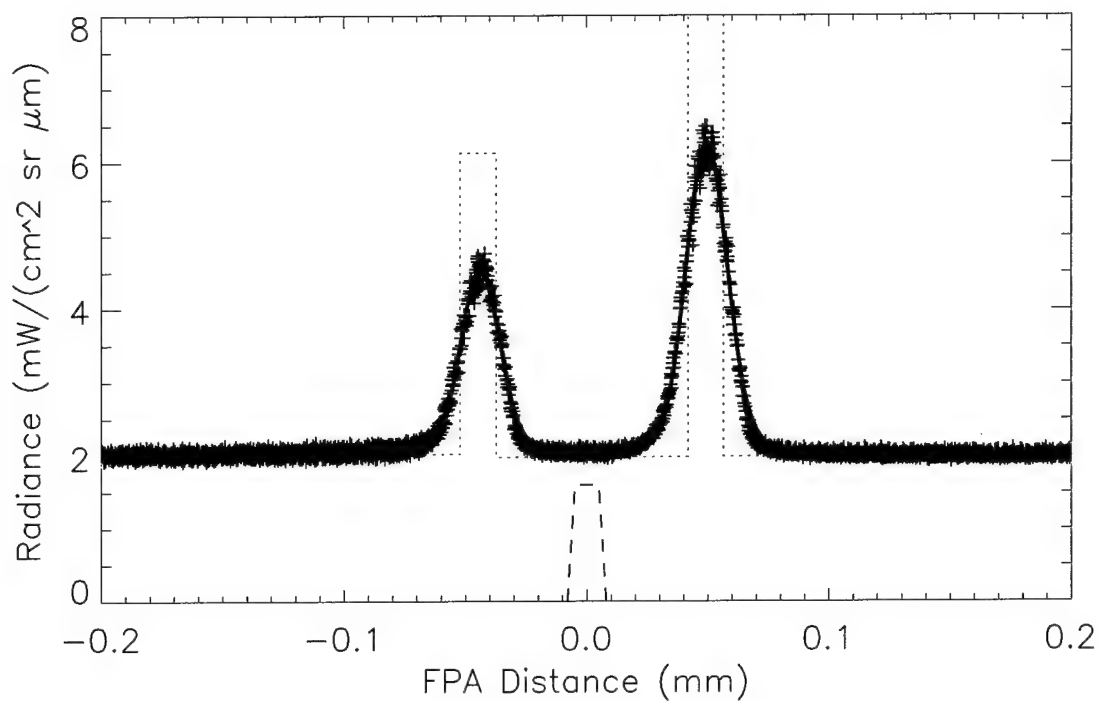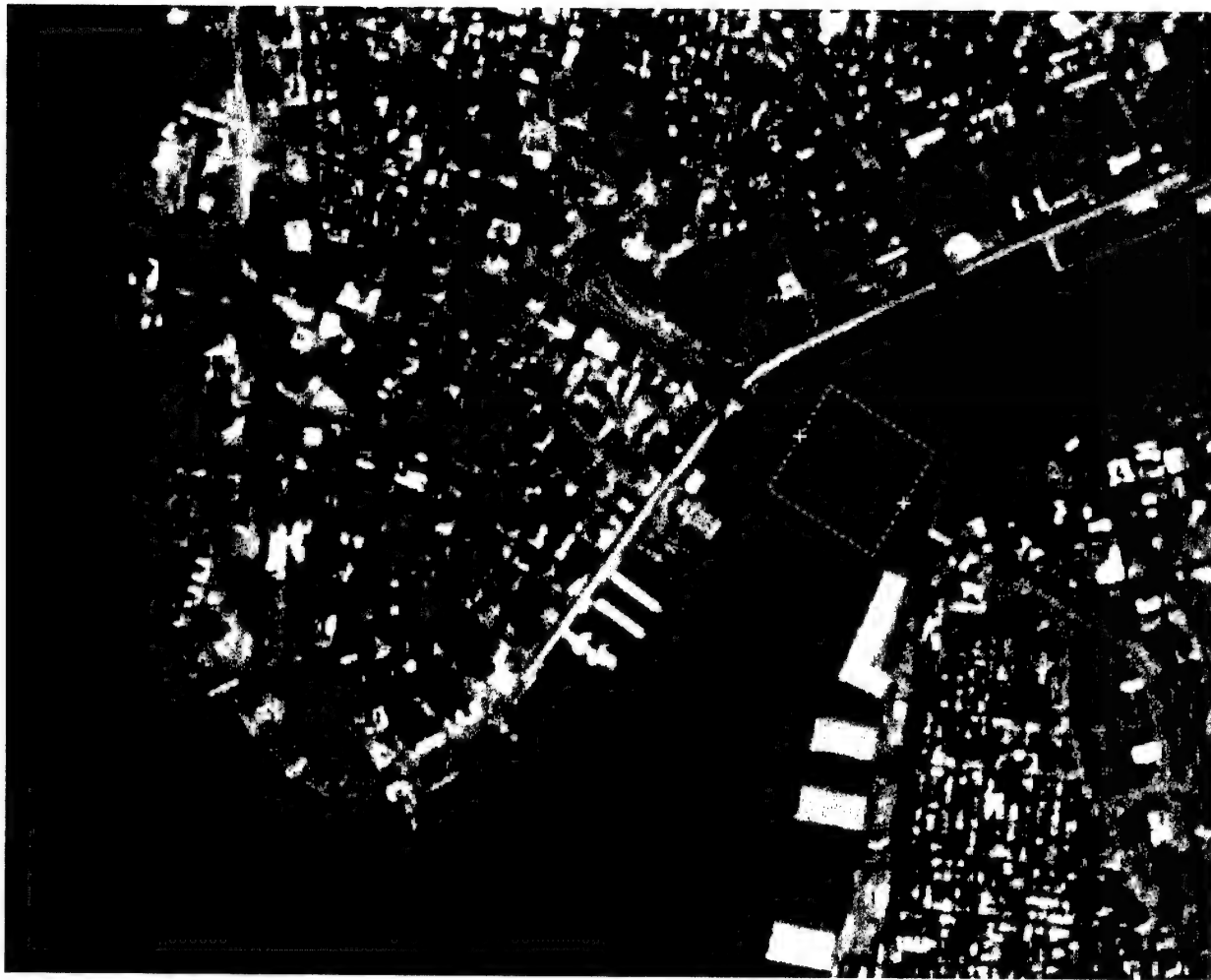
*Figure 19. Panchromatic Profile of the Earle Naval Pier, from the ROI outlined in Figure 18.*

SCA 3 on the March 20 DCE scanned across Manhattan and parts of Brooklyn. Figure 20 shows the image of Lower Manhattan, and the ROI selecting the Brooklyn Bridge for profiling. The Pan profile is plotted in Figure 21. The bridge axis in this case was 57.60° from the track.

*Figure 20. Panchromatic image of Lower Manhattan from 2001 March 20. The ROI delineates the data used to profile the Brooklyn Bridge.*
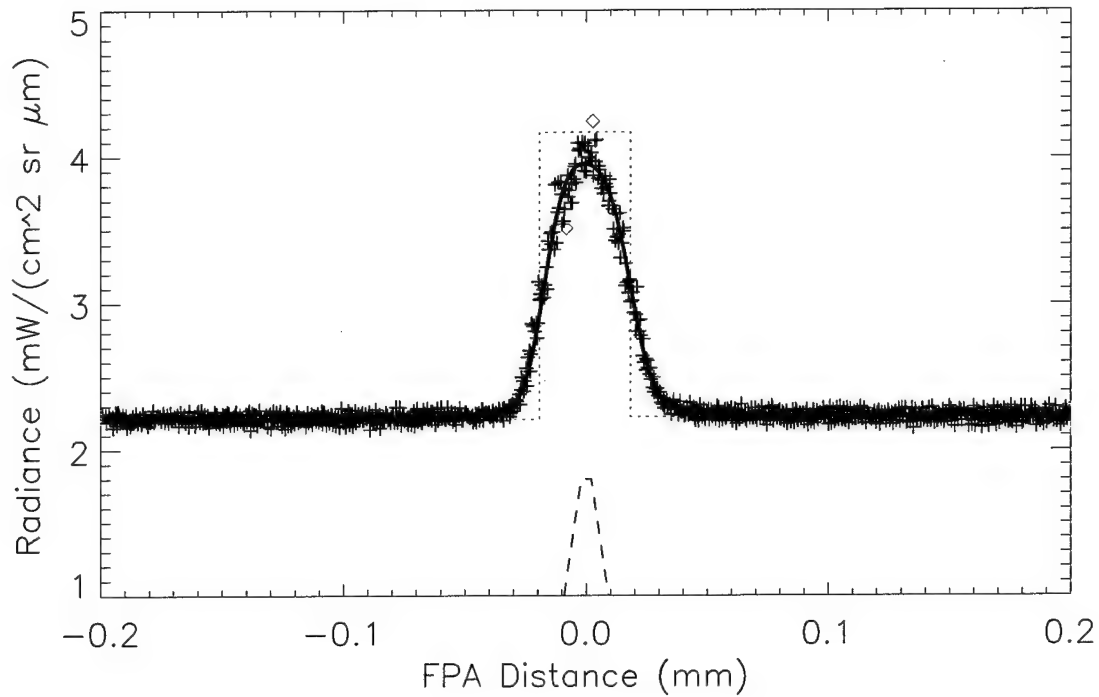
*Figure 21. Panchromatic Profile of the Brooklyn Bridge, from 2001 March 20.*

Also scanned by SCA 3 on 2001 April 14 was the Verrazano Narrows Bridge, seen in Figure 22. An attempt was made to fit this highly-structured image with a step-function profile, shown in Figure 23. A $\chi^2$ value of 1.54, for 2,213 DOF was obtained. This particular image is probably too complicated to be useful for the validation of the spatial transfer functions.
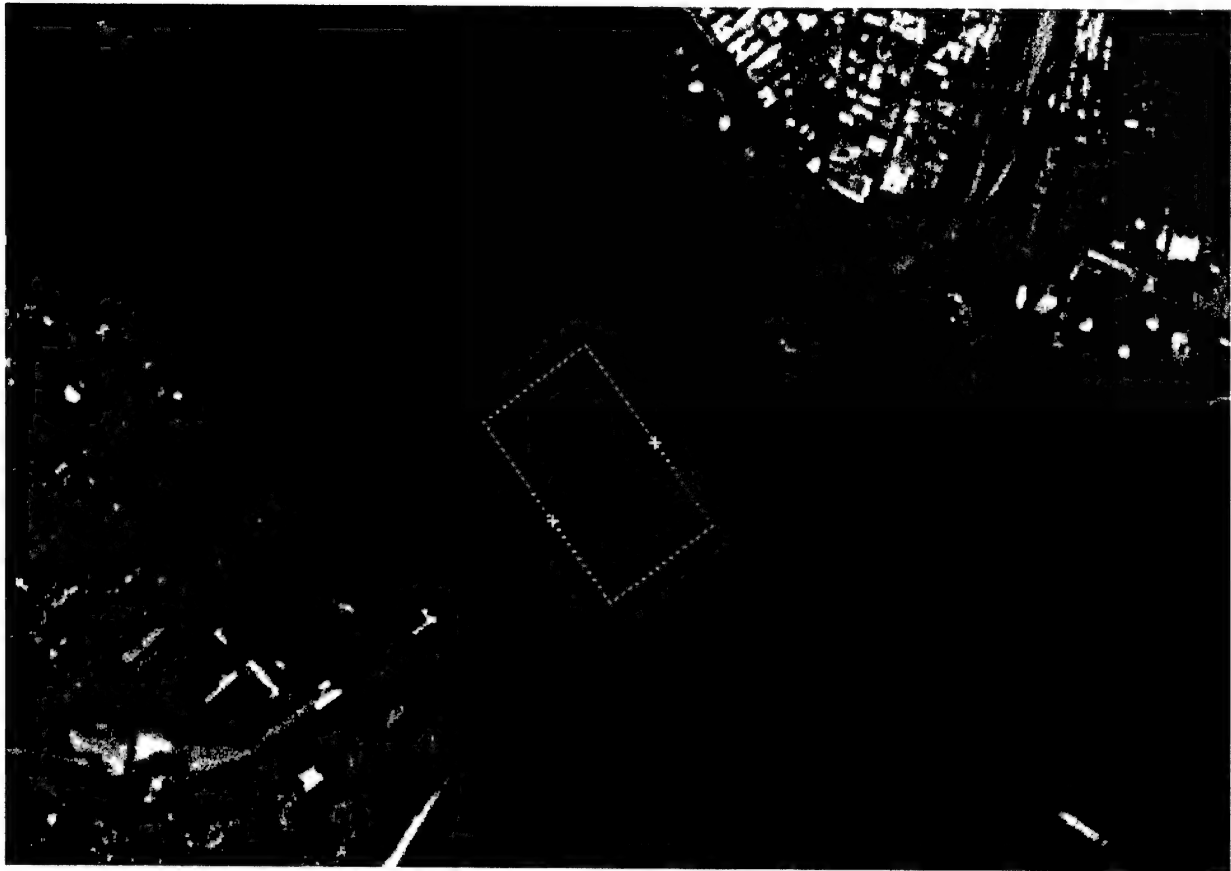
*Figure 22. Panchromatic image of the Verrazano Narrows from 2001 April 14.*

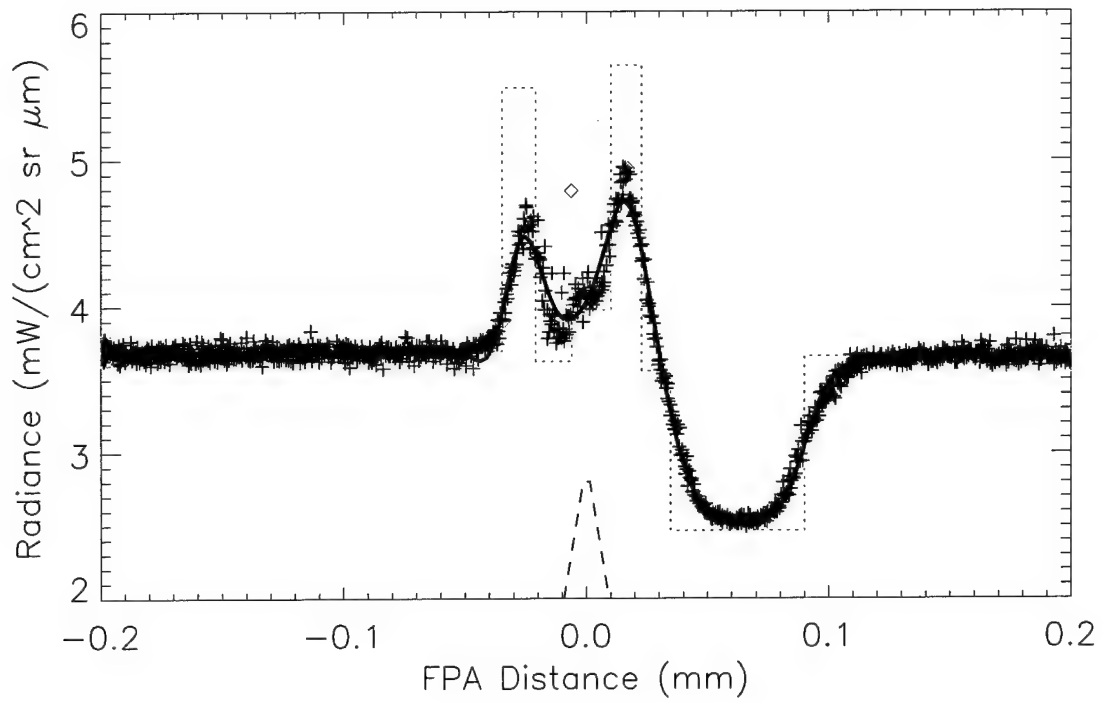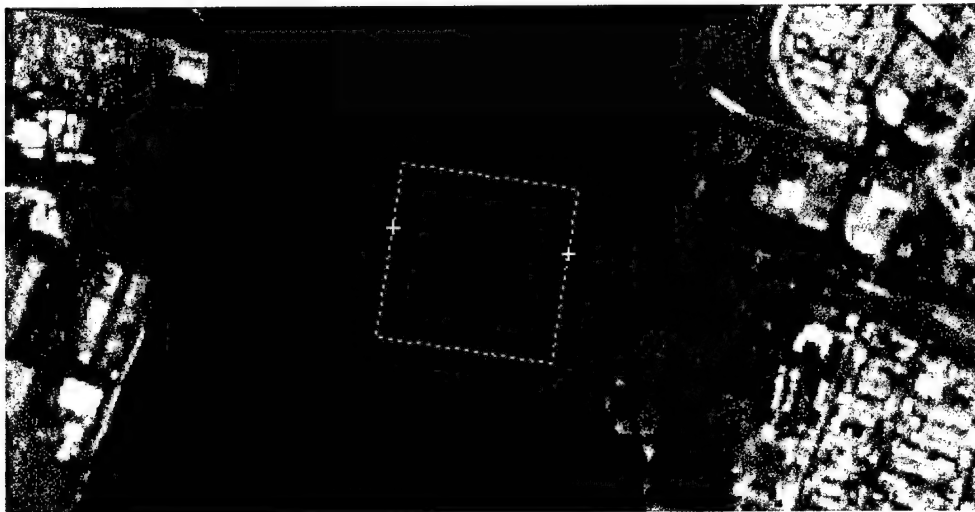*Figure 23. Panchromatic profile of the Verrazano Narrow Bridges from the ROI of Figure 22.*



*Figure 24. Panchromatic image of the New Jersey Turnpike Extension bridge.*

An image of the New Jersey Turnpike Extension bridge across Newark Bay was obtained from SCA 4 on 2001 April 14, shown in Figure 24. This bridge is at 81.22° from the track. Unfortunately, our least-squares fitting process did not converge to a sensible result, possibly because of the shadow north of the bridge.

On 2001 January 25, EO-1 scanned over Chocktawhatchee Bay, near Eglin Air Force Base in the Florida Panhandle. The Chocktawhatchee Mid-Bay Bridge was imaged in SCA 3, at 1.54° from the track, as seen in Figure 25. The panchromatic image and ROI for analysis are in Figure 26. A fitted Pan profile is shown in Figure 27 and the Band 4 profile is in Figure 28.
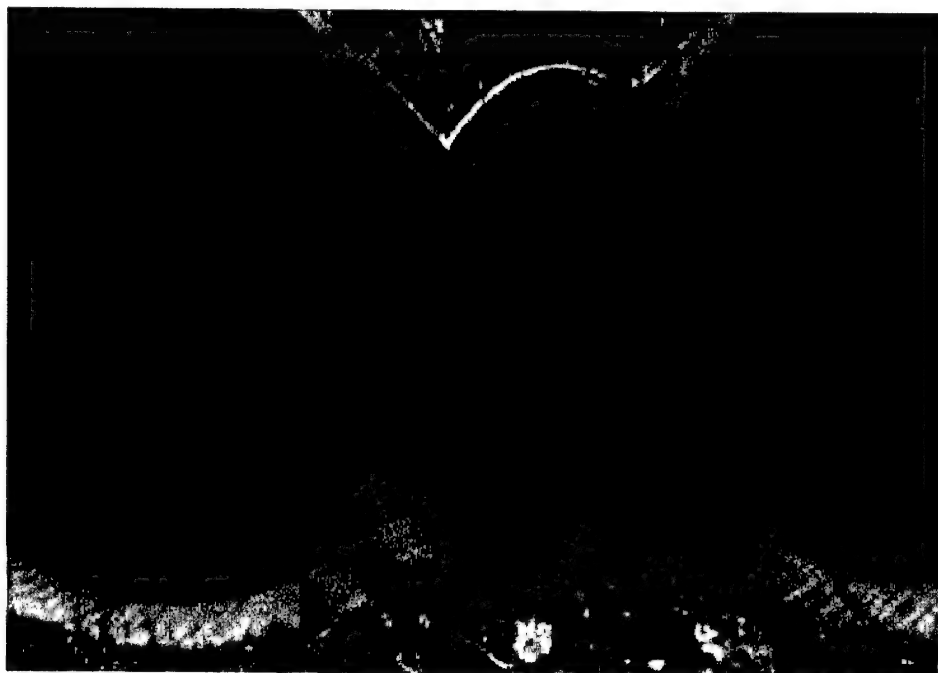


*Figure 25. Natural-color image of the Chocktawhatchee Mid-Bay Bridge, scanned on 2001 January 25.*

*Figure 26. Panchromatic image of the Mid-Bay Bridge and ROI for analysis.*
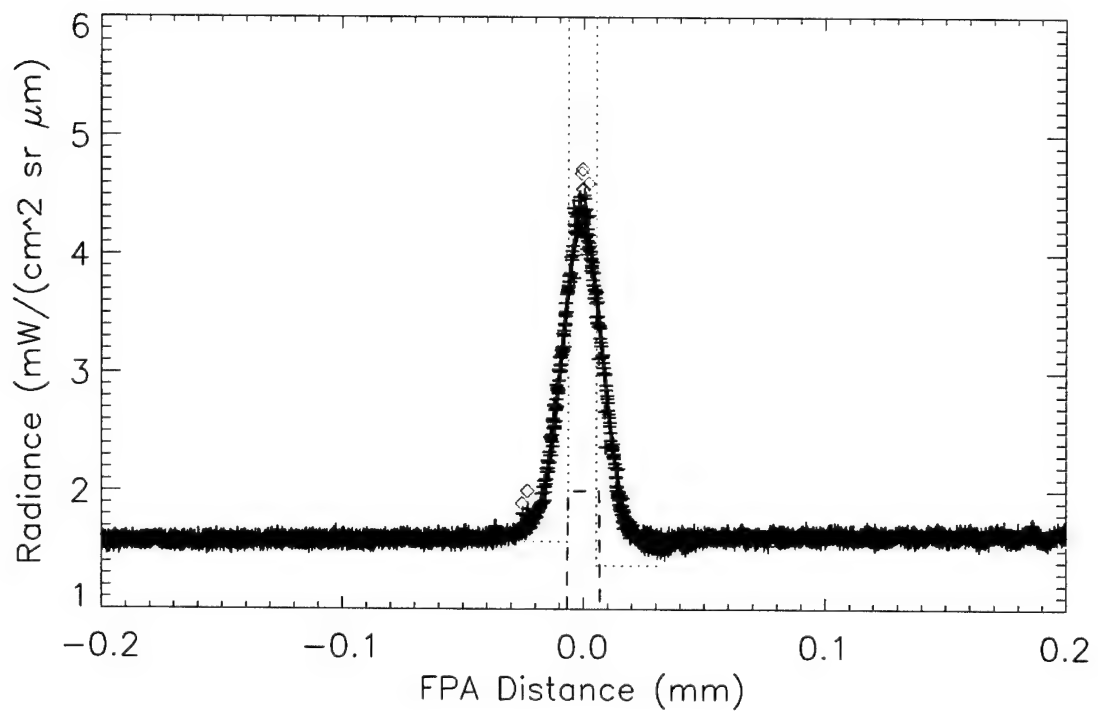
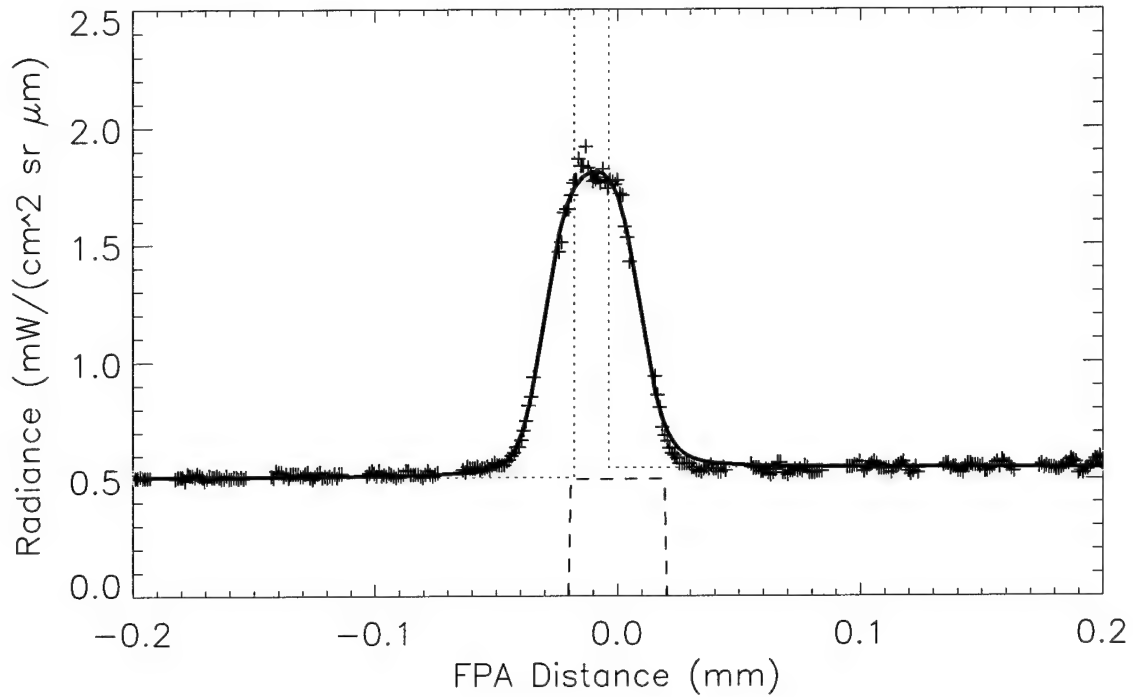*Figure 27. Panchromatic Profile of the Chocktawhatchee Mid-Bay Bridge.*

*Figure 28. Profile of the Chocktawhatchee Mid-Bay Bridge in Band 4.*

On 2001 September 20, the ALI collected an image of Lake Pontchartrain, shown in Figure 29. The 38.5 km-long, straight bridge at the left is the Lake Pontchartrain Causeway, a frequent subject for satellite imaging tests [9]. A view of the Causeway from a lower altitude, showing the bascule bridge for ships 12.9 km from the North shore, is seen in Figure 30. The bridge spans are each 10.0 m wide, and they are separated by 24.4 m. The axis of the Causeway was 4.14° from the EO-1 track. We selected a portion of the Causeway free of clouds, where the water was darkest, to be profiled (Figure 31). The Causeway image appeared in SCA 4. The Pan band profile is plotted in Figure 32. Figure 33 shows the fitted profile for Band 1. The twin spans are barely resolved in this band, but we were unable to obtain good parameter fits for the other multispectral bands. The fit to the Pan data looks excellent ($\chi^2$ = 1.50, for 3,000 DOF). The widths of the image stripes at the focal plane, fitted to the Pan data, are 9.53 μm for the West span, 8.16 μm for the East span, and 37.27 μm for the gap between spans. The center-to-center spacing of the spans is 46.11 μm. From the known center-to-center spacing (34.4 m), we can infer an image scaling factor of 1:746,042.

*Figure 29. Natural-color image of Lake Pontchartrain, acquired by the ALI on 2001 September 20.*
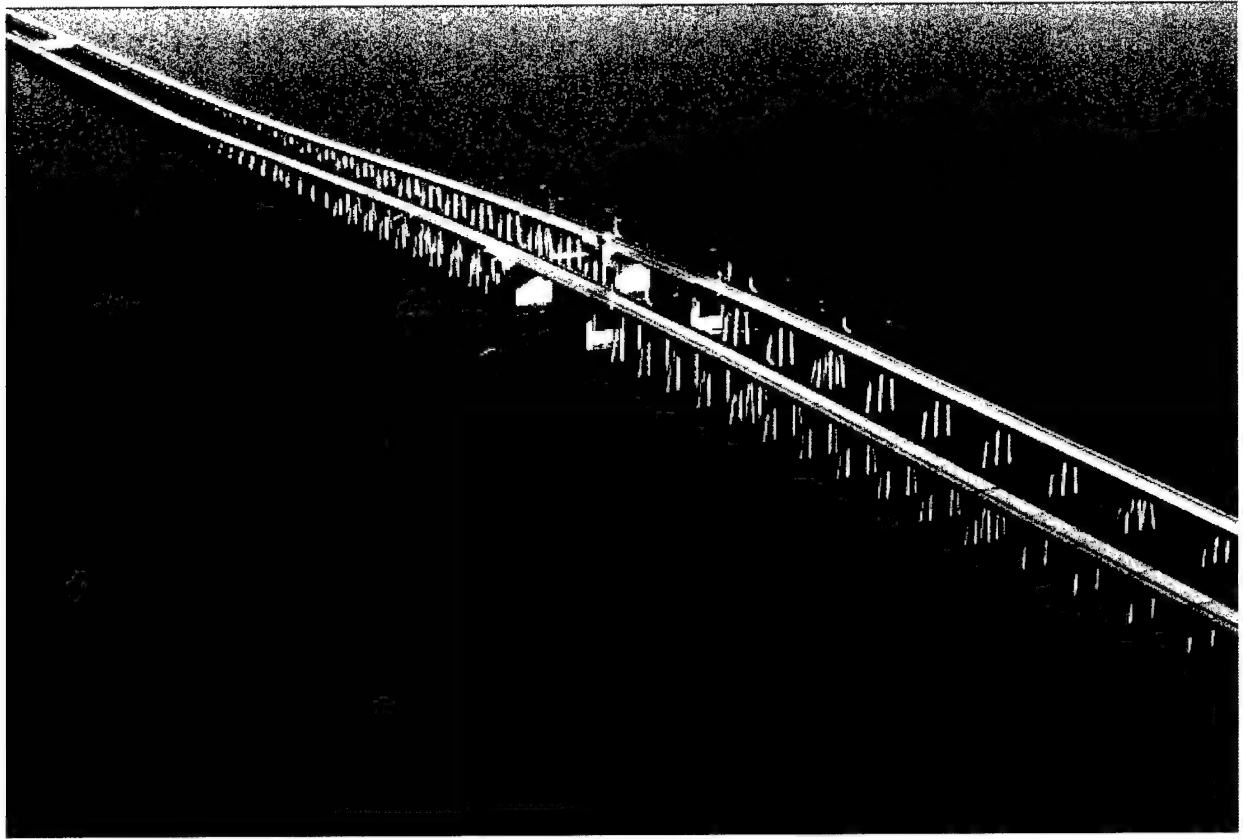
*Figure 30. Lake Pontchartrain Causeway, with passageway for boats.*
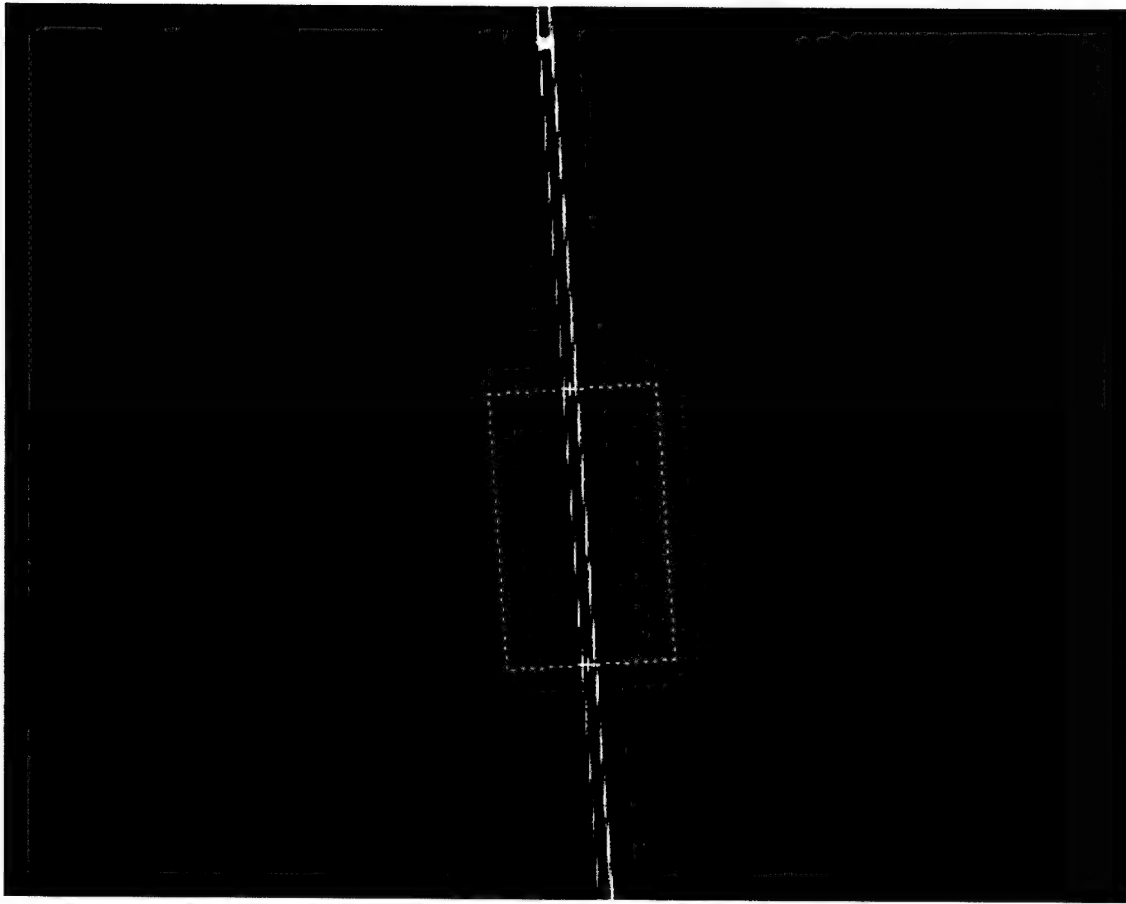
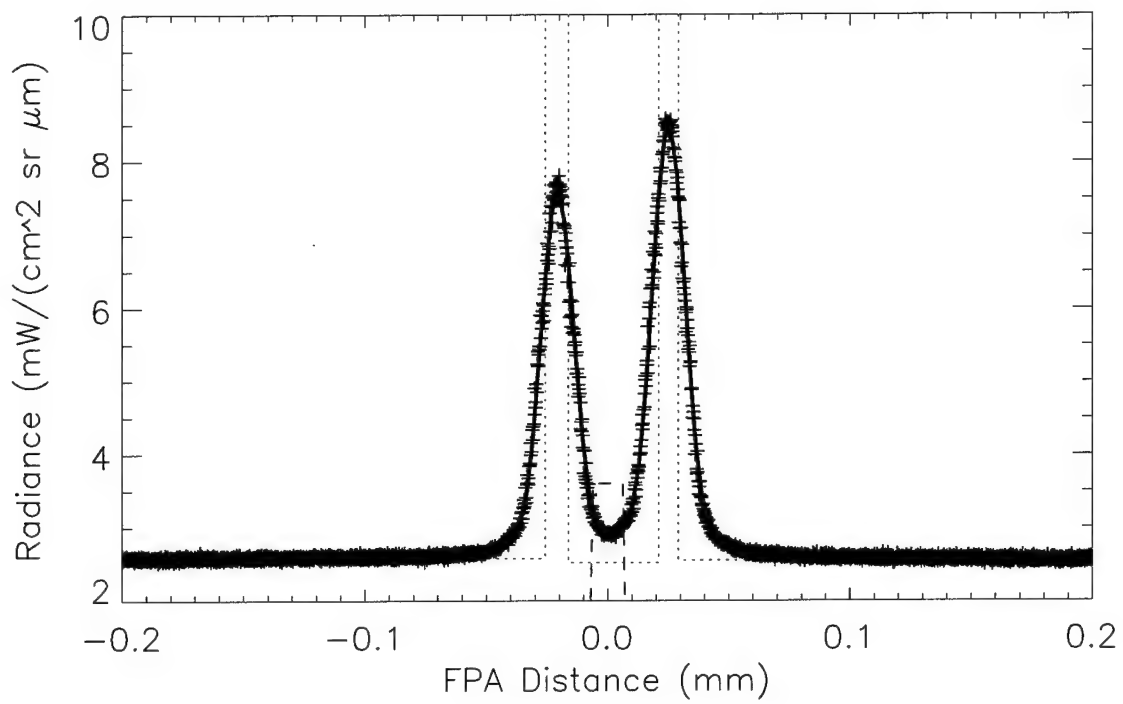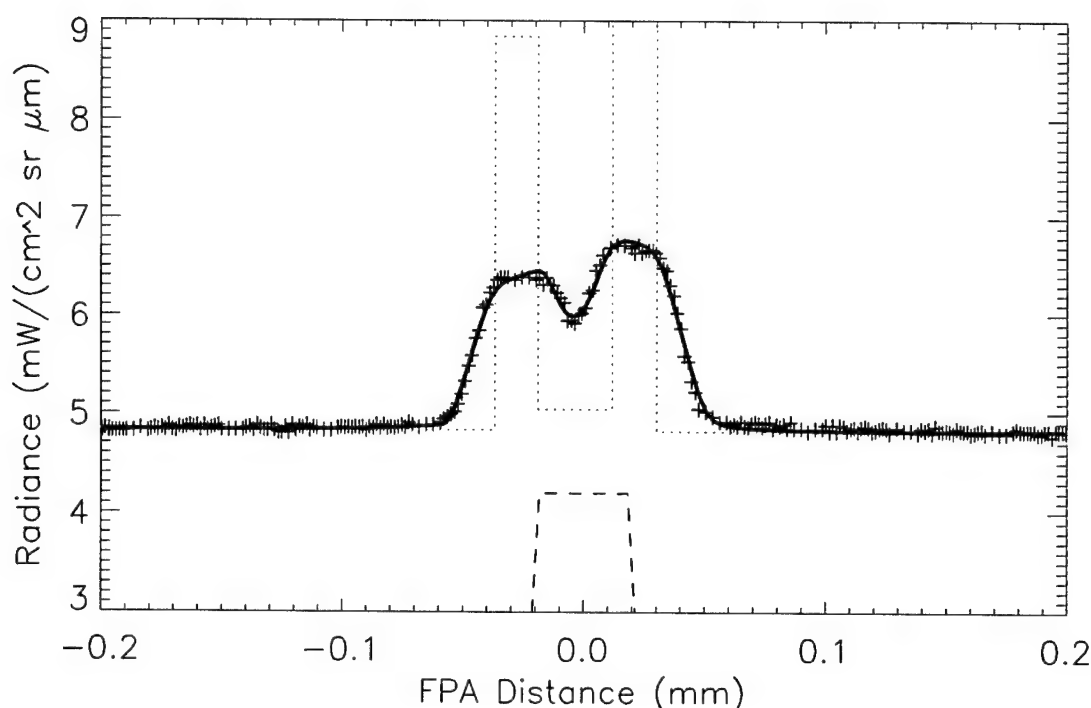*Figure 31. Selected portion of the Pan image of the Lake Pontchartrain Causeway.*

*Figure 32. Panchromatic band profile of the Lake Pontchartrain Causeway.*

*Figure 33. Band 1 profile of the Lake Pontchartrain Causeway.*


Many other bridge images captured by the ALI have been examined and fitted, including the Throgs Neck Bridge, New York; the Øresund Bridge between Malmö, Sweden and Copenhagen, Denmark; and the Harvard Bridge over the Charles River Basin in Boston. The results were all consistent with those presented here. Wherever the object being imaged could be adequately modeled by simple stripes of radiance, without too much unresolvable structure, the ALI spatial response computed from the pre-flight calibration parameters agreed extremely well with the observed image data. Given this agreement, we conclude that it is unnecessary to attempt to de-convolve on-orbit images in order to estimate the spatial transfer functions. That would be unlikely to yield any improvement over the pre-flight STF's.

The foregoing conclusion does not apply to the period from late December, 2000 to January 5, 2001. When those scenes were processed, the multispectral browse images were found to be less sharp than expected, indicating the presence of the contamination. Since that time, regular outgassing periods were adopted, in which the focal plane is warmed up for 4.5 hours to boil off the contaminants. This is repeated, initially every 5 days, then eventually every 20 days. The analyses presented here are of data obtained between 0.38 and 5.66 days after the preceding outgassing period.

# 5. LUNAR SCANS

Lunar Calibration scans have been routinely performed with the ALI every month since February, 2001. Normally, they take place near the time of full moon. The main purpose for these lunar calibrations is to check the radiometric calibration of the instrument against a source that should be extremely repeatable over millennia, and which is available for comparison with other instruments. For radiometric calibration, the radiance integrated over the full disk is to be compared with detailed ground-based measurements made over many lunar cycles [7], [10].

Lunar scans are also useful for the purpose of testing the sharpness of the instrument's spatial response. The bright limb of the moon is contrasted with the black space background, yielding an edge-spread function. In this section, we compare the limb profiles obtained during lunar scans with the edge-spread functions we expect on the basis of the pre-flight calibrations.

During each lunar calibration, the spacecraft is maneuvered to scan the moon slowly across each SCA in turn. The scan pattern is shown in Figure 34. The image of the moon traverses each SCA at approximately one-eighth of the nominal earth-scene image speed. Quick-look images are produced by re-binning the radiometrically-calibrated data by 8:1 in the scan direction, and applying any necessary frame shifts to allow for the odd-even detector offsets. More accurate reconstructions of the lunar image make use of the attitude, position and velocity telemetry from the spacecraft, and the computed position of the moon, as described in the following sub-section.
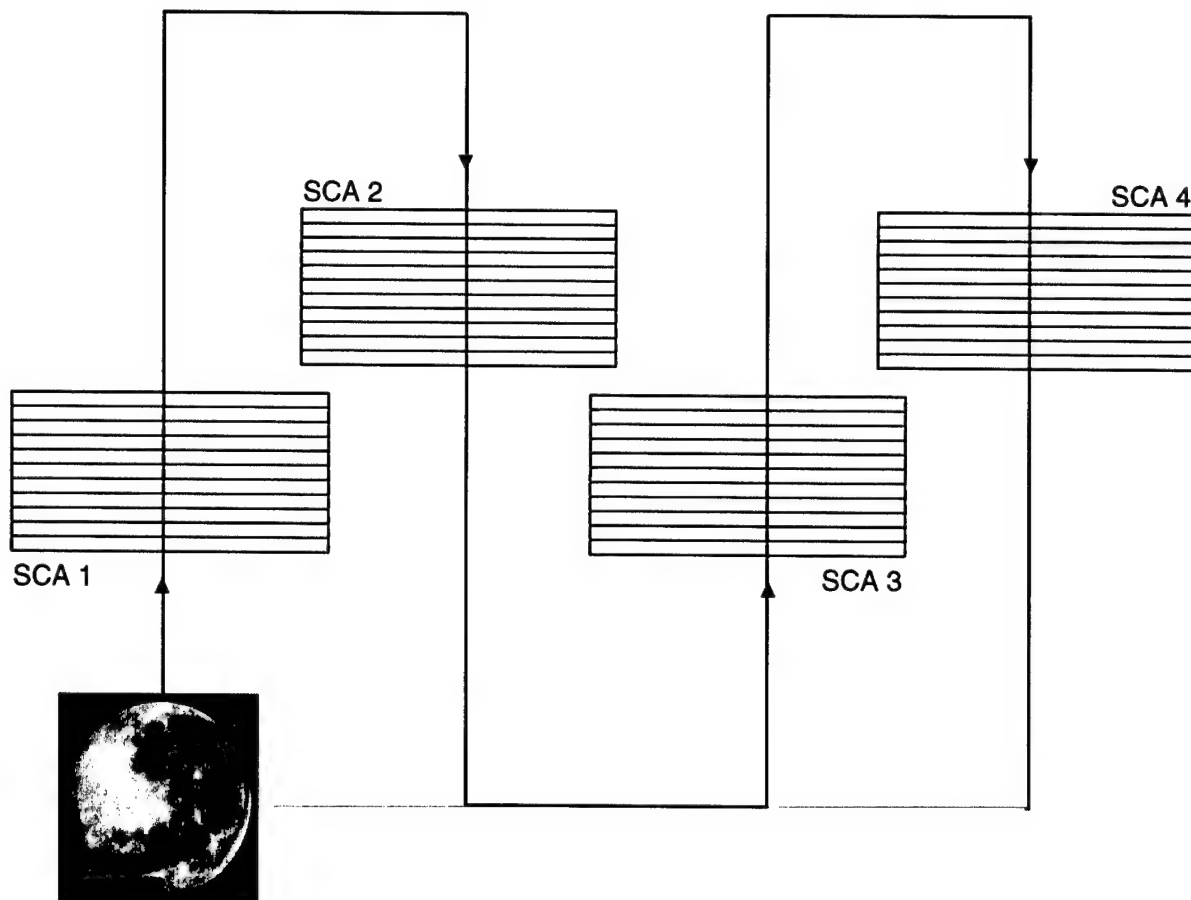
*Figure 34. Pattern of lunar calibration scans.*

## 5.1 ANALYSIS PROCEDURE

The first step in analysis of a lunar calibration scan is to perform the radiometric calibration to a set of level 1R files. Next, the IDL procedure Skymap_all.pro reads the HDF telemetry file *yyyy_ddd*_ali.hdf to determine the instrument settings, such as the start time of the image data, the integration times and frame rates. The telemetry file *yyyy_ddd*_acs.hdf is read to establish the position, velocity, and attitude of the spacecraft, recorded once per second during the scan. The position of the moon throughout the scan, in equatorial coordinates, is computed with MOONPOS.PRO, an IDL procedure from the Astronomy User's Library at GSFC (idlastro.gsfc.nasa.gov/homepage.html). The positions of all of the detectors on the ALI focal plane are read from the detector line-of-sight (LOS) calibration file.

48

Procedure Skymap_all.pro computes a cosines matrix for each Kalman filter quaternion reading, and applies the LOS data to establish when each SCA was scanning across the moon. Next, it reads the level 1R image data files, and projects the detector readings to a re-sampled image array centered on the moon, at a pre-selected size and resolution. All nine multispectral bands and the panchromatic band are mapped in this way, and written to HDF output files, one per SCA. The changing positions of the spacecraft and the moon are accounted for, and the data are projected to a plane through the center of the moon. The velocity of the spacecraft relative to the Earth-Moon system is also taken into account, though the magnitude of this effect is $\leq 25$ $\mu$rad. Typical images produced in this process are shown in Figure 35 and Figure 36. (Some slight distortion of the image caused by the varying range to the center of the moon may be expected, but it is not important in the present applications.)
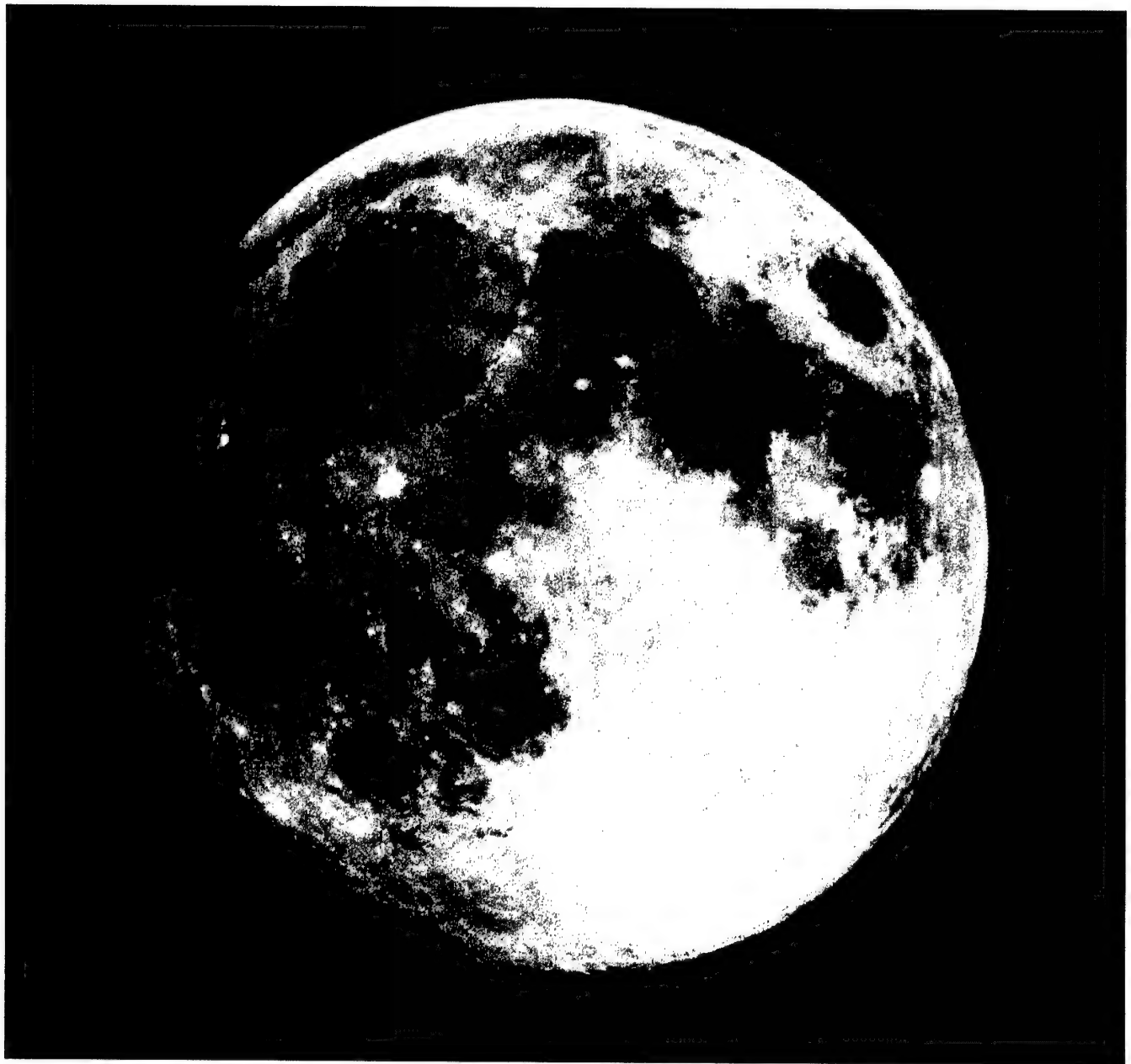
*Figure 35. Typical panchromatic image of the moon, from a lunar calibration of 2001 February 7.*

*Figure 36. Panchromatic image of the moon, from the lunar calibration of 2002 February 26, SCA 2. This image has been contrast-enhanced, and lightly sharpened in PhotoShop.*

51

The Multispectral images of the moon look remarkably alike across all bands. Ordinary experience shows this for the visible bands. To compare the visible bands with the SWIR bands, some pseudo-color images were formed. The image shown in Figure 37, from 2002 February 26, SCA 2, uses red, green, and blue to represent bands 7, 5', and 2. The Moon still looks basically gray, but there are local areas of light blue and reddish brown. Thus there are small but noticeable variations in reflectivity over the wavelength range 0.5 to 2.2 μm.

*Figure 37. Multispectral image of the moon, from the lunar calibration of 2002 February 26, SCA 2. Red, green and blue represent bands 7, 5', and 2, respectively. Each band image has been lightly sharpened and contrast-enhanced in PhotoShop.*

To facilitate analysis of the ALI spatial response at the lunar limb, Skymap_all.pro calls Limb_band.pro to create data structures containing all information relating to an annulus of specified radii, centered on the moon. The data structures contain the detector numbers, scaled radiances, right ascension (RA) and declination (Dec) of the detector relative to the moon, and radial and azimuthal position angles, all on a frame-by-frame basis. Also, SUNPOS.PRO is called, and the solar phase angle and orientation are computed. For each SCA, Skymap_all.pro writes the data structure and solar parameters, etc. to an unformatted binary file. Figure 38 shows the geometry of the limb annulus, and several azimuth bins examined from the scan of 2002 Feb 26.
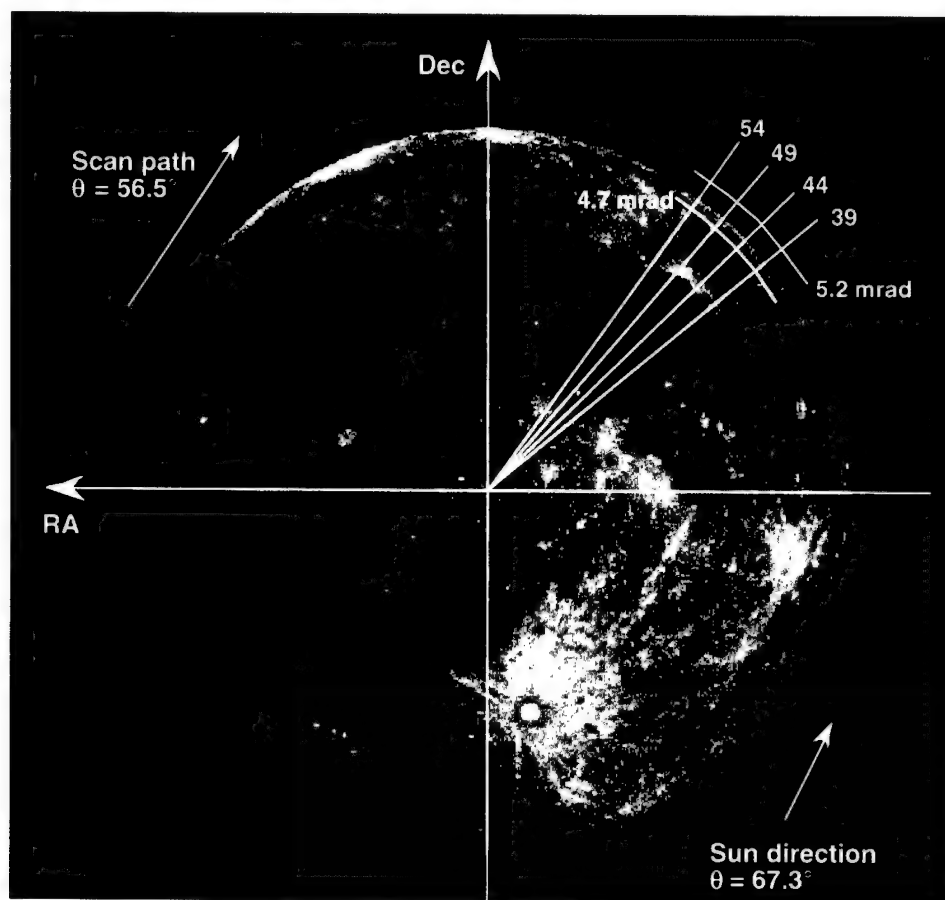


*Figure 38. Geometry of lunar scan 2002 Feb 26.*

## 5.2 LUNAR LIMB PROFILES

Procedure `Limb_plot_Bands.pro` was developed to read the binary file of limb data from `Skymap_all.pro`, and plot the radiances as a function of radius from the moon's center. The solar phase and azimuth are used to compute the expected outline of the illuminated portion of the disk, by the `crescent_2.pro` procedure. Approximate positions of the limb crossings for each detector are found, where the radiance is just one sixth of the peak radiance in the image. The radii of these crossings are plotted *vs.* azimuth. Small RA and Dec offsets of the apparent position of the moon are estimated, and expected radius *vs.* azimuth curve for the limb is over-plotted. The offsets result from any errors in the pointing parameters of the telescope that were used in the `Skymap_all.pro` procedure. Comparison of the individual detector-crossing radii with the smooth crescent curve shows that the ALI is seeing terrain elevation differences on the order of tens of microradians at the limb.

For the portion of the limb that is in full solar illumination, we parcel out the data points into azimuth bins of typically 5°. PostScript files of radiance *vs.* radius plots are then written. A simple model of the radiance is derived from the data by fitting a quadratic curve to the radiance inside the limb (by at least a detector width), and truncating it to zero at the radius where the radiance data drop to 50% of the extended curve. This model is plotted over the radiance data as a green line. Next, procedure `Make_DSTF.pro` produces the dynamic system transfer function for the current band and SCA, based on the pre-flight MTF calibration [3]. Procedure `Slice_STF.pro` derives the one-dimensional transfer function corresponding to the local angle of the limb. Finally, the simple fitted model is Fourier-transformed, multiplied by this calibrated ALI spatial transfer function, then reverse-transformed to produce the expected ALI response curve, which is plotted as a red line. Examples of the finished plots may be seen in Figure 39 to Figure 41.
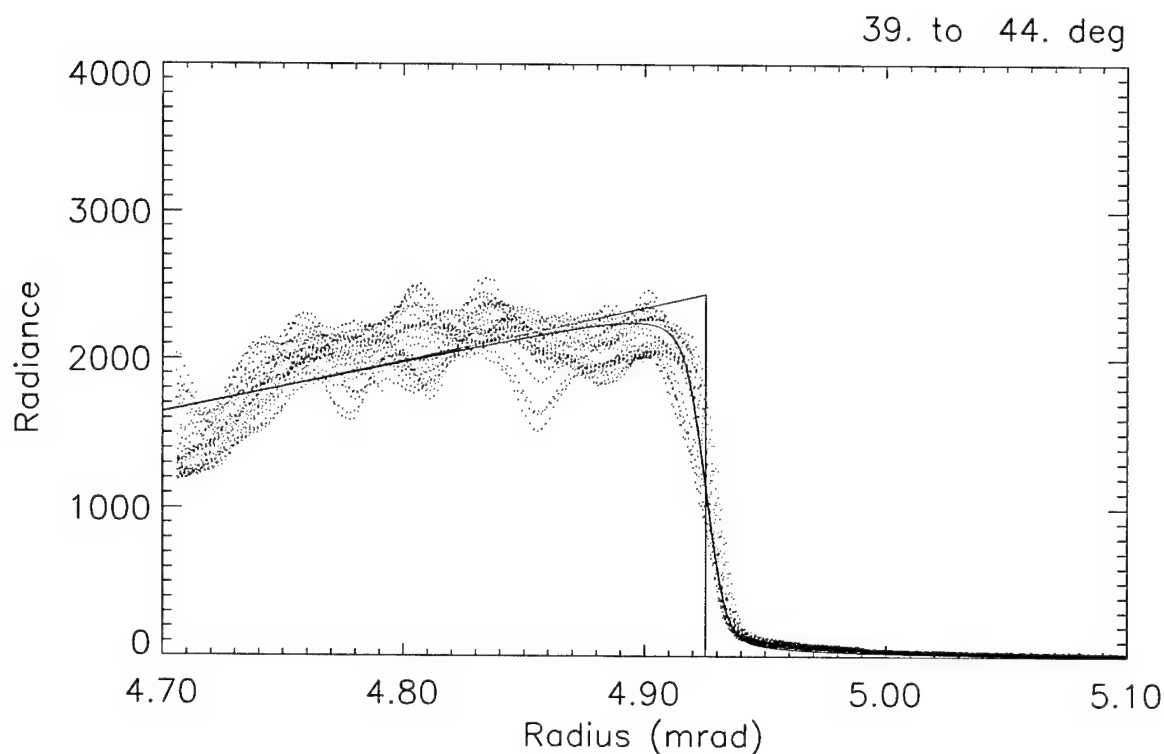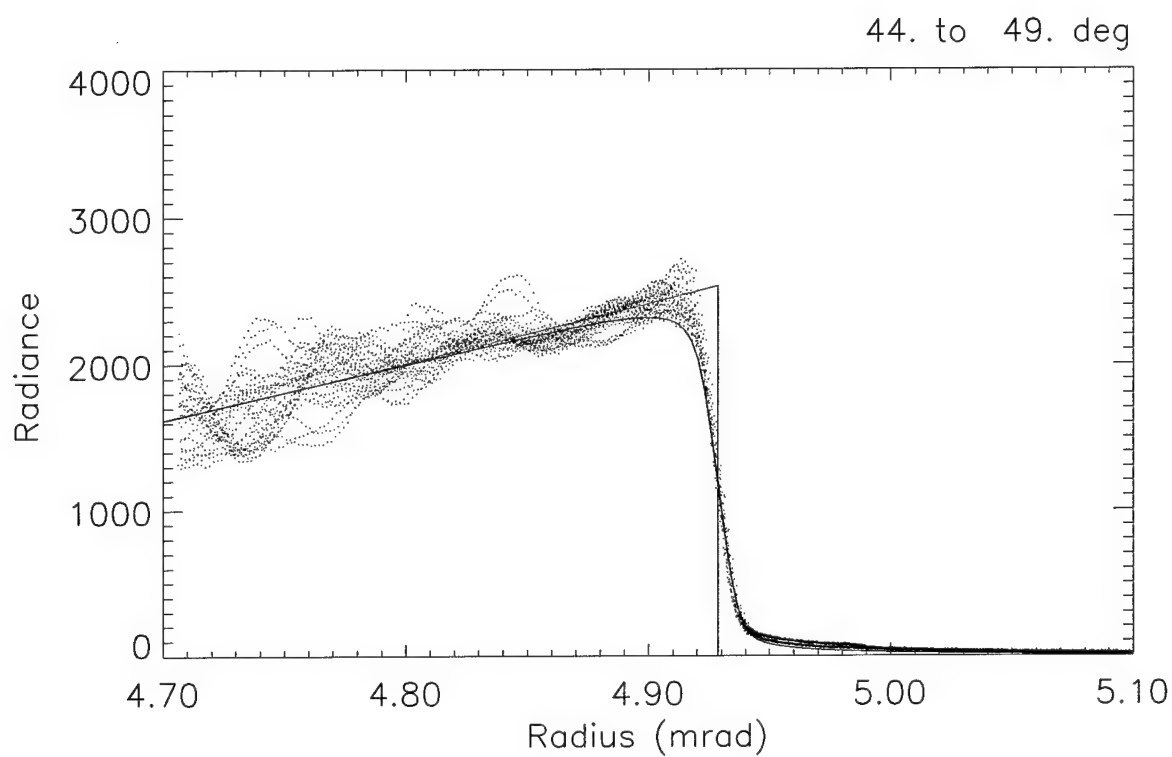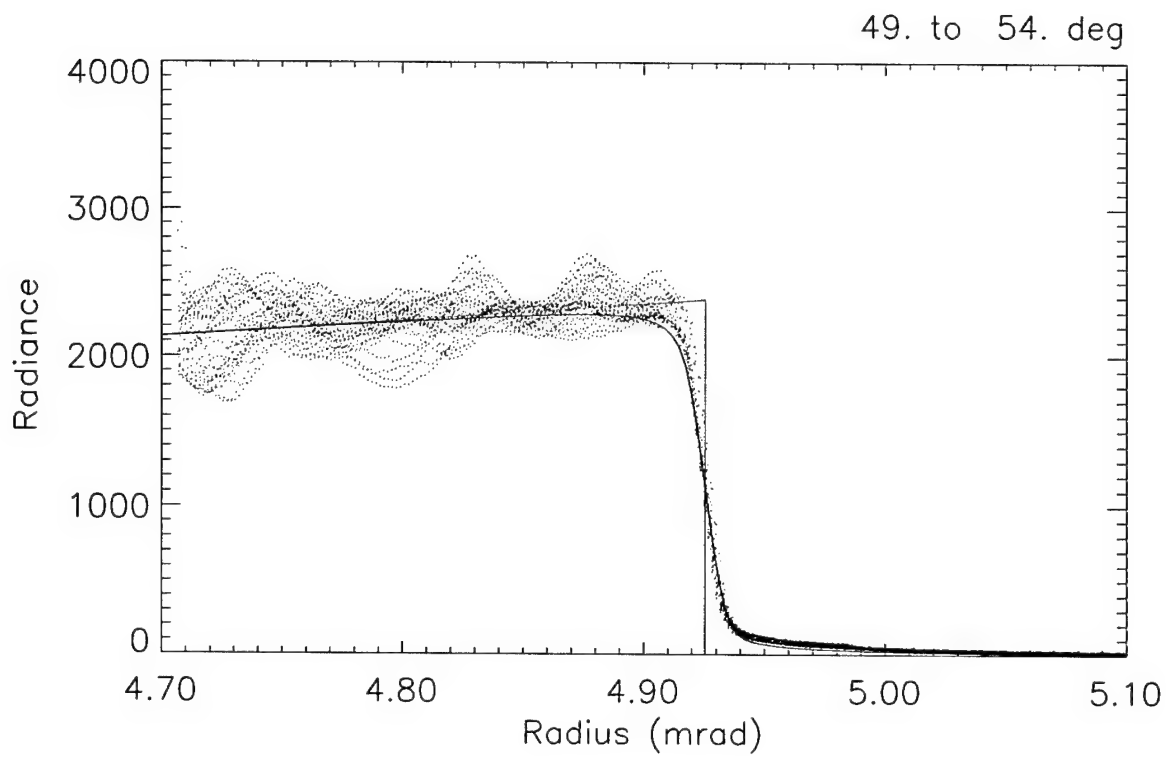
*Figure 39. Lunar limb profile, from scan of 2002 February 26, Pan band, SCA 2, over 39° to 44° azimuth (see Figure 38). The black dotted curves are radiance readings from the individual detectors. The green line represents simplified fitted model of radiance near the limb. The red line is the predicted ALI response to the model.*

### 5.2.1 Panchromatic Band Limb Profiles

Examination of the limb plots shows that there is a range of apparent radii for the limb, as a function of azimuth. The $\theta$ bin from 44° to 49° has been selected for detailed presentation here, as it appears to show minimal radial variation, as indicated by the tight clustering of the Pan radiance curves there (Figure 40). From the plot, it is apparent that the observed data agree well in general with the expected spatial response, based on pre-flight calibrations and modeling. The corresponding plots for SCA's 1, 3, and 4 are shown in Figure 42 to Figure 44. Variations in the estimated radius of the limb from one SCA to another are the result of inaccuracies in the overall pointing reconstructions, which have not been fine-tuned at this time.
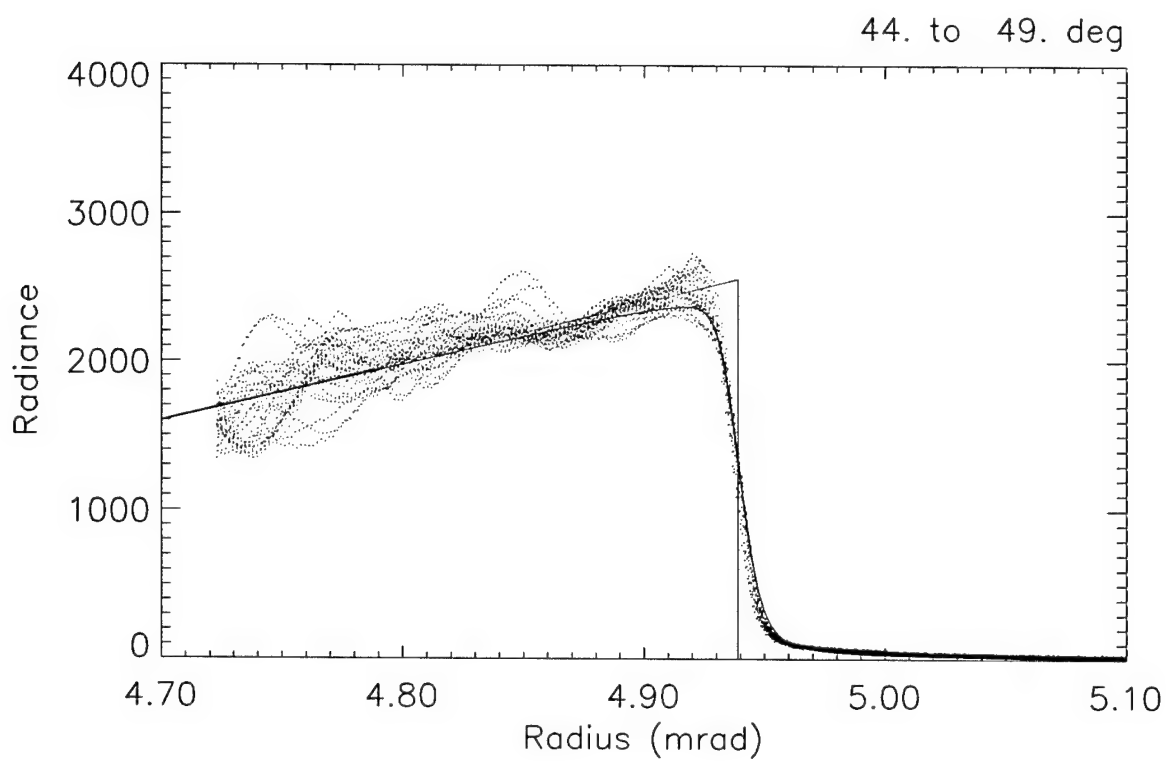
56

*Figure 40. Lunar limb profile, from scan of 2002 February 26, Pan band, SCA 2, over 44° to 49° azimuth.*
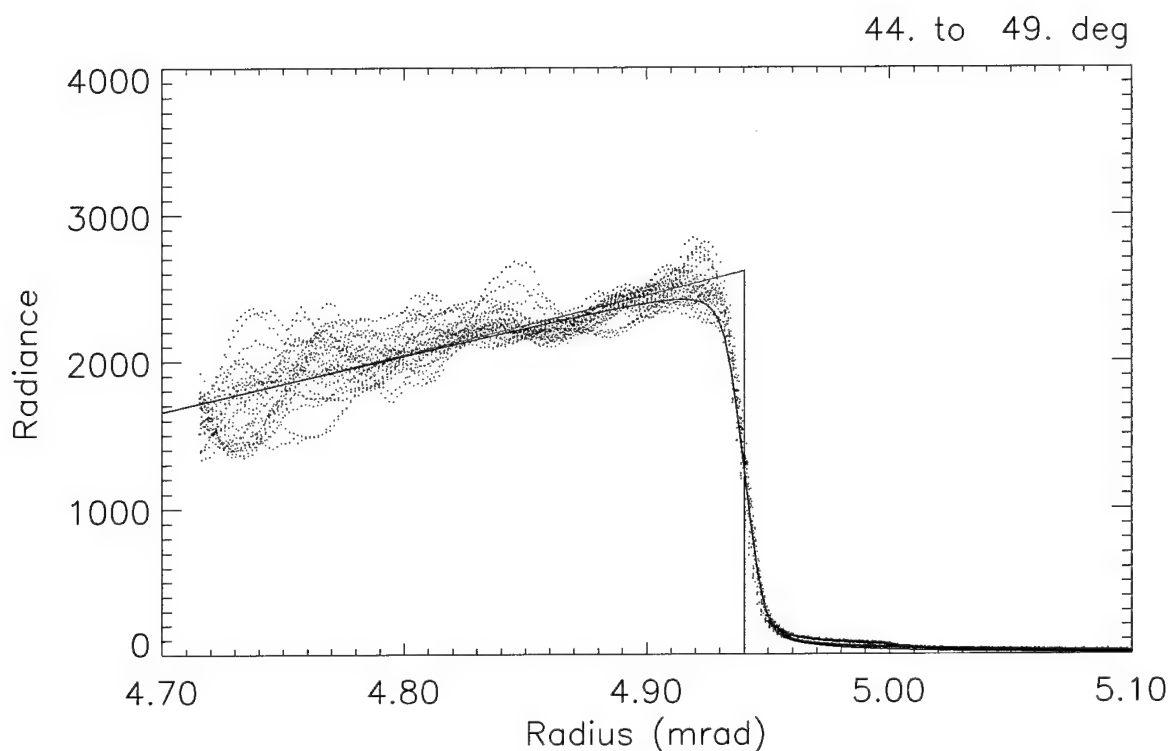
*Figure 41. Lunar limb profile, from scan of 2002 February 26, Pan band, SCA 2, over 49° to 54° azimuth.*
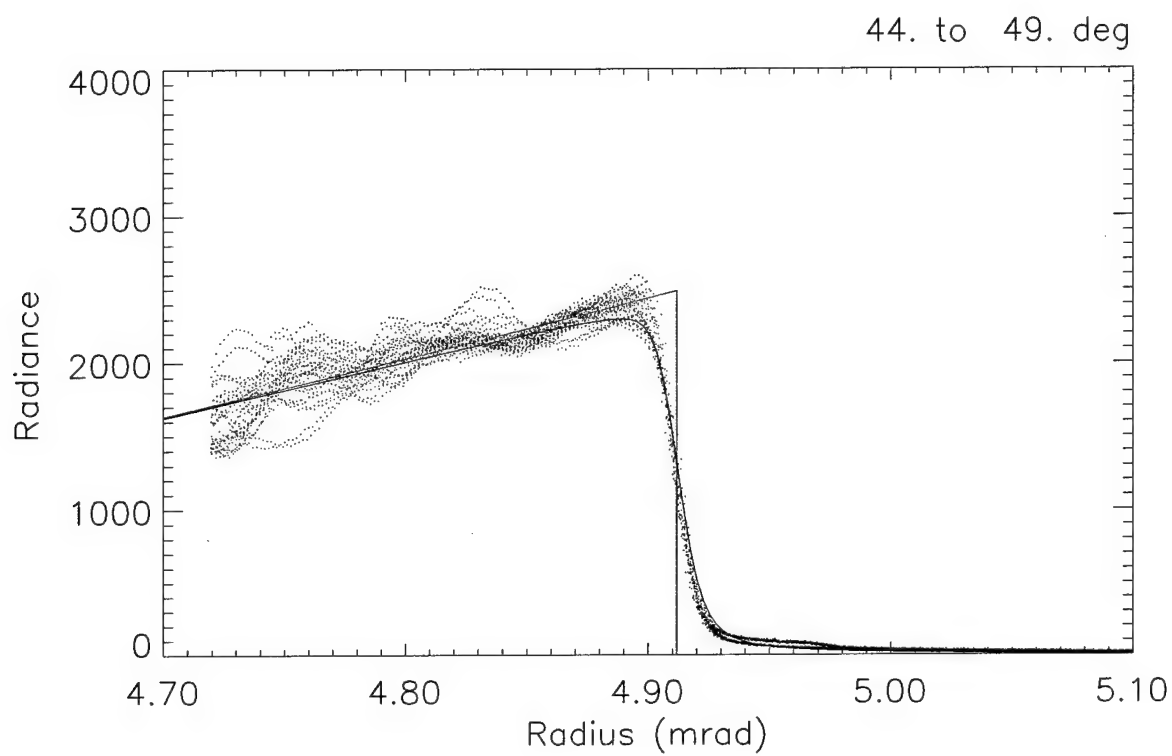
*Figure 42. Lunar limb profile, from scan of 2002 February 26, Pan band, SCA 1, over 44° to 49° azimuth.*

*Figure 43. Lunar limb profile, from scan of 2002 February 26, Pan band, SCA 3, over 44° to 49° azimuth*

*Figure 44. Lunar limb profile, from scan of 2002 February 26, Pan band, SCA 4, over 44° to 49° azimuth*

The deep-space background in the lunar limb scans provides a unique opportunity to examine the spatial responses of the sensor at angles several pixel widths away from an edge. Here, optical scattering and weak cross-talk effects may show up. Accordingly, we have made semi-logarithmic plots of radiance *vs.* radius, corresponding to those in the preceding figures. An example is shown in Figure 45, where the SCA 1 Pan detector normalized average radiances *vs.* radius are plotted. Again, the predicted ALI edge response is plotted as a solid red curve, and the data points fit it quite well, down to the 5% level. The odd and even-numbered detectors were plotted separately, after it was noticed that there appeared to be two separate radiance levels at approximately 60 μrad from the limb. At that radius, the even detectors show an excess signal amounting to approximately 1.5% of the peak lunar limb radiance. At still greater radii, the difference is reversed, with odd detectors showing an excess. All of the SCA's show similar behavior in the Pan band. Beyond ~30 μrad from the limb, all SCA's and bands show excess signal above the model prediction. The spatial transfer function model does not include a term to account for optical scattering, either by the mirror surfaces, or by contamination on the filters.

61

Curves were added to the semi-logarithmic plots in an attempt to clarify the unpredicted response variations. To show the difference between the even and odd detectors, the even minus odd radiances were plotted as a solid green curve and a red curve shows odd minus even. For the Pan band, a dotted red curve is added to represent a "ghost" response at approximately the 1% level, and shifted 63 µrad in the scan direction. This ghost response appears to fit the even detector excesses well, with levels of 1.5, 0.9, 0.5, and 1.1% of the peak, for SCA's 1 to 4, respectively. No attempt has yet been made to fit the much smaller excess signal in the odd detectors at larger distances from the limb. The semi-logarithmic plots of normalized average Pan band radiance *vs.* radius for SCA's 2, 3, and 4 are plotted in Figure 46 through Figure 48.
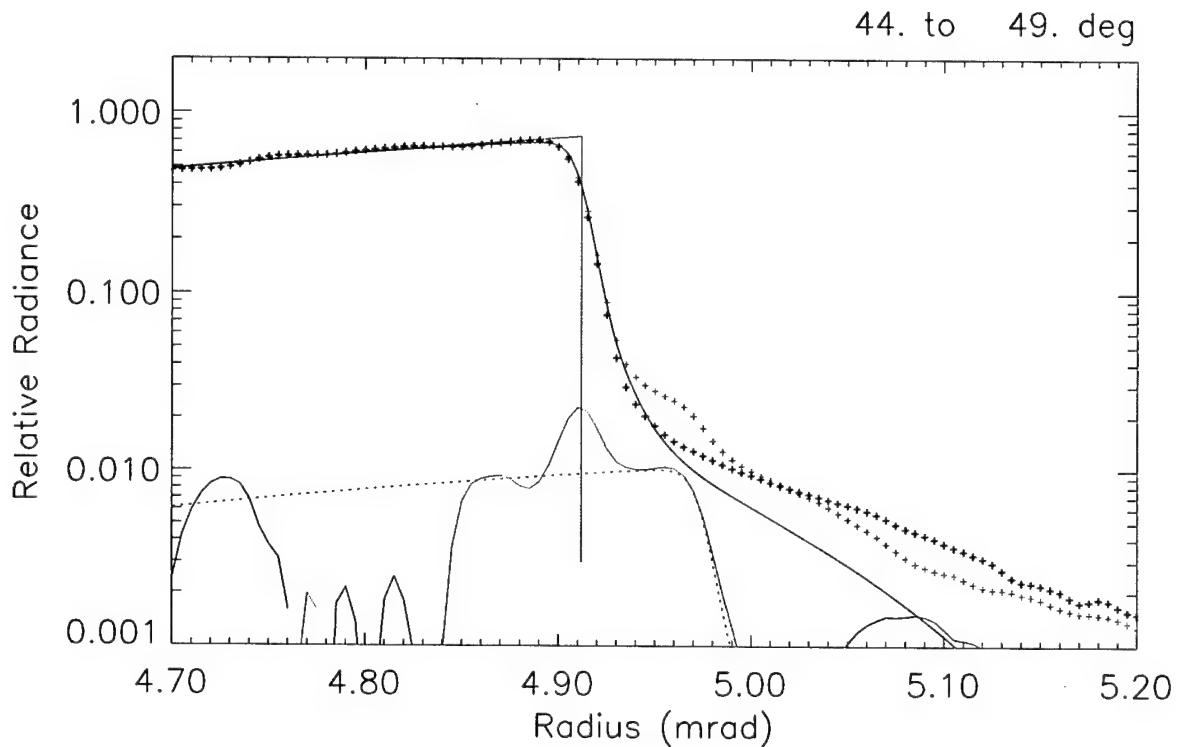


*Figure 45. Lunar limb profile in SCA 1, Pan band over 44° to 49° azimuth, as in Figure 42. The black crosses are the average normalized radiance for the odd-numbered detectors, and the green crosses are the even detector radiances. The various curves are explained in the text.*
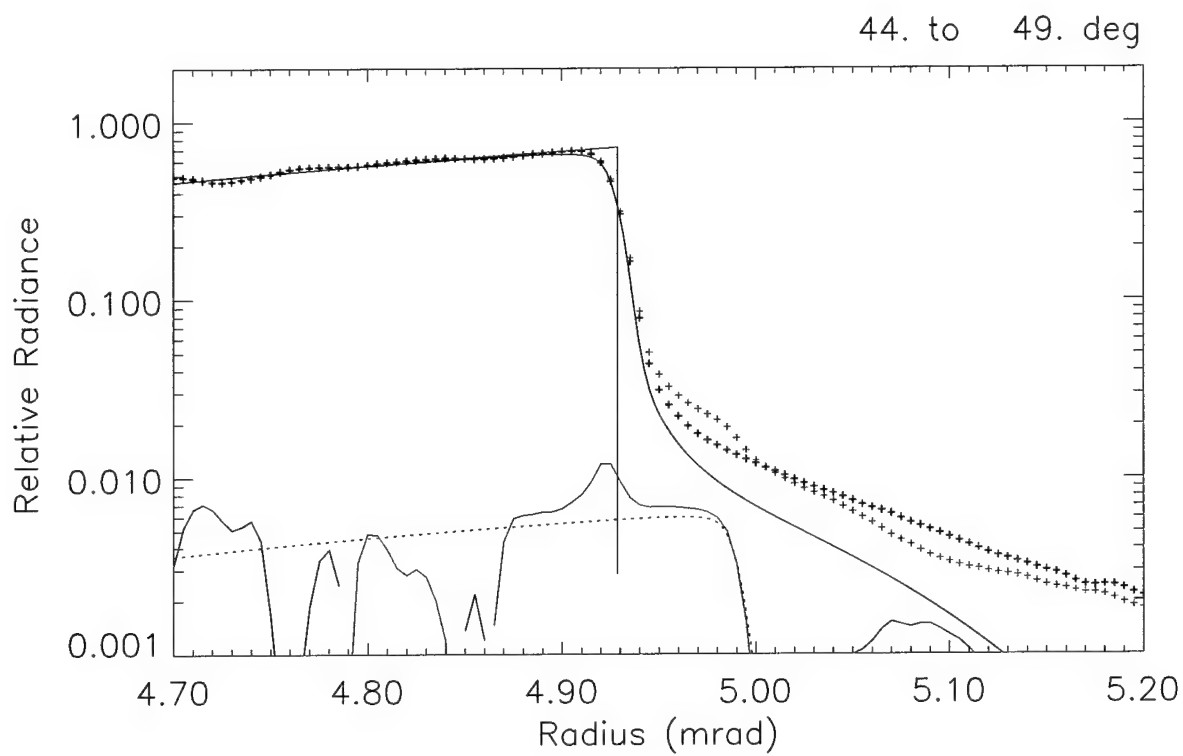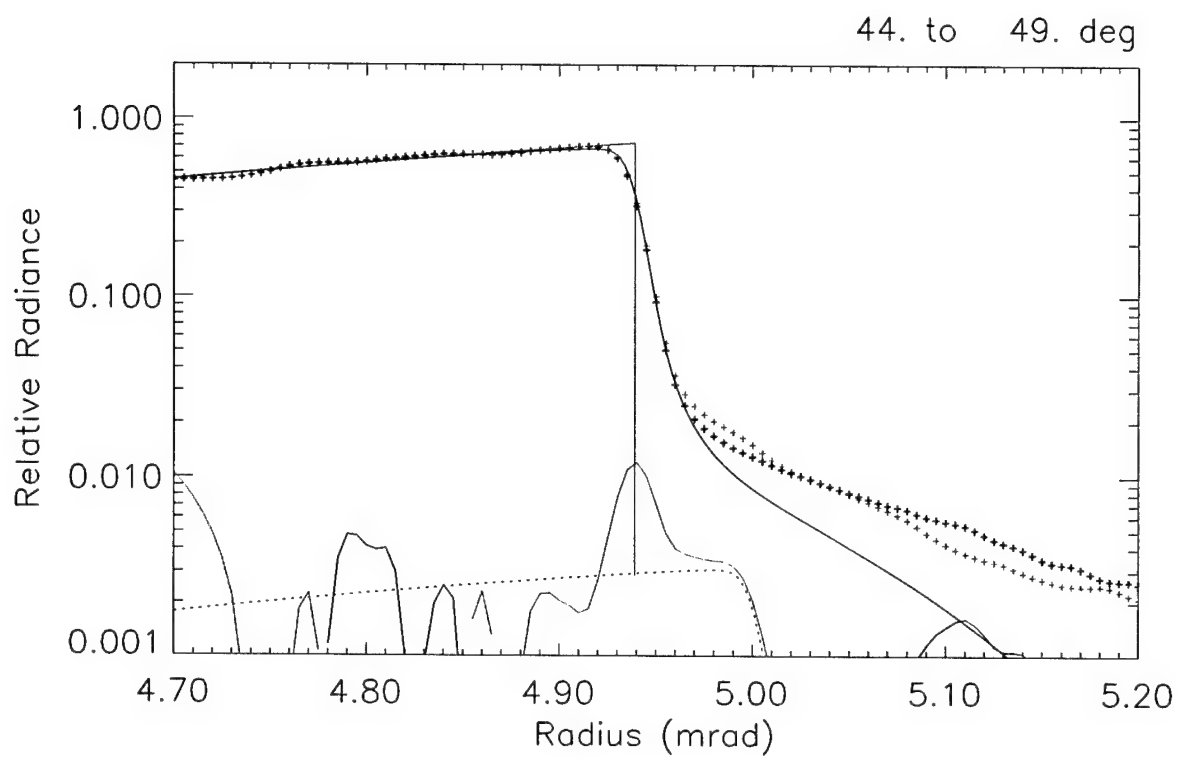
62

*Figure 46. Lunar limb profile in SCA 2, Pan band over 44° to 49° azimuth, as in Figure 40.*

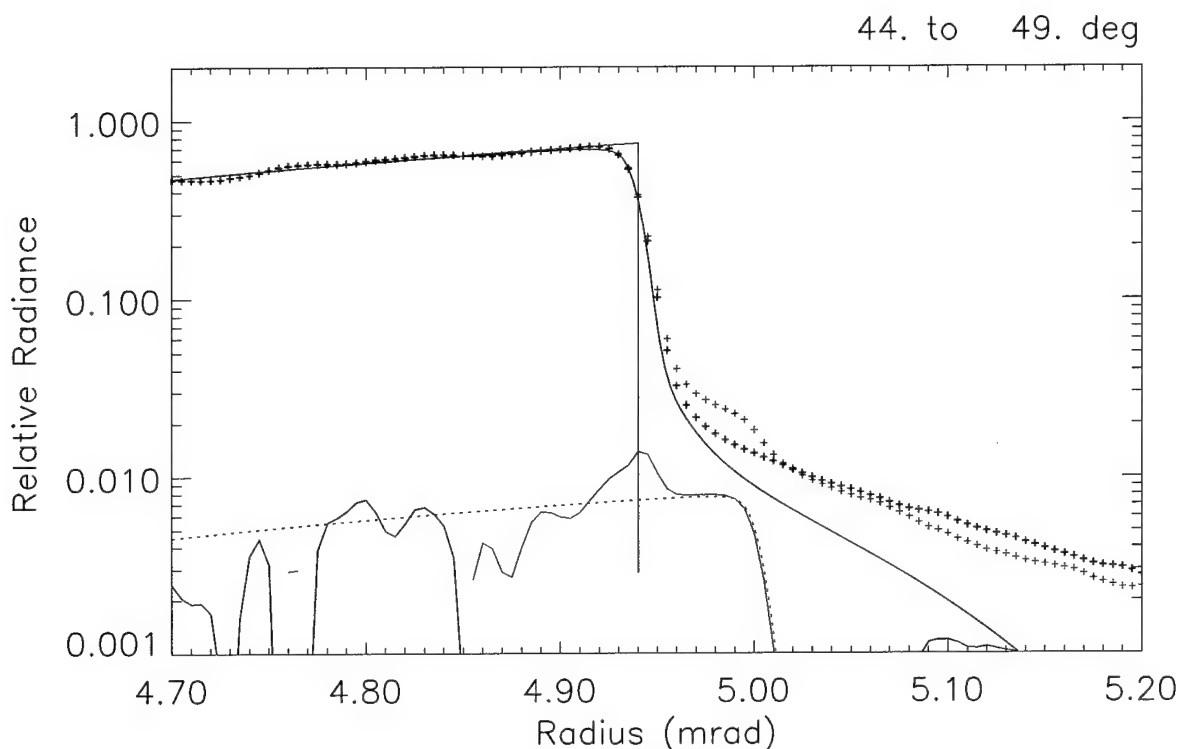Figure 47. Lunar limb profile in SCA 3, Pan band over 44° to 49° azimuth, as in Figure 43.

*Figure 48. Lunar limb profile in SCA 4, Pan band over 44° to 49° azimuth, as in Figure 44.*

### 5.2.2   Multispectral Limb Profiles

All of the multispectral bands have been analyzed in the same way as the Pan band, except that the "ghost" effect at 63 µrad from the limb does not appear in these bands. Data from SCA 3, band 3, and SCA 4, band 2 are not presented here, as they were corrupted by the detector cross-talk problem. [7]. Again, we show both linear and semi-logarithmic plots of radiance *vs.* radius. The same azimuth bin (44° to 49°) as shown in the preceding Pan analyses is used here. Figure 49 to Figure 57 show the multispectral radiances for SCA 1, and Figure 58 through Figure 66 are the corresponding plots for SCA 2. The results for SCA 3 are very similar to those for SCA 1, and those for SCA 4 are very similar to those for SCA 2. The odd SCA's differ from the even SCA's in being oriented oppositely to the scan direction (see Figure 34).
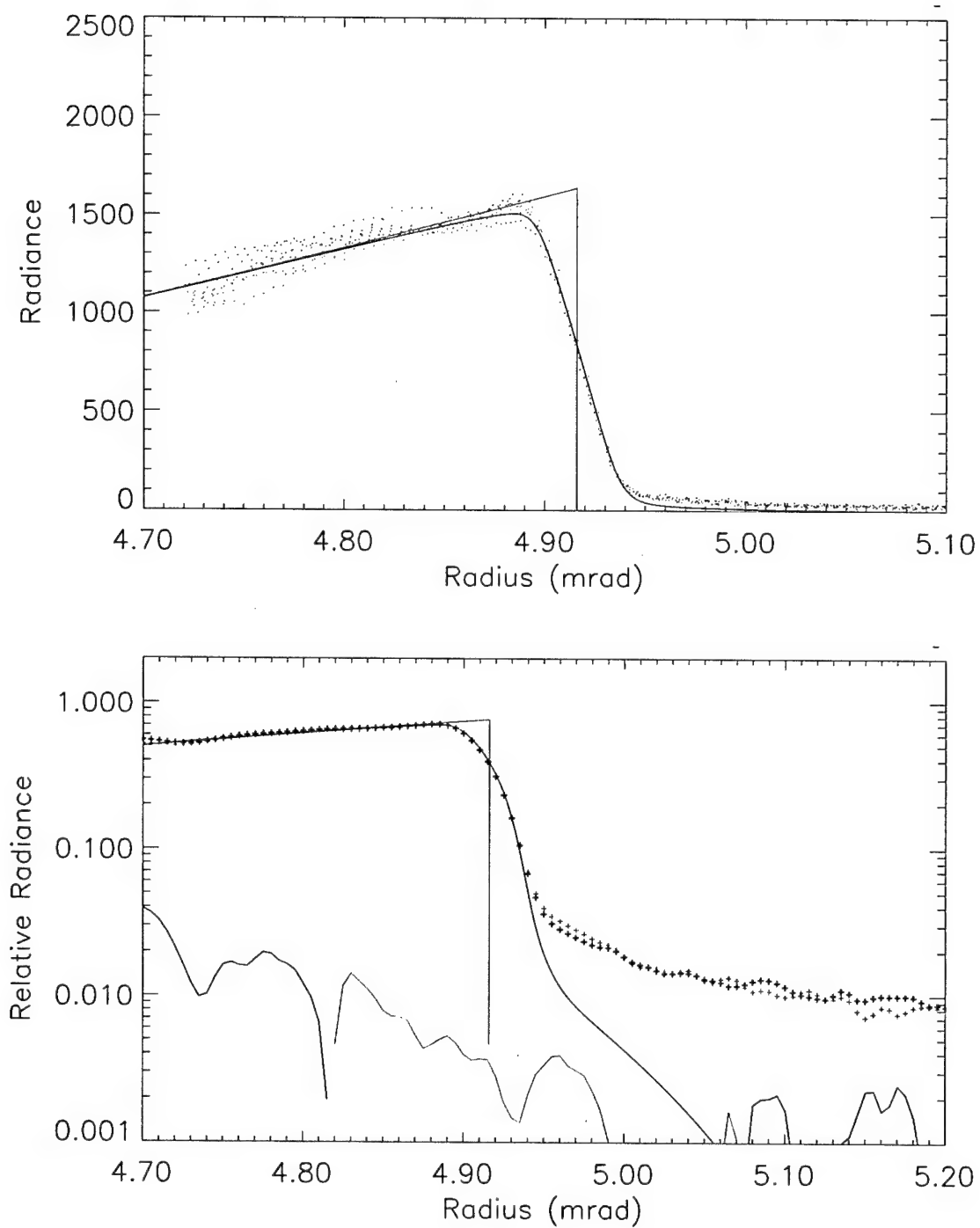
*Figure 49. Lunar limb profile in SCA 1, band 1', over 44° to 49° azimuth.*
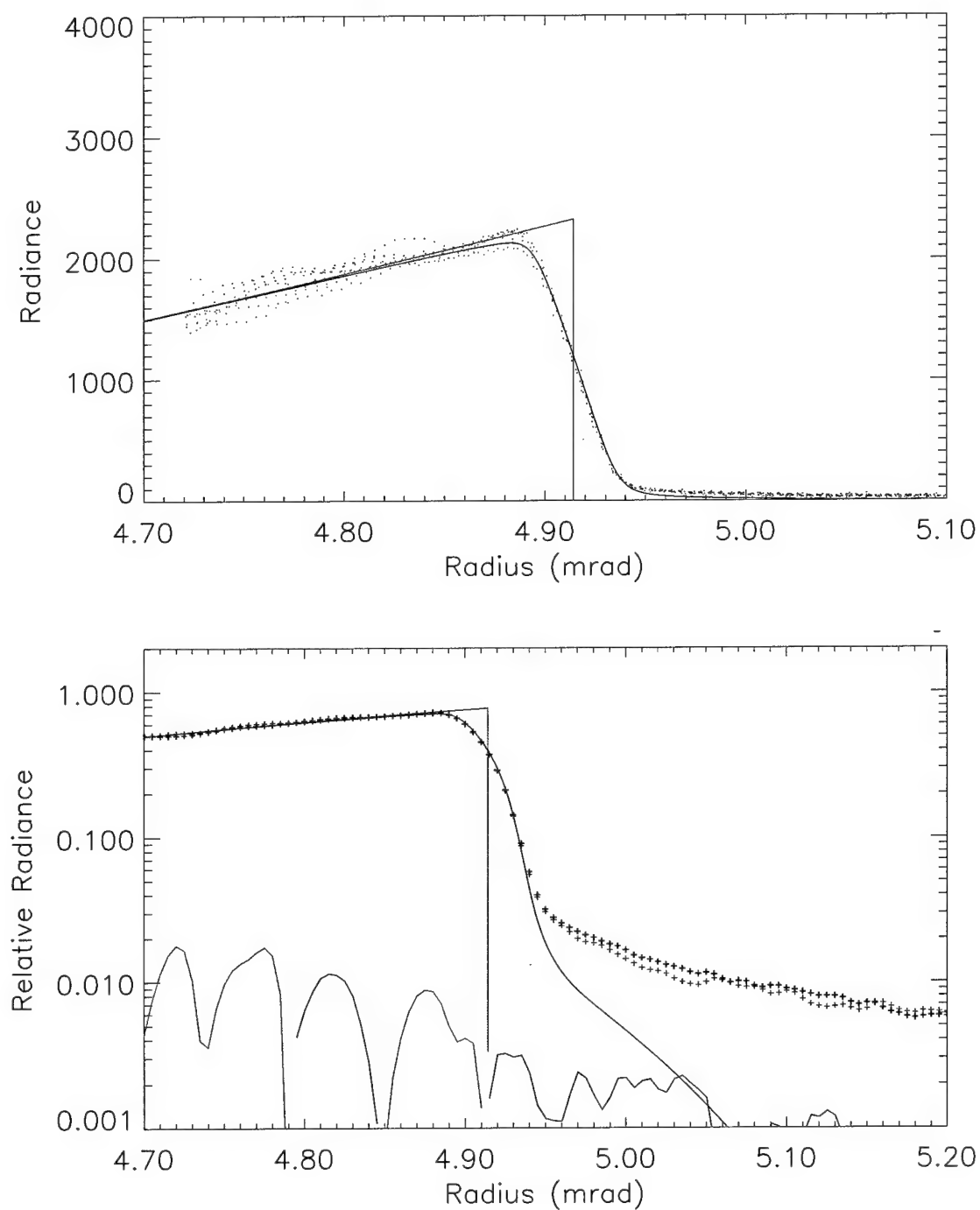
66

*Figure 50. Lunar limb profile in SCA 1, band 1,  over 44° to 49° azimuth.*

*Figure 51. Lunar limb profile in SCA 1, band 2, over 44° to 49° azimuth.*

68

*Figure 52. Lunar limb profile in SCA 1, band 3, over 44° to 49° azimuth.*

69

*Figure 53. Lunar limb profile in SCA 1, band 4, over 44° to 49° azimuth..*

*Figure 54. Lunar limb profile in SCA 1, band 4', over 44° to 49° azimuth.*

71

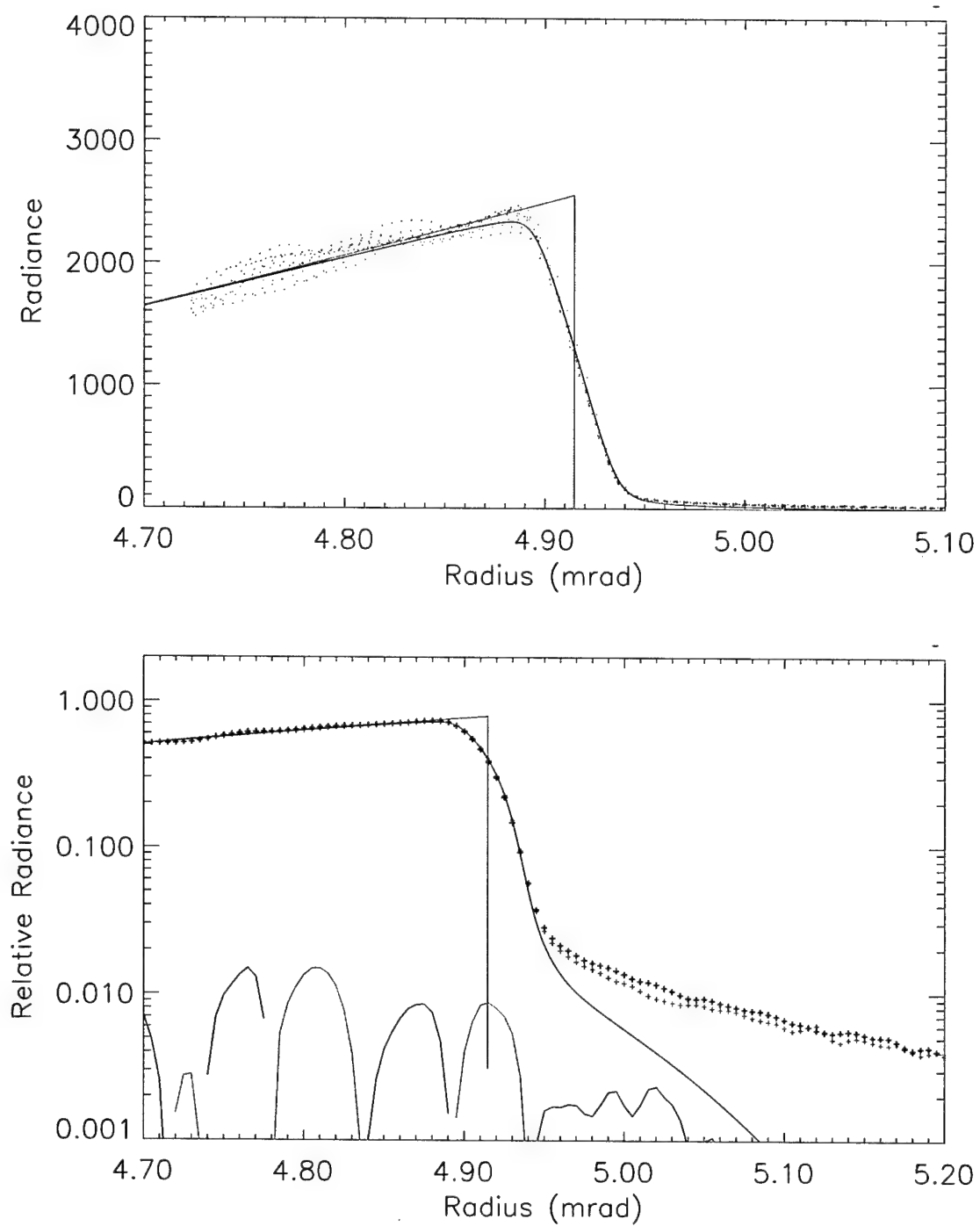*Figure 55. Lunar limb profile in SCA 1, band 5', over 44° to 49° azimuth.*

*Figure 56. Lunar limb profile in SCA 1, band 5, over 44° to 49° azimuth.*

*Figure 57. Lunar limb profile in SCA 1, band 7, over 44° to 49° azimuth.*

*Figure 58. Lunar limb profile in SCA 2, band 1', over 44° to 49° azimuth.*

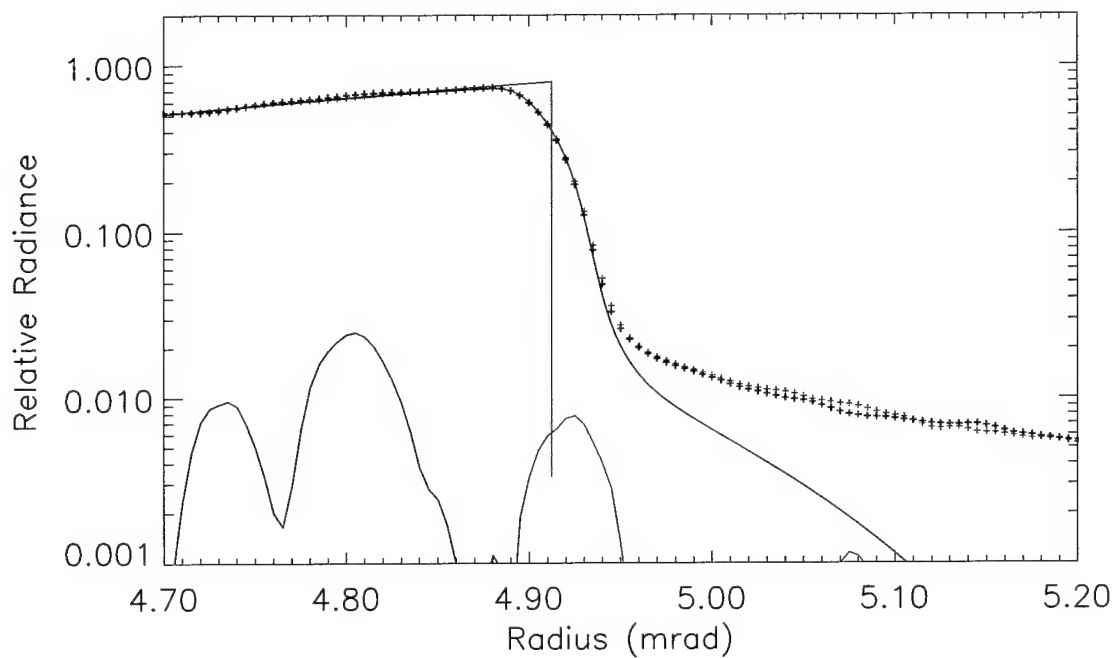*Figure 59. Lunar limb profile in SCA 2, band 1, over 44° to 49° azimuth.*
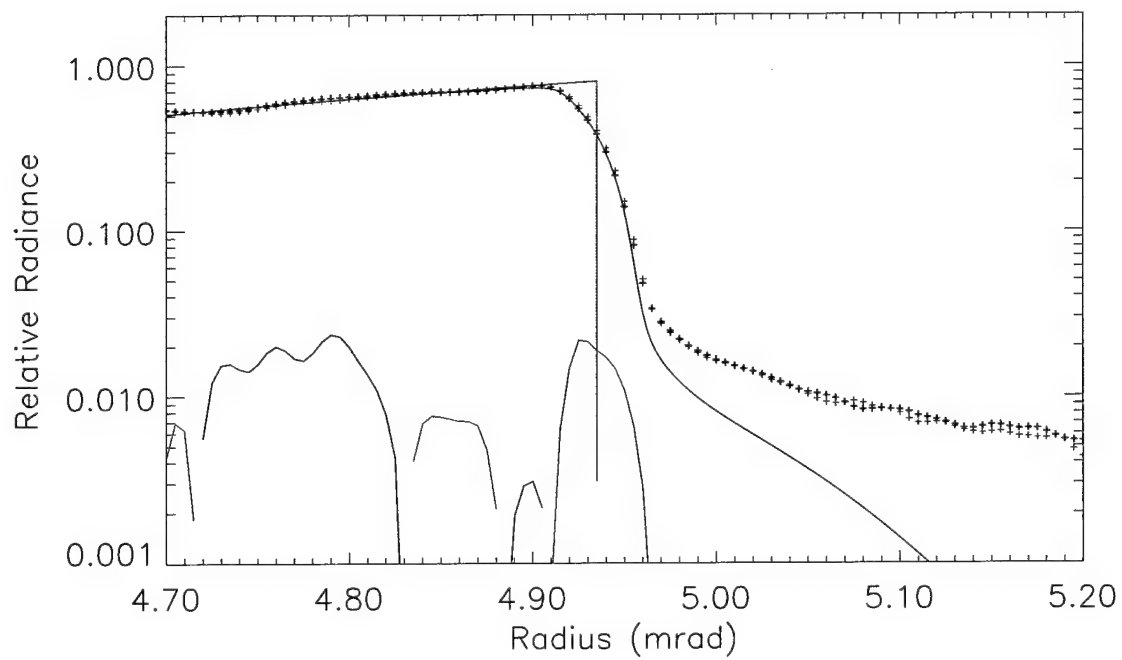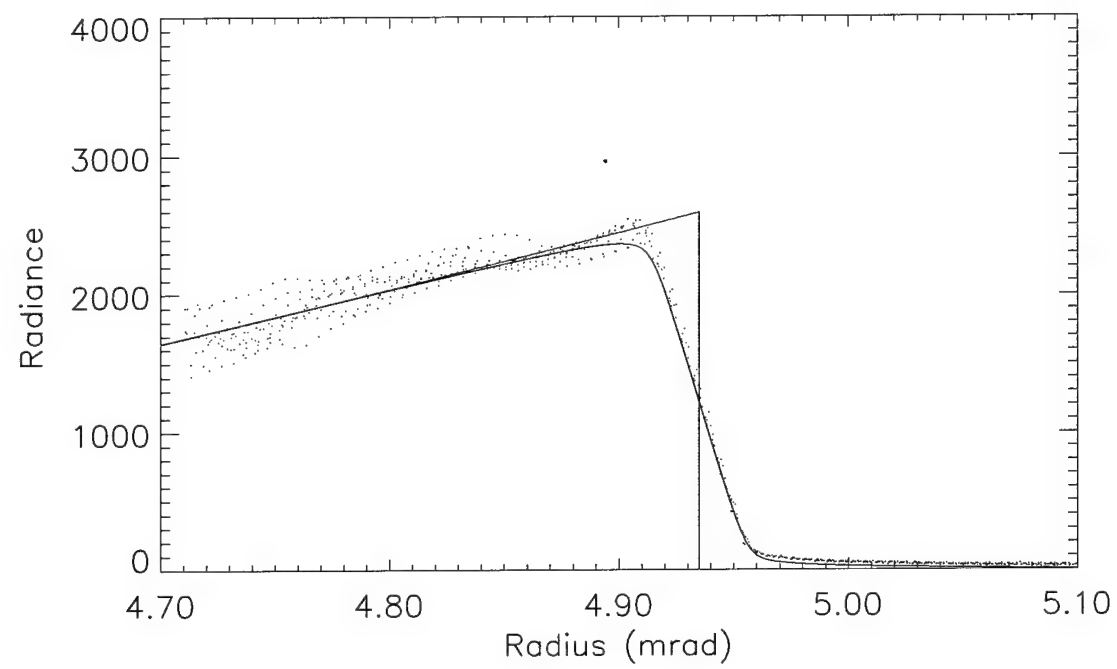
*Figure 60. Lunar limb profile in SCA 2, band 2, over 44° to 49° azimuth.*
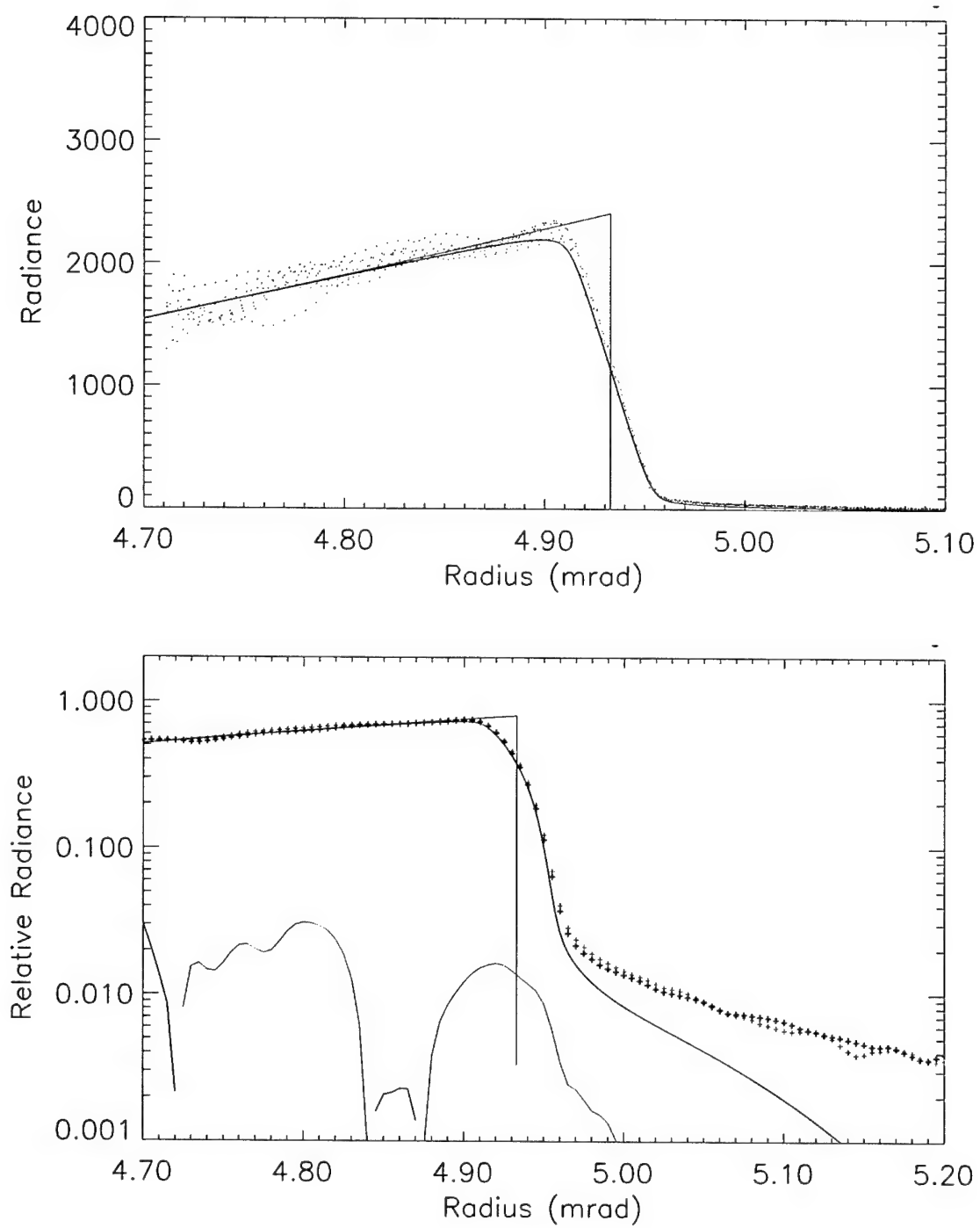
*Figure 61. Lunar limb profile in SCA 2, band 3, over 44° to 49° azimuth.*
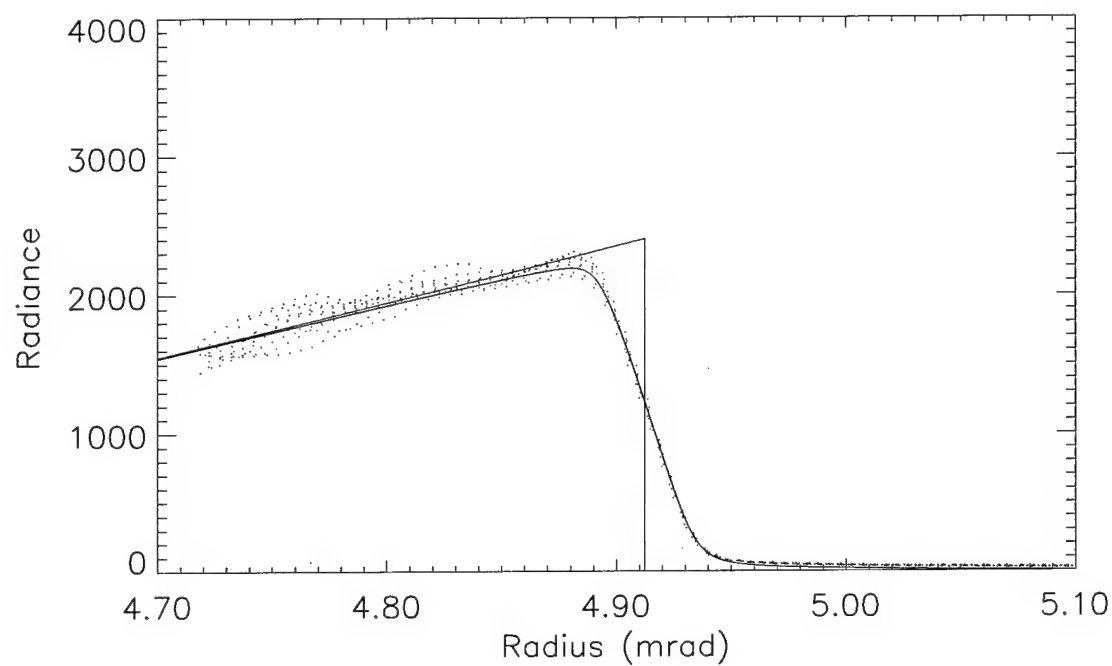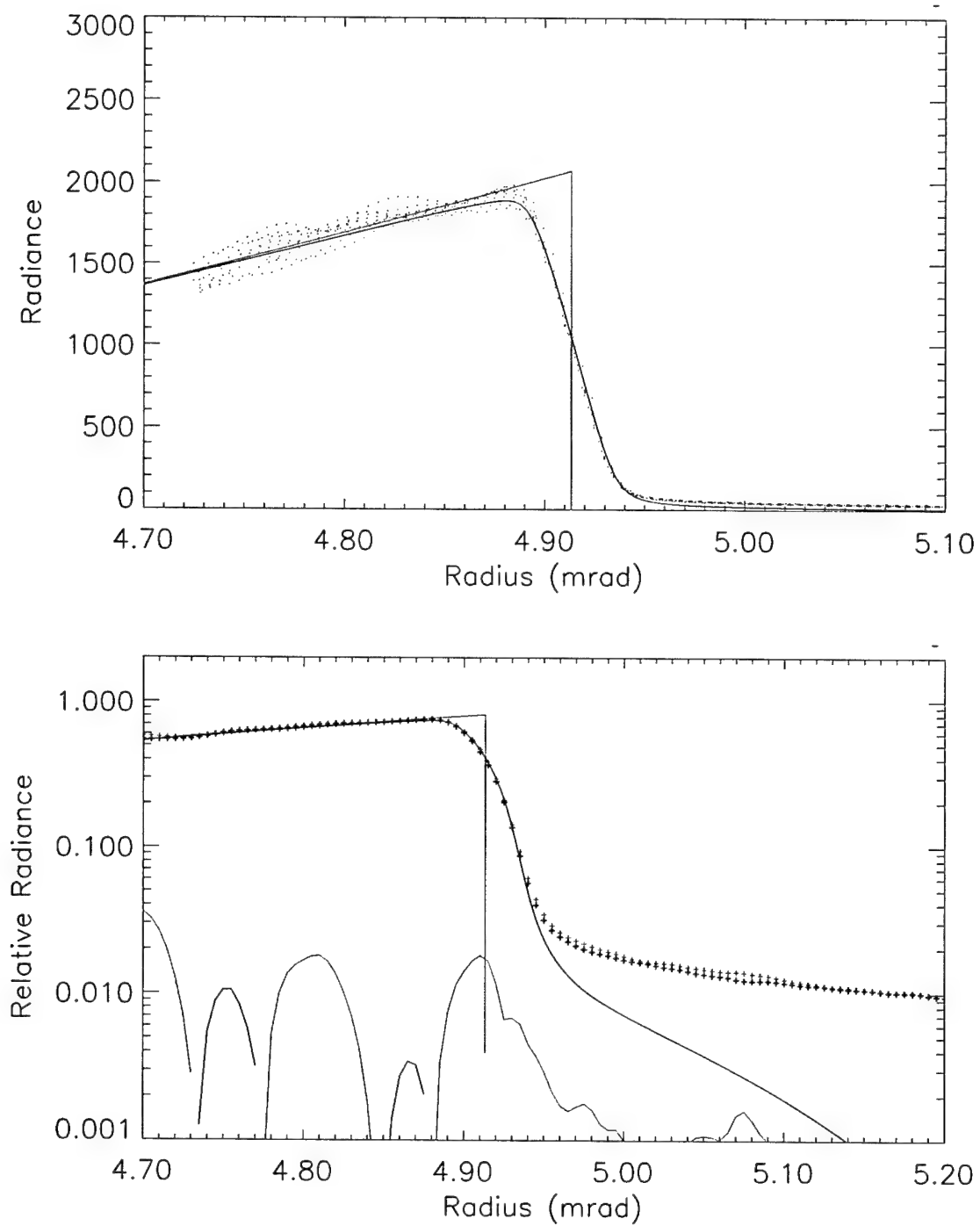
78
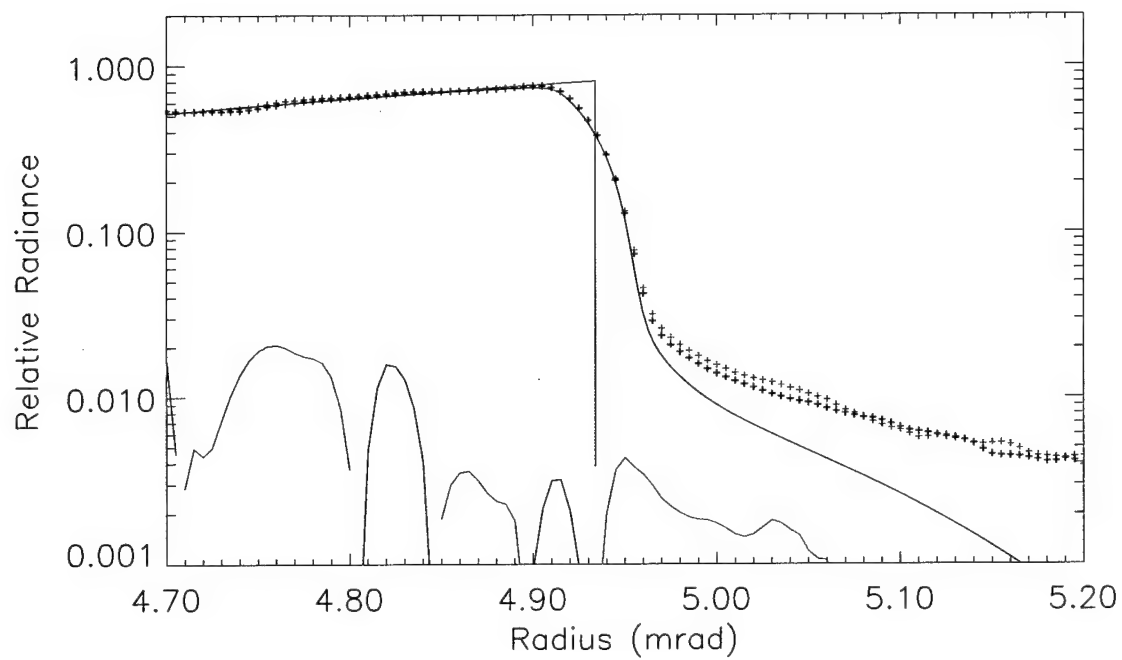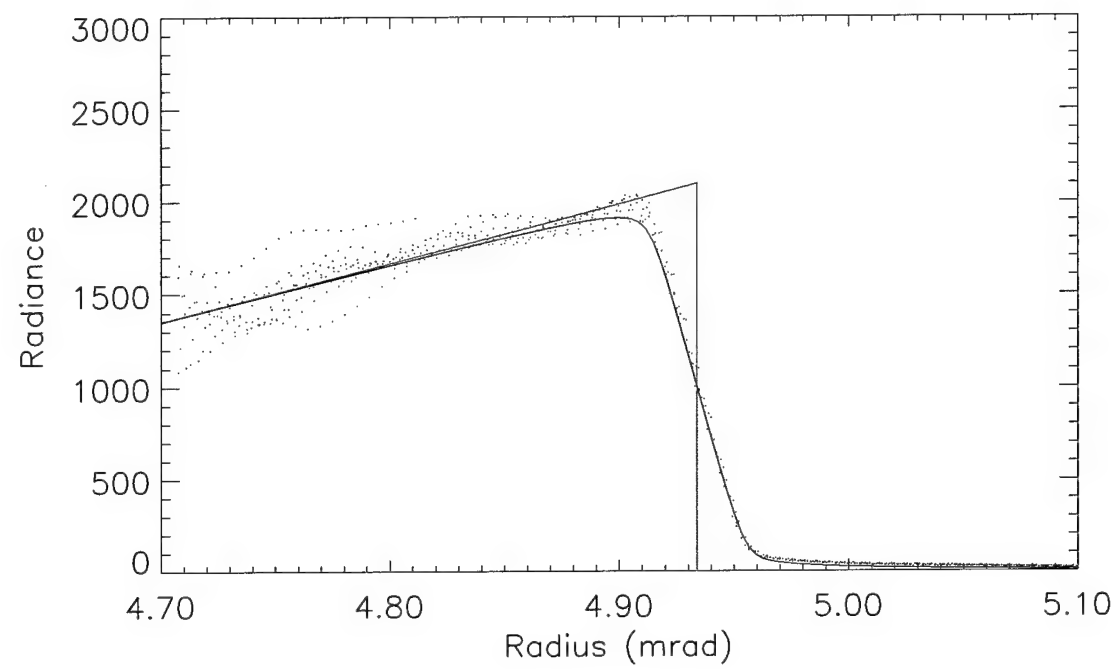
*Figure 62. Lunar limb profile in SCA 2, band 4, over 44° to 49° azimuth.*
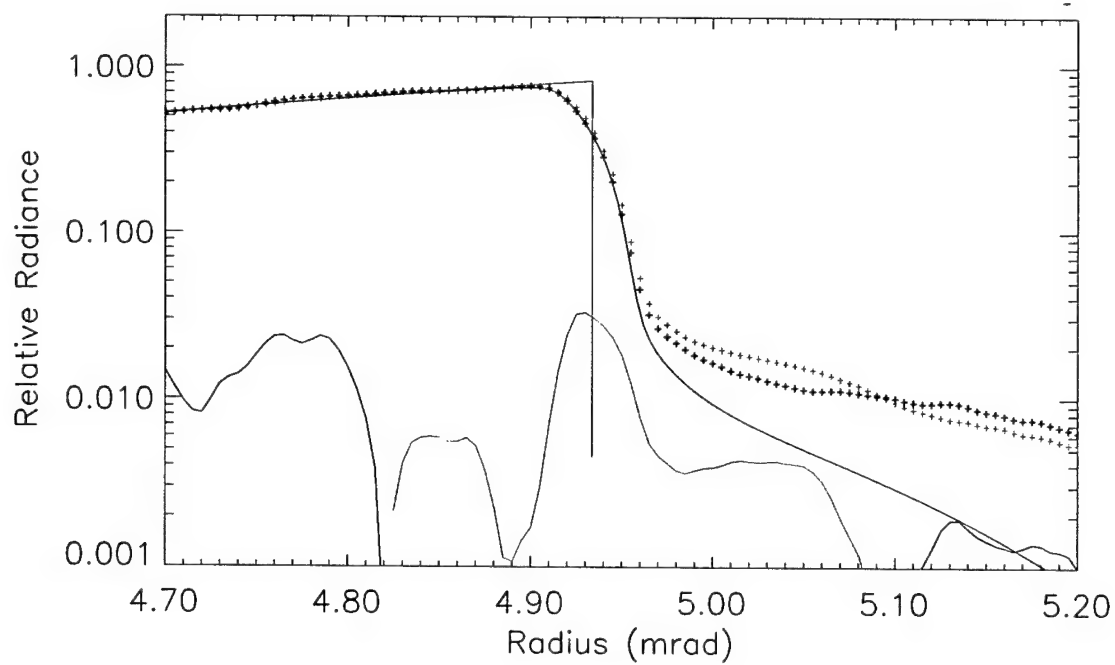
*Figure 63. Lunar limb profile in SCA 2, band 4', over 44° to 49° azimuth.*
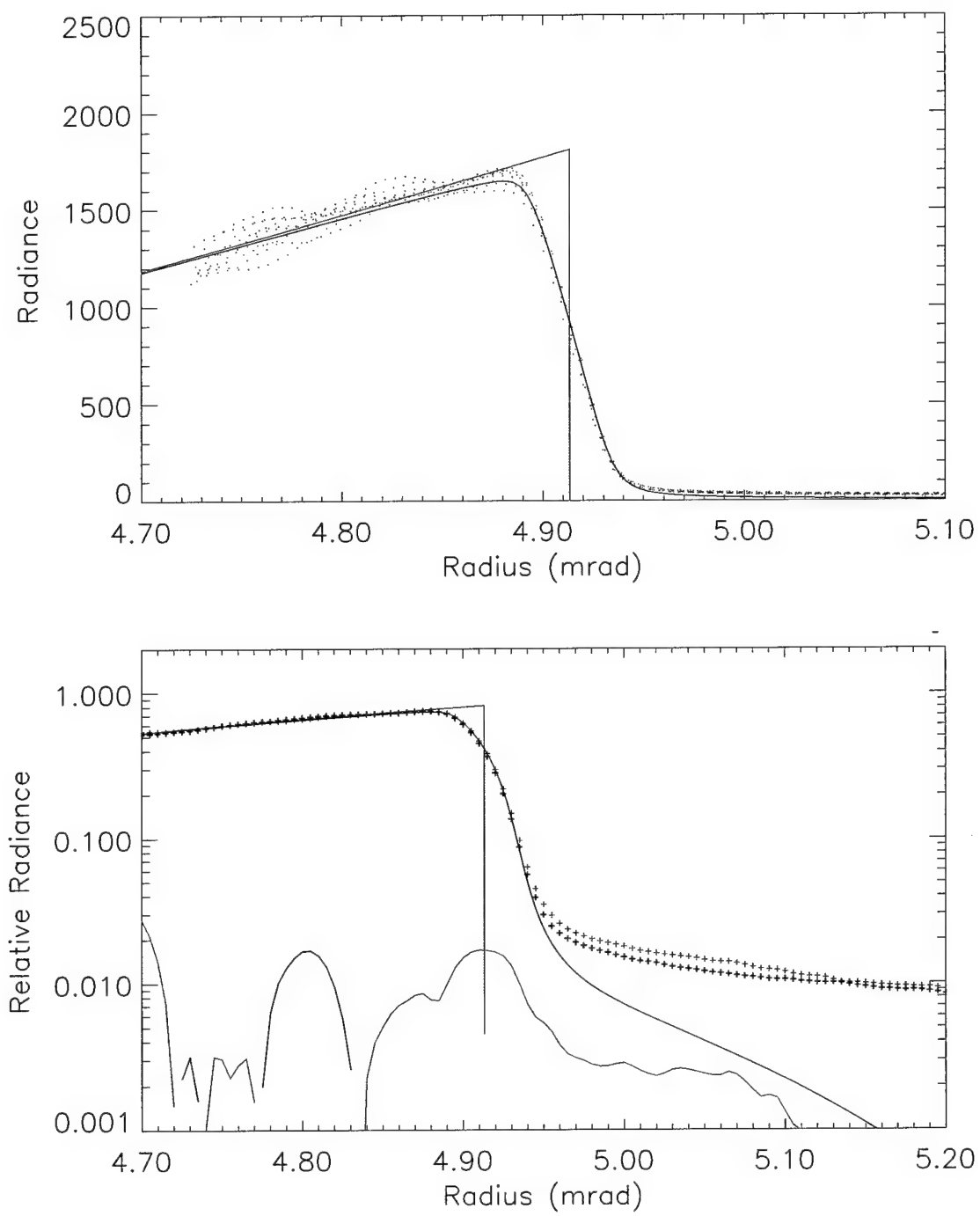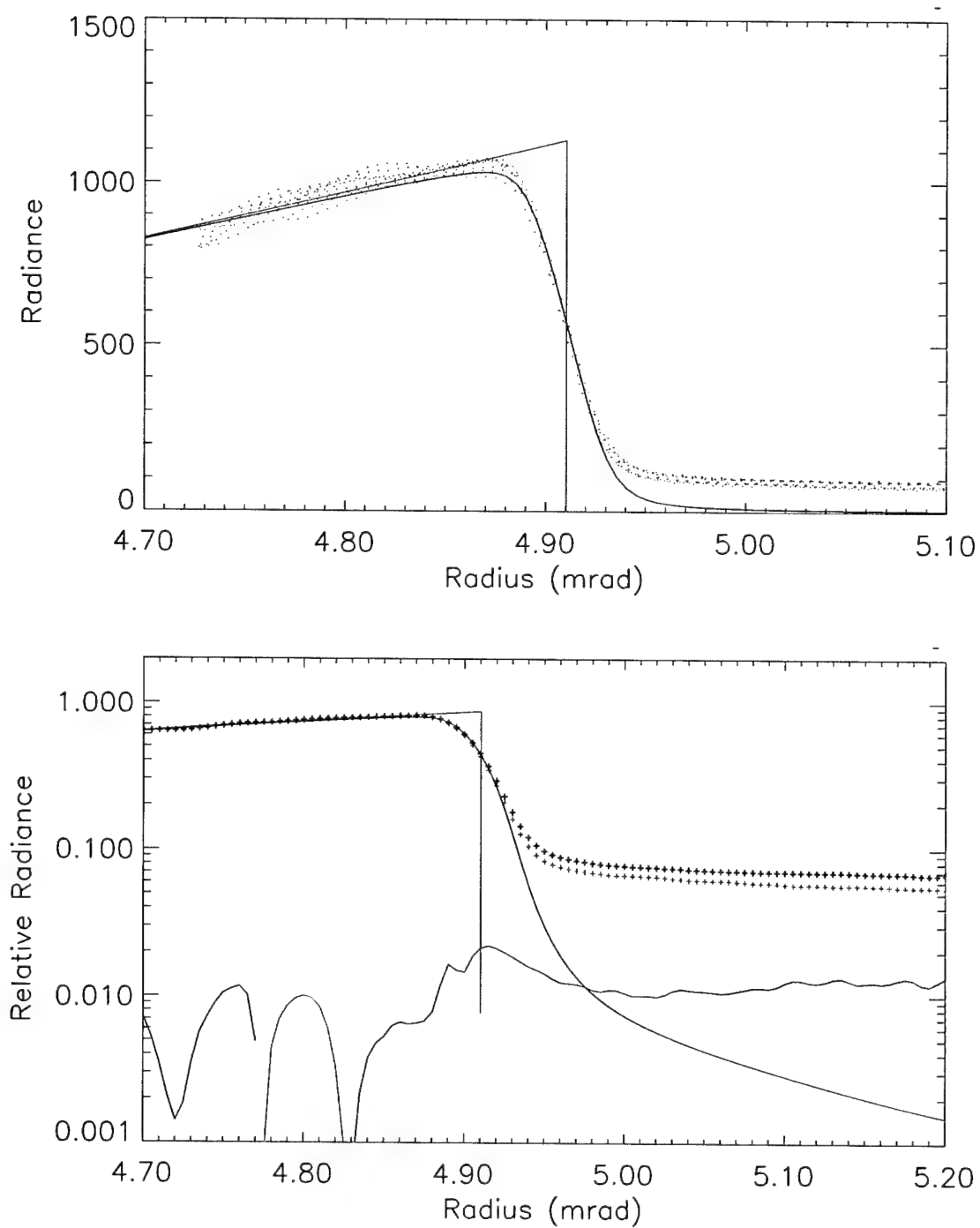
80

*Figure 64. Lunar limb profile in SCA 2, band 5', over 44° to 49° azimuth.*

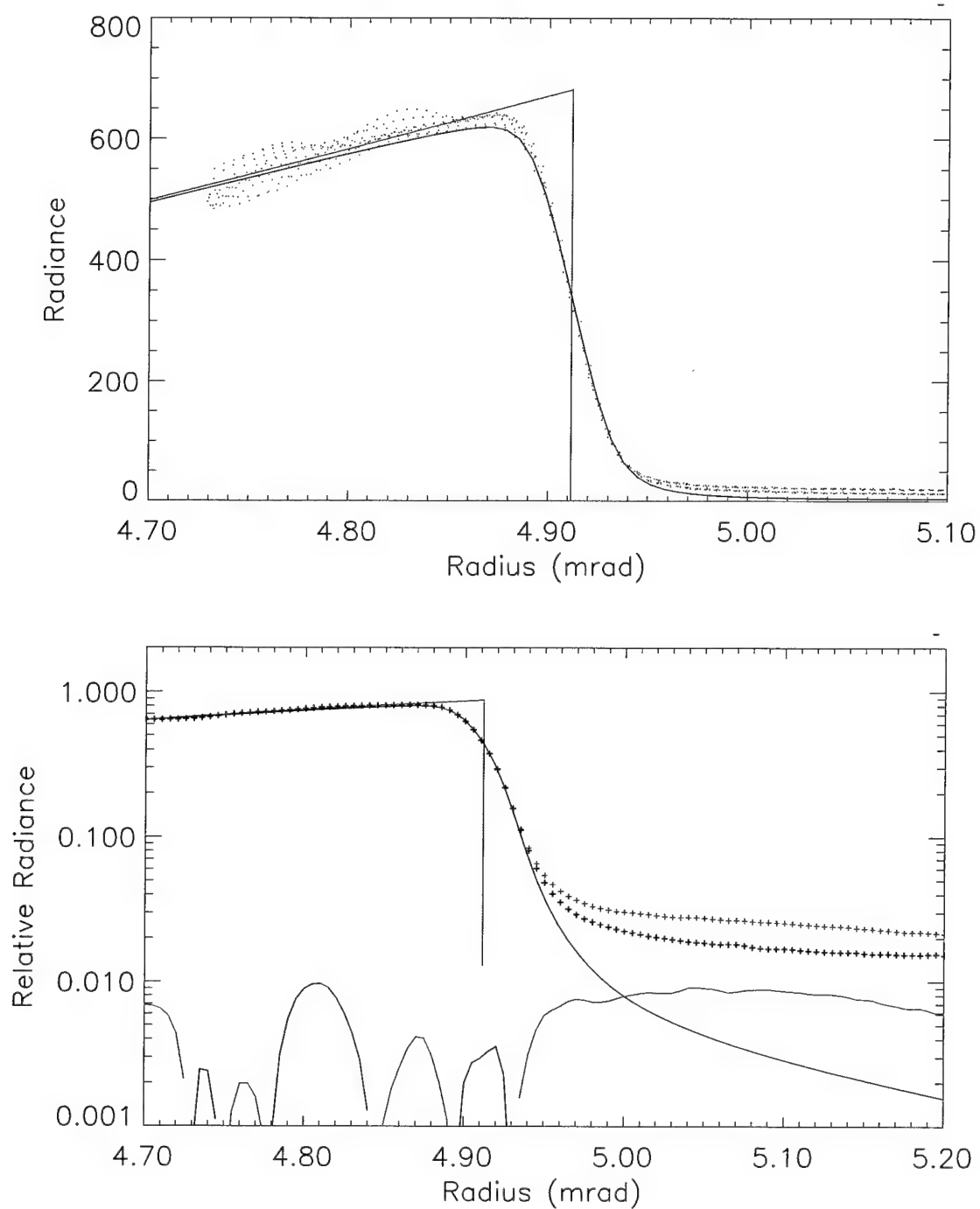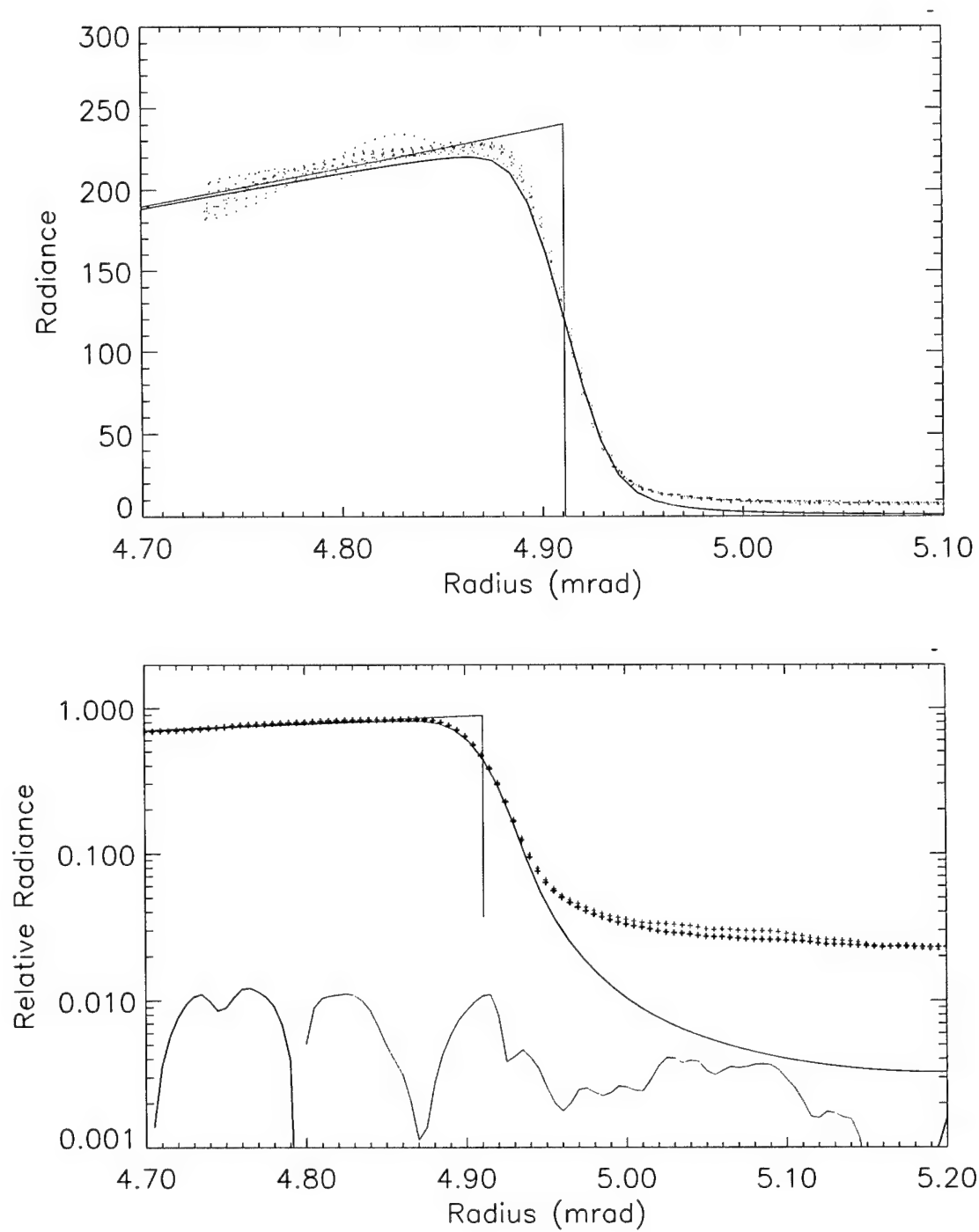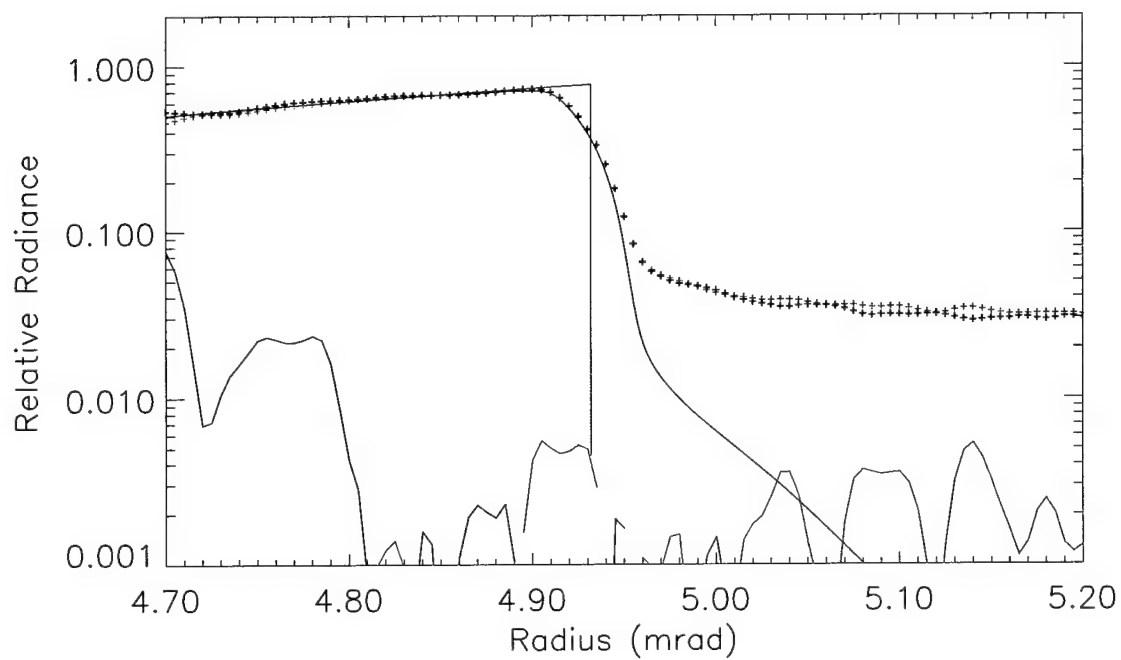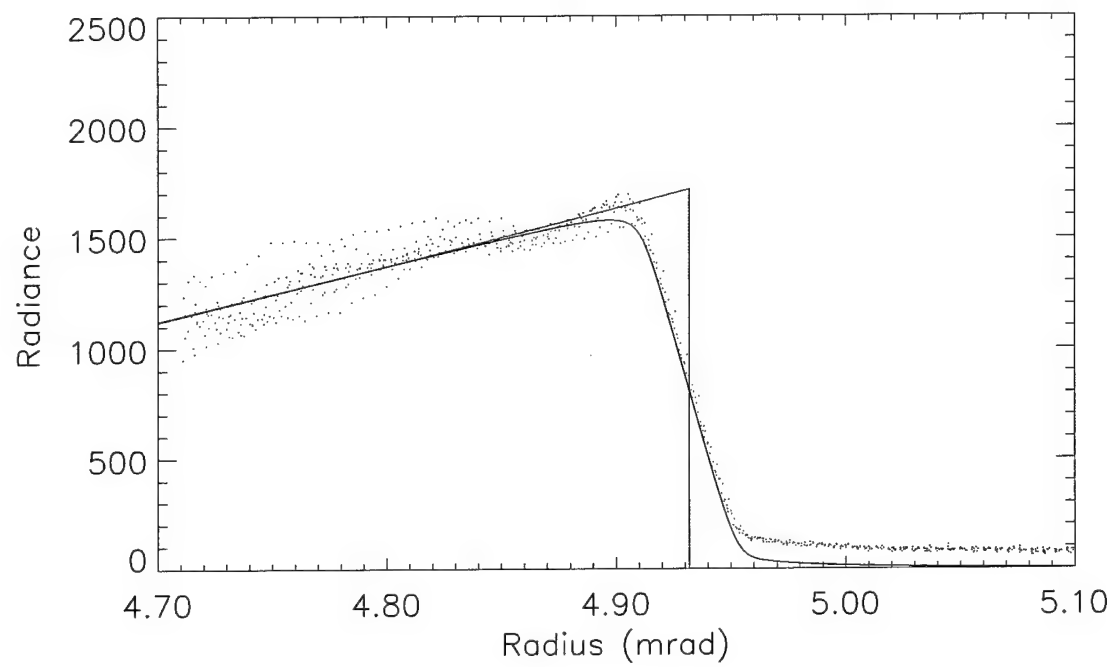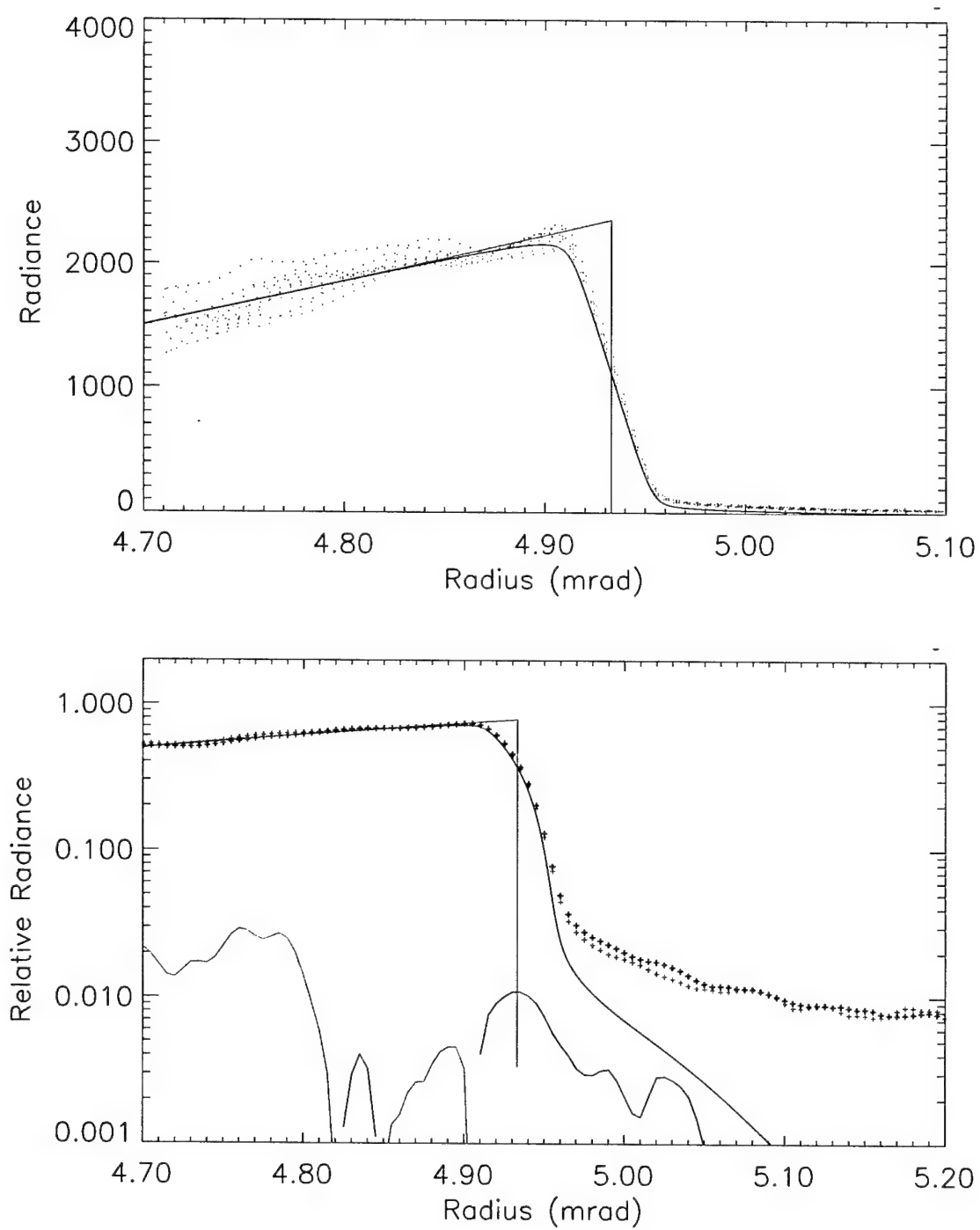*Figure 65. Lunar limb profile in SCA 2, band 5, over 44° to 49° azimuth.*

82
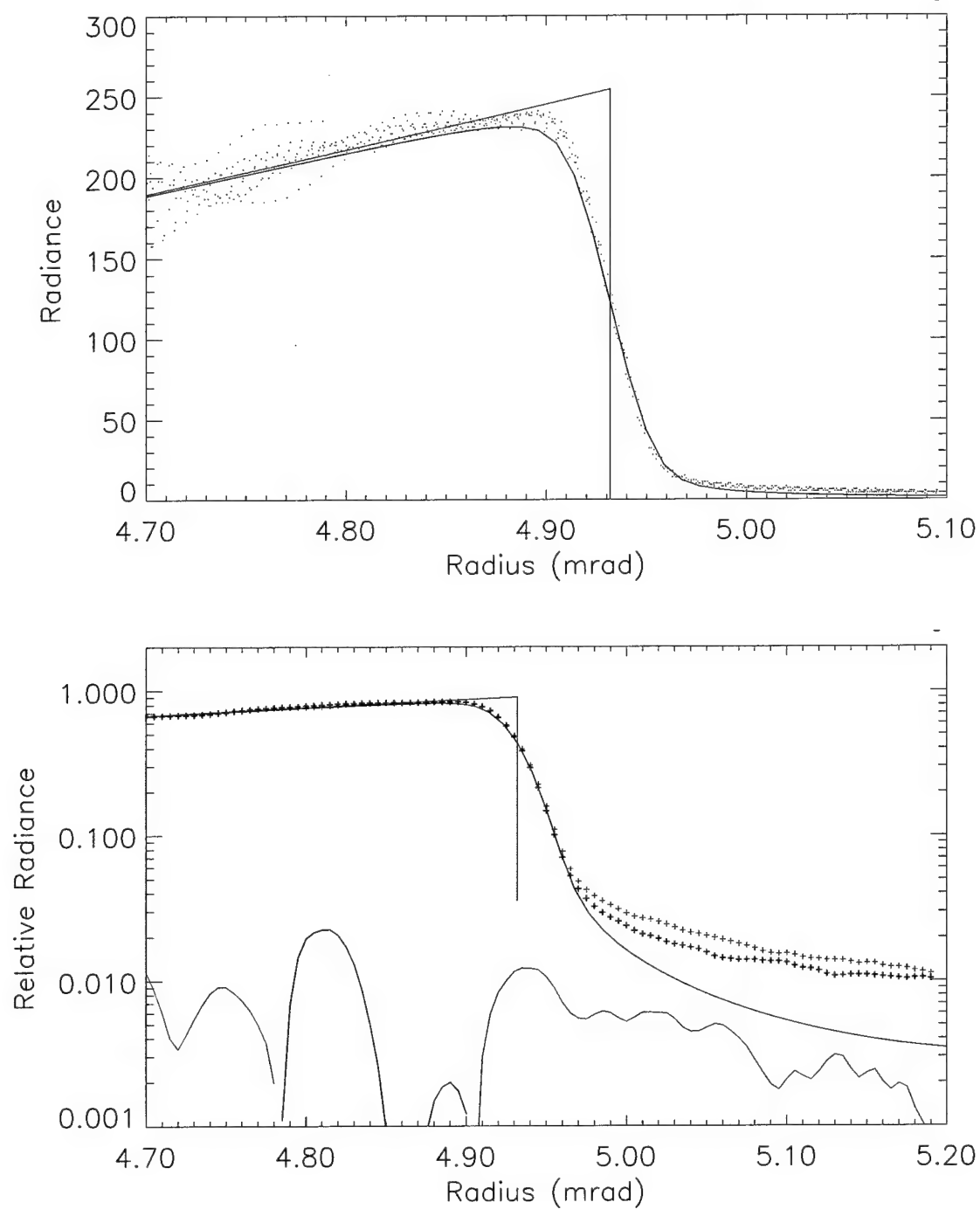
*Figure 66. Lunar limb profile in SCA 2, band 7, over 44° to 49° azimuth.*

83

For bands 1 through 4', the excess radiance falls below 1% of the limb radiance within 250 μrad of the limb. For the SWIR bands (5, 5', and 7), as discovered earlier by Mendenhall, the odd SCA's show a strong "ghost" image, as large as 6% of the direct image. It is particularly strong in band 5'. The ghost is thought to originate from light scattered at the stepped joint between the VNIR and SWIR filters [7]. We show the SWIR limb profiles from SCA's 3 and 4 in Figure 67 through Figure 72. The 1' band of the even SCA's also shows a similar ghost image. The source of this ghost is unknown at this time. For this observation, the apparent amplitudes of the ghost in each band and SCA at 250 μrad from the limb are tabulated in TABLE 1.

Following standard operating procedures for the ALI, the scans analyzed here carried the lunar image first across the SWIR detectors, then the VNIR detectors (from band 7 toward the Pan band). We have shown here the radiance data only for the portion of the limb in full sunlight. For SCA's 1 and 3, the lunar image was mostly over the VNIR detectors while the sunlit limb intersected the joint between the VNIR and SWIR filters. Light scattered from the joint toward the SWIR detectors could therefore be seen against the space background. For SCA's 2 and 4, the SCA orientation is reversed, and the SWIR detectors were viewing the moon while the sunlit limb intersected the joint, thus masking the ghost. For the 1' band, a ghost appears in SCA's 2 and 4, but not 1 and 3. This suggests that if a similar mechanism to the SWIR ghost is at work in band 1', then the source of this ghost is toward the longer-wavelength bands (1 to 7), rather than the nearby edge of the mounting bezel. It remains unclear whether either ghost is a purely optical effect, or possibly an electronic artifact.

## TABLE 1

### Relative Lunar Ghost Image Amplitudes[a]

| SCA | Band 1' | | Band 5' | | Band 5 | | Band 7 | |
|---|---|---|---|---|---|---|---|---|
| | even | odd | even | odd | even | odd | even | odd |
| 1 | 1.0% | 1.4% | 6.5% | 8% | 2.6% | 1.8% | 2.6% | 2.6% |
| 2 | 4.1% | 3.8% | 1.8% | 1.9% | 0.7% | 0.7% | 1.4% | 1.2% |
| 3 | 1.0% | 1.0% | 3.1% | 3.6% | 1.6% | 1.0% | 1.3% | 1.8% |
| 4 | 4.1% | 3.9% | 0.9% | 0.9% | 0.6% | 0.5% | 0.5% | 0.7% |
| [a] Radiance at 250μrad from limb ÷ peak of model limb radiance. | | | | | | | | |

84
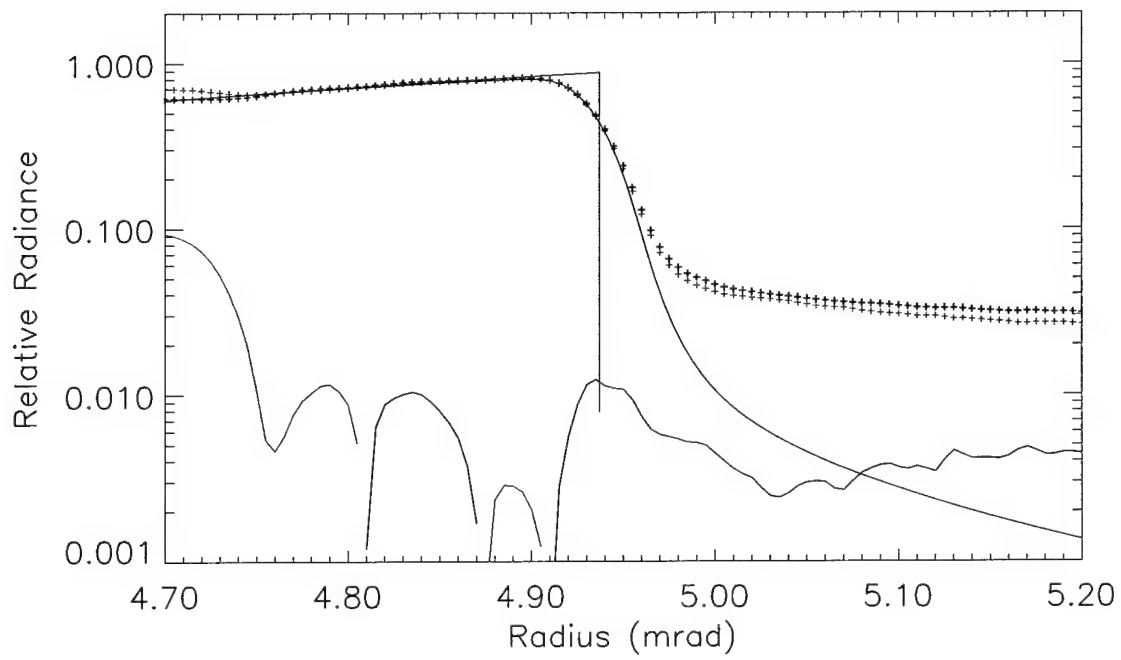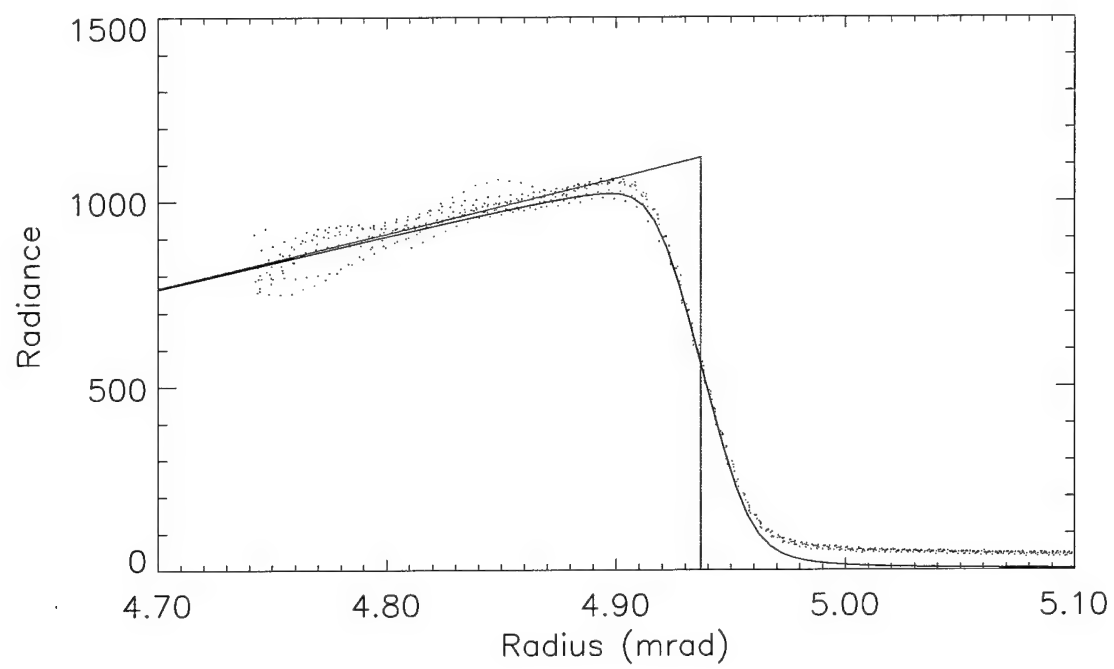
*Figure 67. Lunar limb profile in SCA 3, band 5', over 44° to 49° azimuth.*
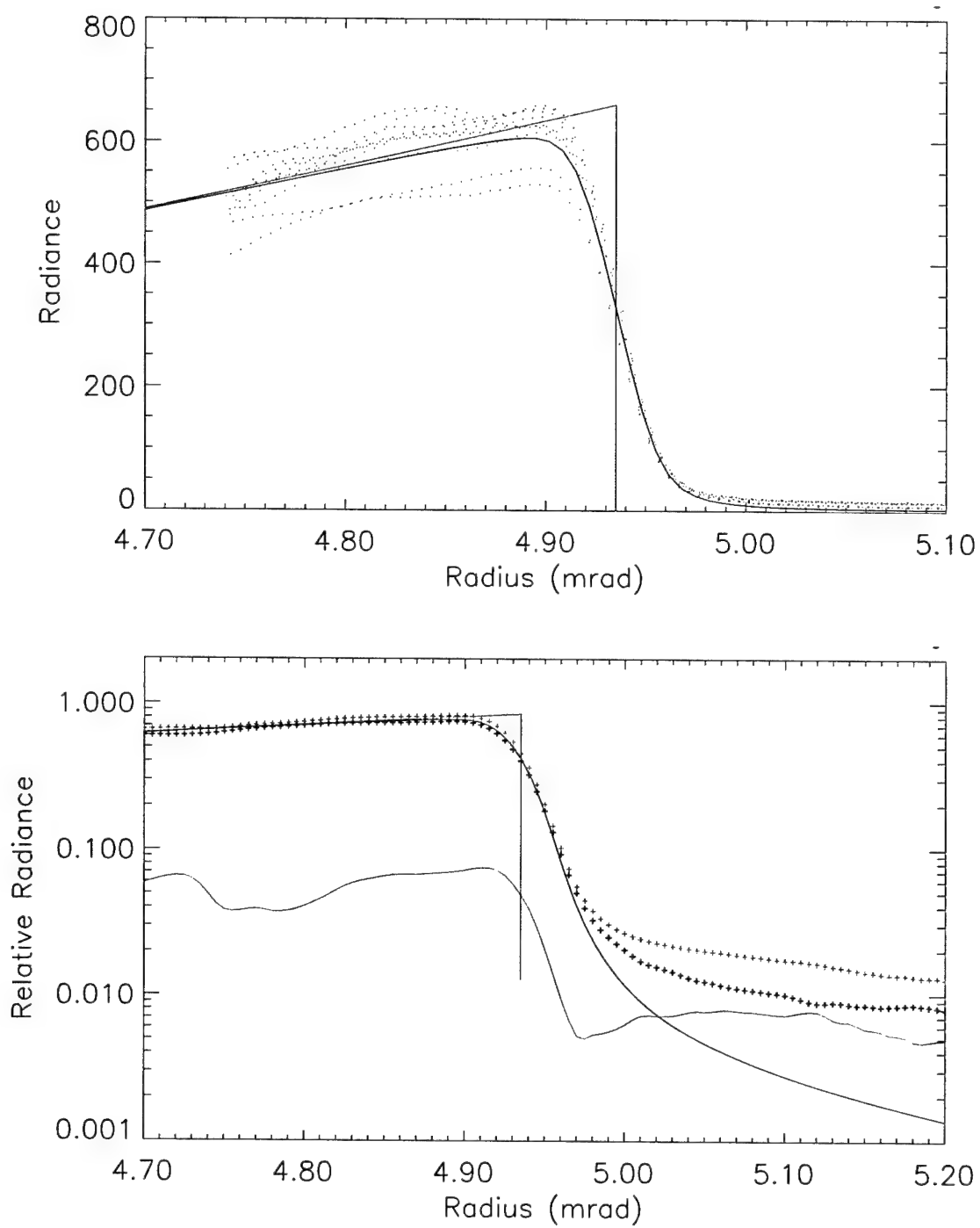
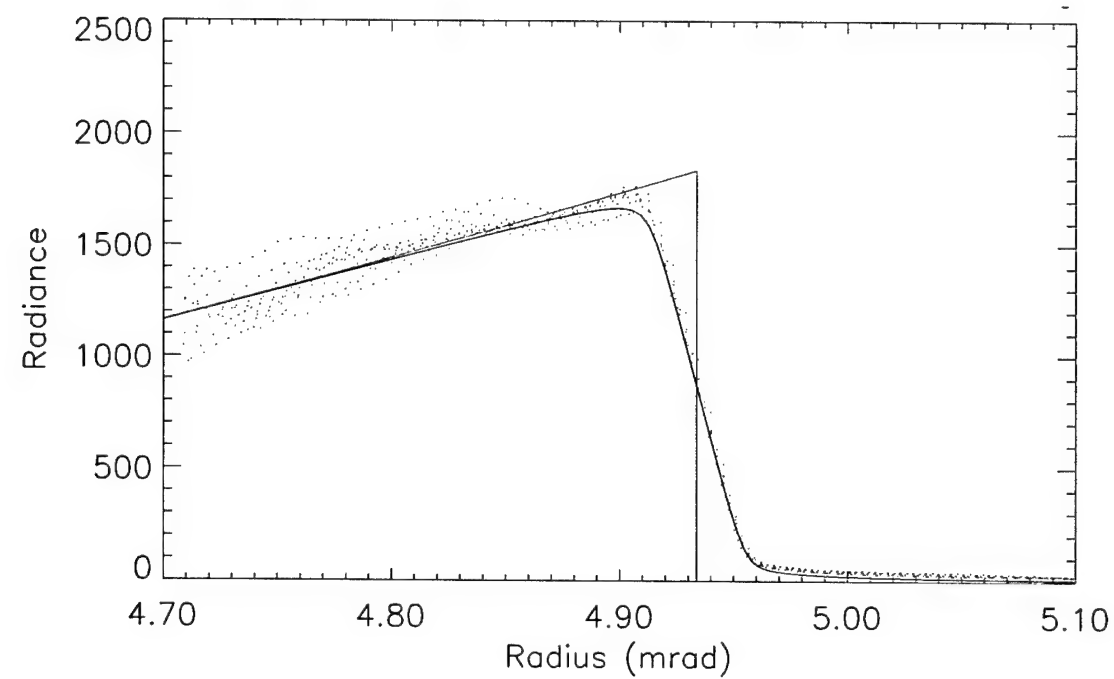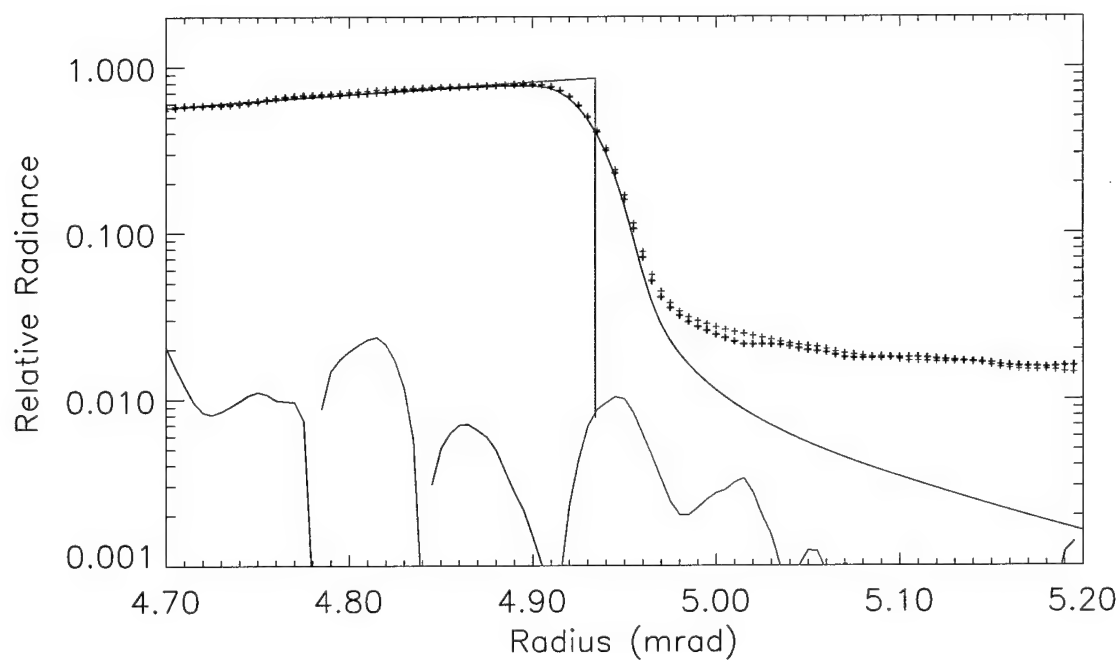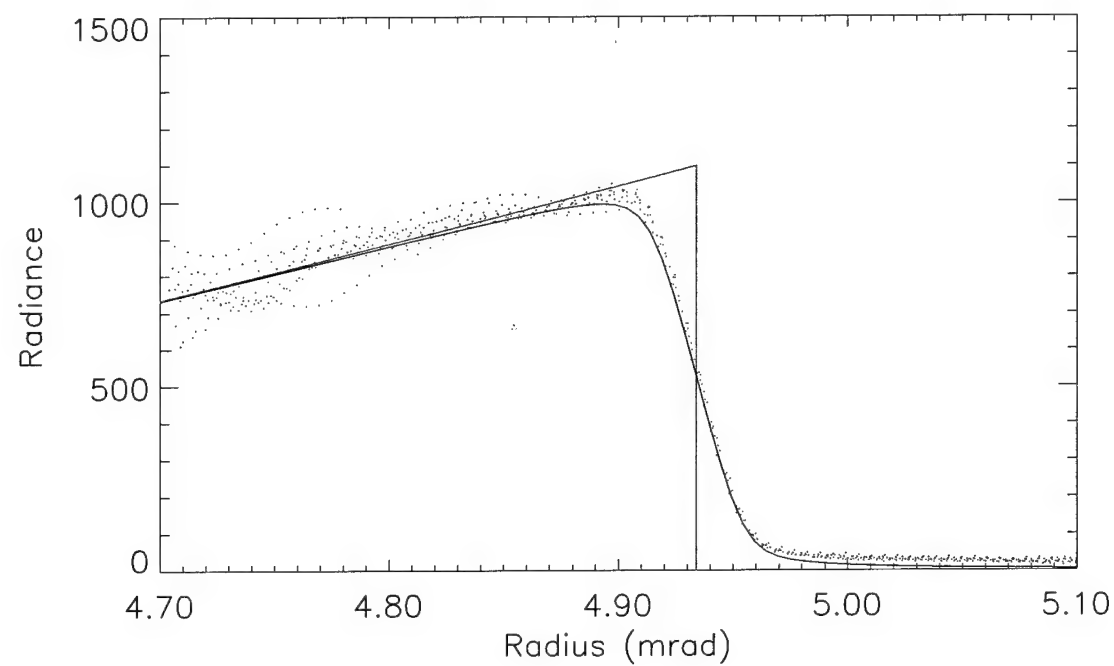*Figure 68. Lunar limb profile in SCA 3, band 5, over 44° to 49° azimuth.*

86
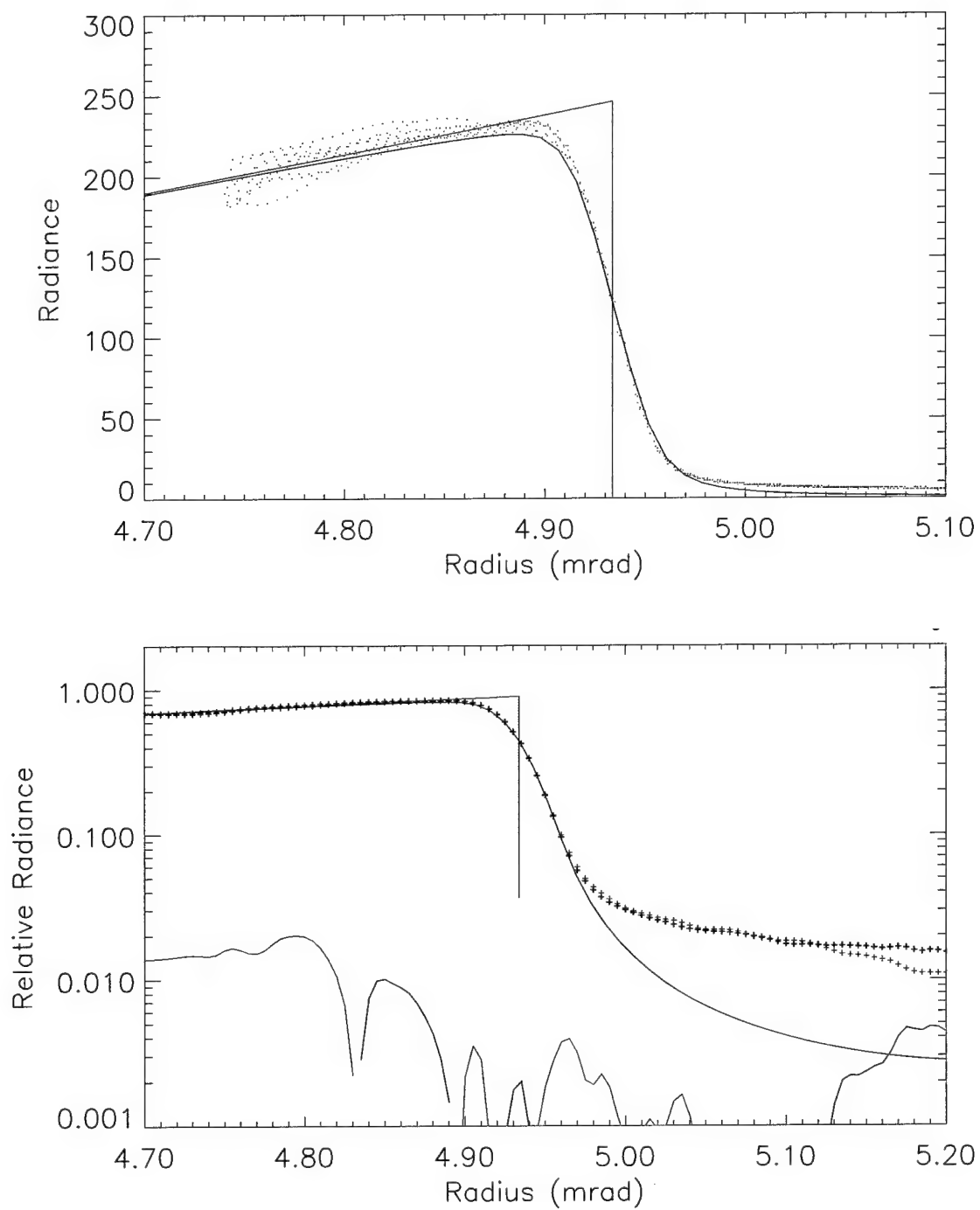
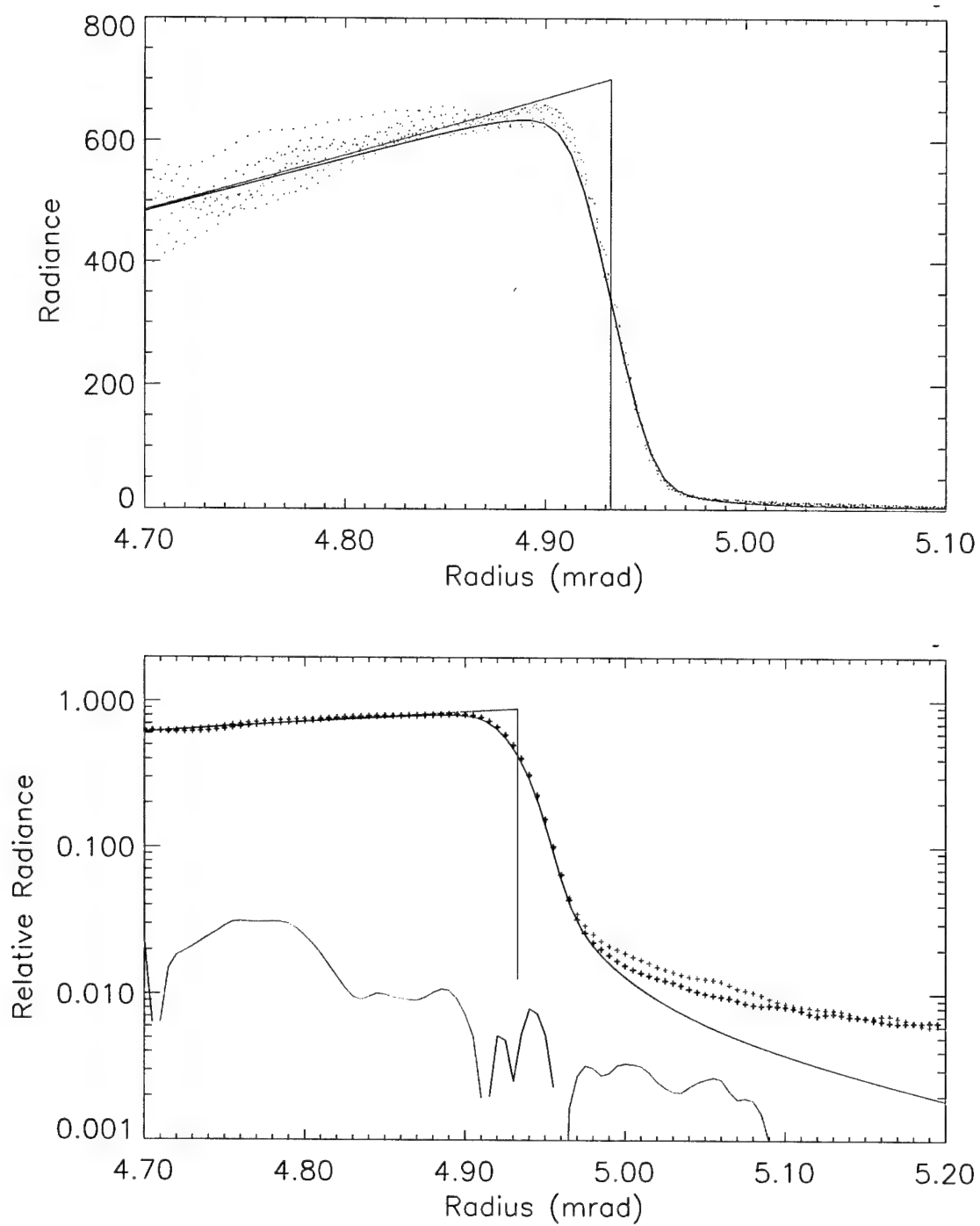*Figure 69. Lunar limb profile in SCA 3, band 7, over 44° to 49° azimuth.*
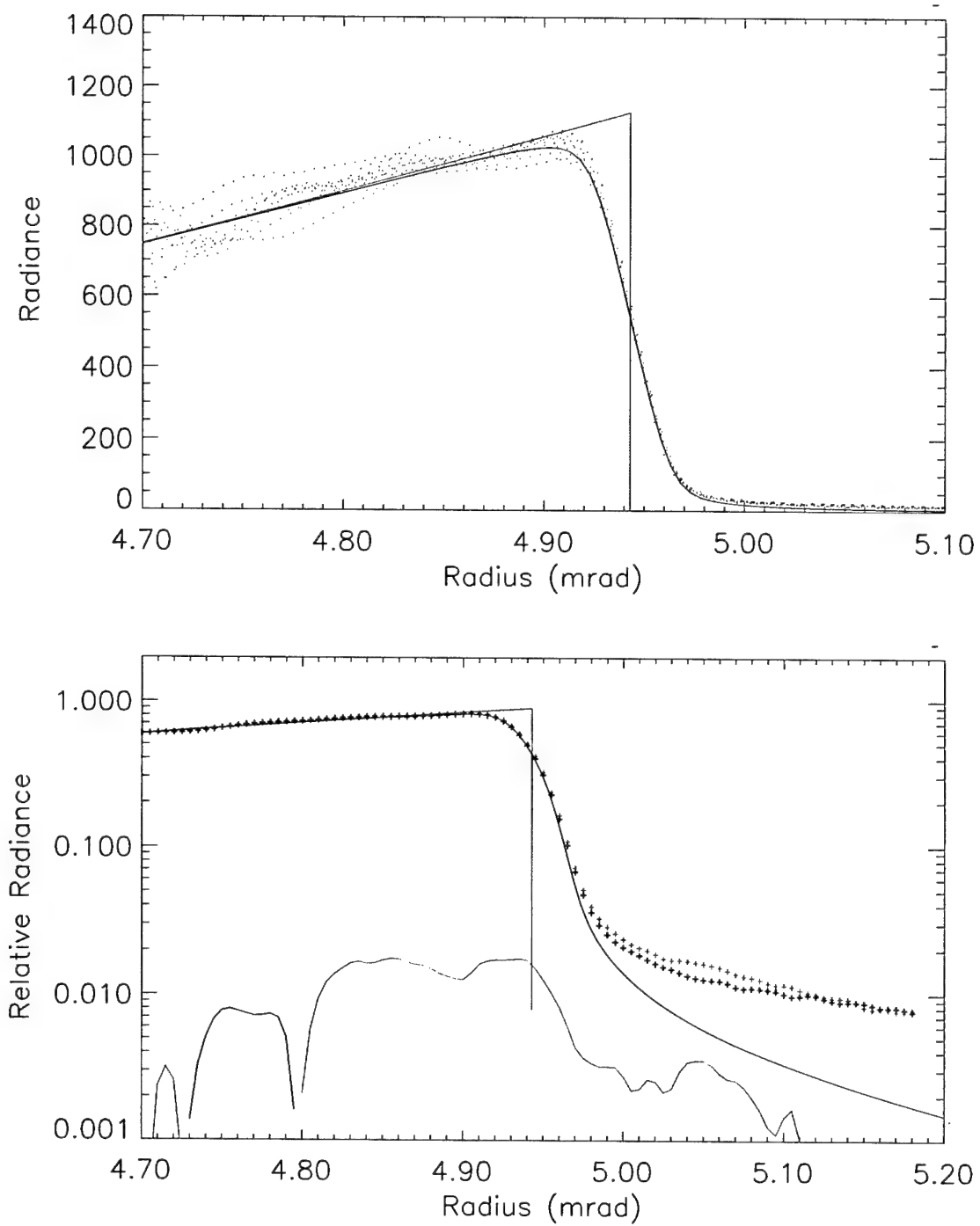
*Figure 70. Lunar limb profile in SCA 4, band 5', over 44° to 49° azimuth.*

88
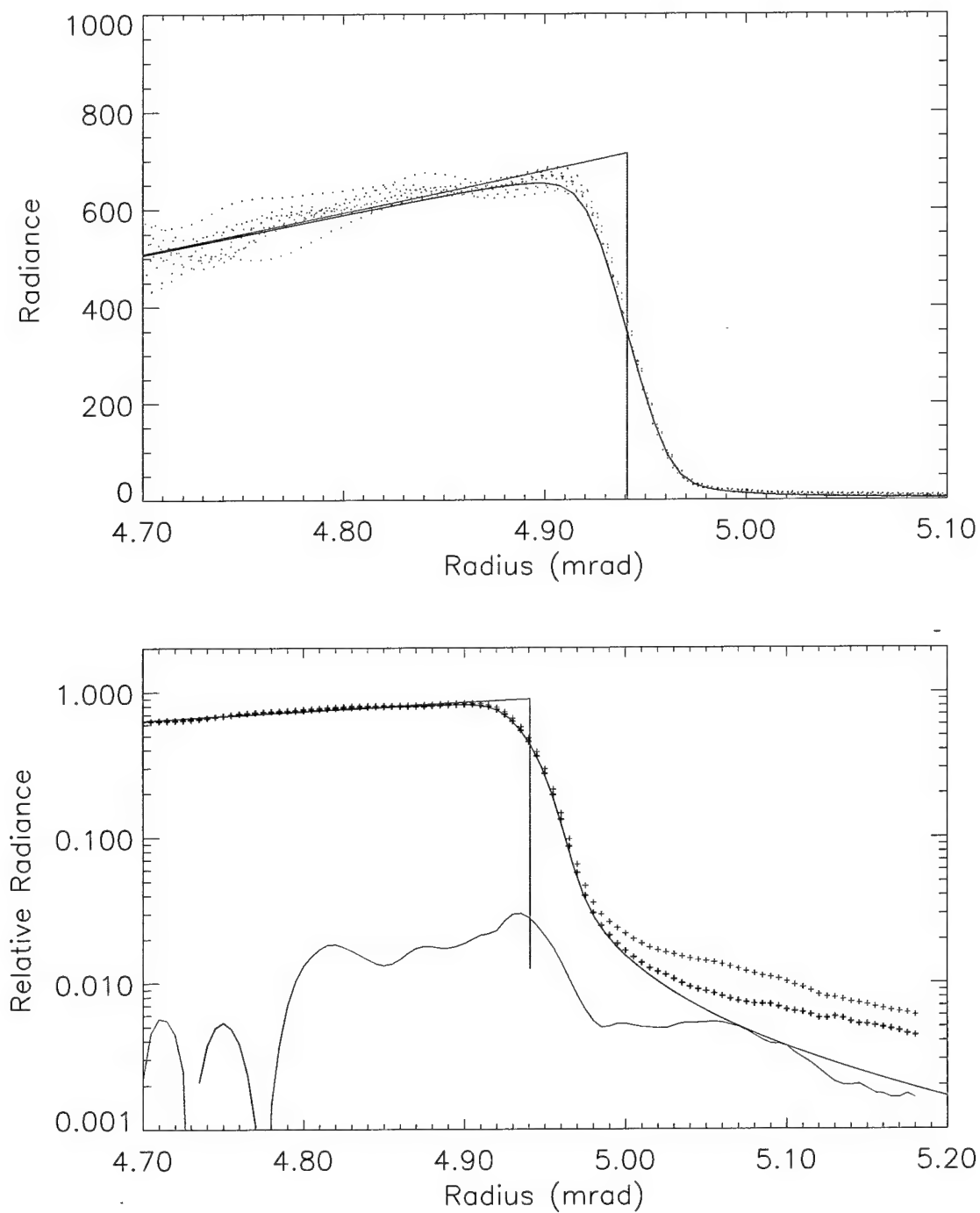
*Figure 71. Lunar limb profile in SCA 4, band 5, over 44° to 49° azimuth.*
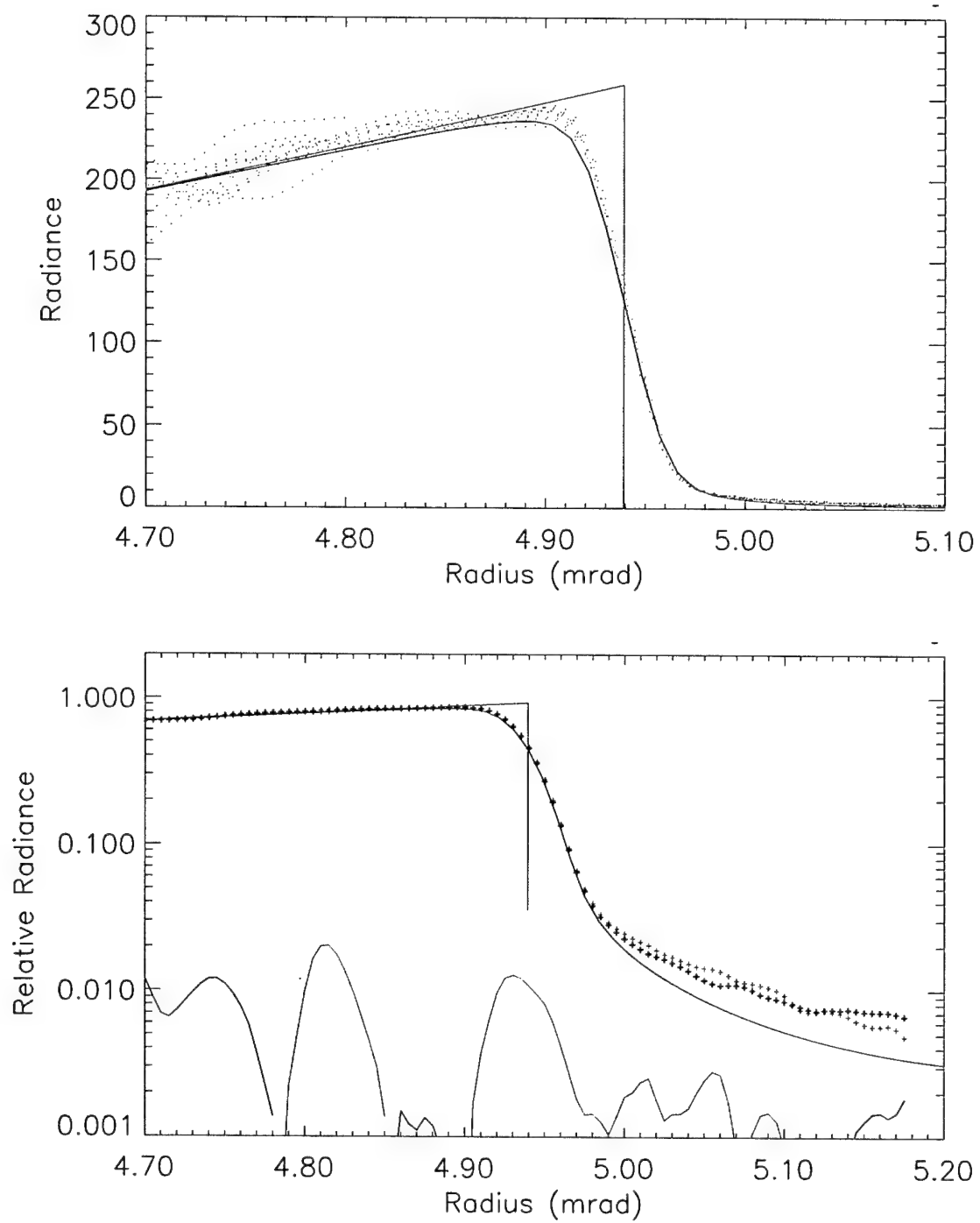
*Figure 72. Lunar limb profile in SCA 4, band 7, over 44° to 49° azimuth.*

The foregoing analysis of a lunar calibration scan lends weight to the basic conclusion of Section 4, that the Spatial Transfer Function model derived from the pre-flight calibration process accurately describes spatial response of the ALI near a sharp edge. Beyond ~30 μrad from an edge however, there is a definite excess response above that expected from the model STF. The decrease in response with distance from the edge becomes much more gradual than the model STF would indicate. At 250 μrad from an edge, the excess is 0.2 – 2.0% of the radiance at the edge. In addition, there are apparent ghost image effects seen in certain bands. These effects were undetectable from the bridge profiles, because they are too small to distinguish from possible radiance variations of the water backgrounds there.

The basic excess response is probably attributable to scattering from the mirror surfaces, which were known to have an imperfect finish when the instrument was fabricated. Contamination on the surface of the filters must also contribute an undetermined amount to these effects. For convenience, we will refer to the excess response at large angles as "scattered light," though phenomena other than scattering may contribute to it. With the exception of the ghost seen in SCA 1, band 5' however, all of these effects are below 5% of the direct source radiance. The extreme case of the sunlit lunar limb, seen next to the black of space, was required to make evident the presence of the scattered light. Limitations of the optical equipment employed in the pre-flight spatial calibrations made it difficult to observe this low level of scattered light. Even if it were detected at that time, it could not have been unambiguously attributed to the ALI rather than the calibration equipment.

# 6. STELLAR AND PLANETARY SCANS

As a further test of spatial resolution and pointing accuracy, we desired scans of bright stars. The positions of the stars are precisely known. Their *apparent* positions, as imaged by the ALI, should provide an additional check on the alignment of the ALI relative to the Attitude Control System (ACS), as well as the validity of the detector LOS map. For this report however, we are solely concerned with the spatial resolution. Star images should represent the point-spread function (PSF) of the instrument. This is a more direct measure of the spatial resolution than the edge- spread functions obtained, for example, from a lunar scan. Since we were uncertain whether the stars would be bright enough to provide good images, scans of several bright planets were also planned and executed.

## 6.1 PLANETS

The angular speed of the planet and star scans was set at approximately 2.37 mrad/s, or one-fourth the angular speed of the earth as seen by the ALI during a normal data collection event. The sky scene is thus over-sampled in the scan direction. Image maps in celestial coordinates were created, centered on the apparent Right Ascension (RA) and Declination (Dec) of each planet. The radiance data were re-sampled to the maps by reference to the telemetry data. This process required some image-by-image adjustments to the ALI-to-ACS alignment parameters, and to the timing relationship between the telemetry readings and the focal plane data frames, in order to center the planets in the maps. The shifts are of order 1.5 mrad in roll, 0.7 mrad in pitch (or timing), and 8 mrad in yaw. Our knowledge of the details of the processing and formatting of the focal plane and telemetry data at GSFC is inadequate to ascertain the cause of these apparent shifts in timing and/or angle.

### 6.1.1 Venus

The planet Venus was scanned on 2001 March 7 (day 66), and again on 2001 May 15 (day 135). On the first occasion, the solar phase was ~15%, and the distance was $51.7 \times 10^6$ km. For the May 15 scan, the solar phase was ~34%, and the distance was $76.3 \times 10^6$ km. The Pan images from those scans are shown in Figure 73.
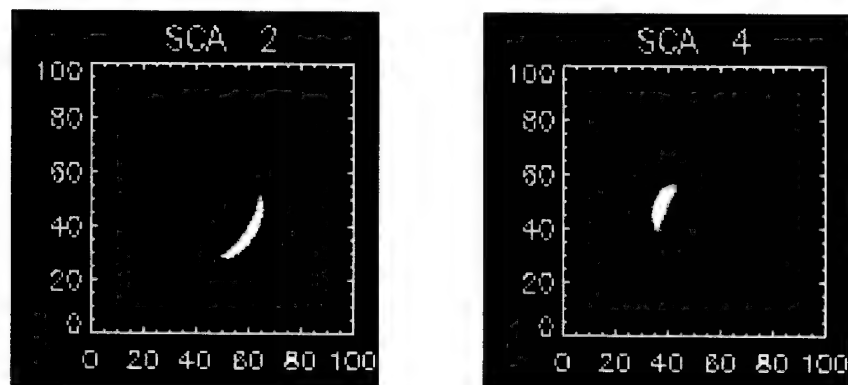
*Figure 73. Pan images of Venus from the scans of 2001 March 7 (left) and 2001 May 15 (right). Axis labels are in pixel units of 5 μrad per pixel. North is at the top, RA increases to the left.*

## 6.1.2 Jupiter and Saturn

Jupiter and Saturn were scanned on 2001 March 14. The re-sampled images of those planets are presented in Figure 74 and Figure 75. Both planets were scanned with SCA 2. The images are too small to show color features in the multispectral bands.
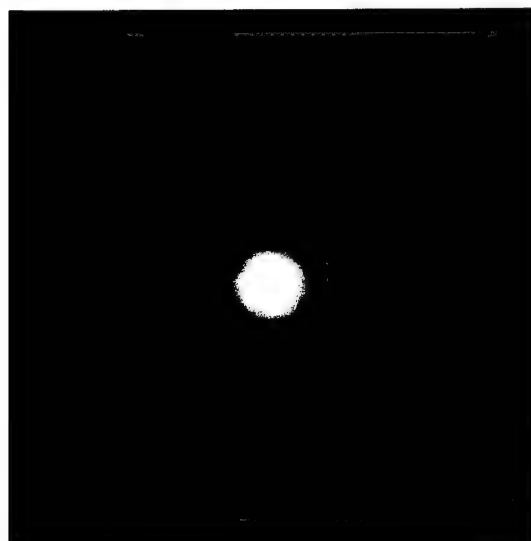
*Figure 74. Pan image of Jupiter (100x100 pixels, at 10 µrad /pixel), printed at the same angular scale as Figure 73.*
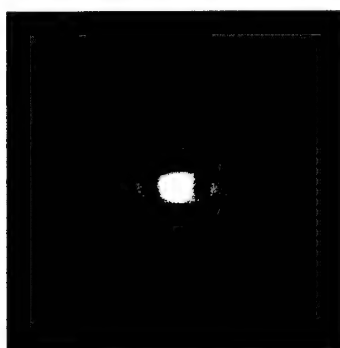


*Figure 75. Pan image of Saturn (64x64 pixels, at 10 µrad /pixel), printed at the same angular scale as Figure 73.*

95

## 6.2 STARS

Stars offer excellent point sources of light that in principle could be scanned to delineate the point-spread function (PSF) of an orbiting instrument. Several scans of stars have been performed with the ALI for this purpose, in the same manner as the planetary scans. Since the scans simply crossed the stars in the normal push-broom direction, the stars are under-sampled in the cross-track direction. However in the in-track direction, over-sampling was accomplished by using a slower than normal angular scan speed.

### 6.2.1 Pleiades

Shortly after the scans of Jupiter and Saturn on 2001 March 14, the Pleiades were scanned. All three targets were in the same part of the sky at the time. The star cluster image overlapped both SCA 2 and SCA 3. Initial attempts to form a reconstructed image of the Pleiades were disappointing. The stars produce relatively faint signals in the ALI, and they occur in very few pixels. A successful approach to the analysis of this scan was to find and fit the star signals in the level 1R data as follows: For each detector, the signal was convolved with a matched filter constructed from the calibrated spatial point-spread function (PSF) and the known scan speed. Peaks significantly above background were then correlated with those from neighboring detectors to identify bright objects. The positions (RA and Dec) and intensities of the bright objects in each band were then fitted, using the PSF and the telemetry data. Ten bright objects were detected in this way, one appearing in both SCA's. At the time of this analysis, our understanding of the ALI alignment with the attitude control system (ACS) was very incomplete. The various bright objects detected were identified as follows: The positions of the objects were roughly reconstructed in a projected image space based on the ACS telemetry and the peak detector and frame number of the objects. The known positions of the stars in the vicinity were also plotted in the same image space, using a spreadsheet program. Angular offset and rotation parameters were adjusted in the spreadsheet until the rotated bright objects pattern overlapped the known star positions. The stars so identified with detected objects are listed in TABLE 2.

As a check on radiometric sensitivity, the apparent intensities of the objects in the Pan band were compared with the V magnitudes of the identified stars. Plotting the log of the scaled Pan intensity against the V magnitudes, a straight line was fitted to the data points. An empirical formula was thus derived for a "Pan pseudo-magnitude," that agrees rather well with the actual V magnitudes. A star of V = 0 would have a scaled Pan intensity of 2400. TABLE 2 lists both the V magnitudes and the Pan pseudo-magnitudes of the ten stars. Alcyone is listed for both SCA's. The intensity uncertainties are on the order of 3 intensity units. The agreement between the two sets of magnitudes is remarkably good, considering that the Pan spectral pass-band peaks at ~660 nm, and the astronomical V response peak is at ~550 nm. Thus some of the scatter of the magnitude points could be attributed to differing stellar spectral shapes.

96

**TABLE 2**

**Stars Detected in the Pleiades (Pan band)**

| Star | V magnitude | SCA | Scaled Pan Intensity | Pan Pseudo-magnitude[a] |
|---|---|---|---|---|
| HD 23753 | 5.44 | 2 | 10.77 | 5.87 |
| HD 23923 | 6.17 | 2 | 8.98 | 6.07 |
| Atlas | 3.62 | 2 | 83.34 | 3.65 |
| Merope | 4.18 | 2 | 59.55 | 4.01 |
| Pleione | 5.09 | 2 | 16.77 | 5.39 |
| Alcyone | 2.90 | 2 | 165.85 | 2.90 |
| Alcyone | 2.90 | 3 | 168.98 | 2.88 |
| Electra | 3.70 | 3 | 85.37 | 3.62 |
| Celæno | 5.46 | 3 | 17.65 | 5.33 |
| Maia | 3.87 | 3 | 67.19 | 3.88 |
| Taygeta | 4.30 | 3 | 41.30 | 4.41 |

[a] Pan pseudo-magnitude = $2.5*\log_{10}(2400/Pan\_intensity)$

### 6.2.2   Vega

The star Vega ($\alpha$ Lyrae, type A0 v, $m_v = 0.03$) was scanned on 2001 May 15. The star image crossed SCA 4, again at one-fourth of the normal angular speed. The star was detected in all bands. In TABLE 3, the intensities of the star in each band are listed, along with the detector and frame numbers closest to the fitted peak location. The column headed "scaled intensity" lists the peak responses fitted with a point-spread function to the radiometrically-calibrated data. The spectral irradiances listed in the last column were obtained from the scaled intensities by multiplying by the respective detector solid angles and dividing by the scaling factor in the radiometric data (300). These spectral irradiances could be compared with the observed spectrum of the star by convolving it with the spectral response functions of the ALI bands, but that is beyond the scope of this report.

## TABLE 3

### ALI Detections of Vega, by Band

| Band | Detector (within SCA 4) | Frame | Scaled Intensity | Irradiance x $10^{12}$ (mW/cm^2 μm) |
|---|---|---|---|---|
| 1' | 252 | 2903.0 | 528.33 ± 2.54 | 3170.3 ± 15.2 |
| 1 | 252 | 2987.0 | 534.92 ± 0.17 | 3209.8 ± 1.0 |
| 2[a] | ~~252~~ | ~~3072.0~~ | ~~138.92 ± 2.39~~ | — |
| 3 | 251 | 3148.0 | 230.81 ± 1.20 | 1385.0 ± 7.2 |
| 4 | 251 | 3233.0 | 142.30 ± 0.05 | 853.9 ± 0.3 |
| 4' | 251 | 3317.0 | 103.72 ± 0.41 | 622.4 ± 2.5 |
| 5' | 250 | 3419.0 | 43.85 ± 1.17 | 263.1 ± 7.0 |
| 5 | 250 | 3503.0 | 16.37 ± 0.05 | 98.2 ± 0.3 |
| 7 | 250 | 3588.0 | 3.00 ± 0.00 | 18.0 ± 0.5 |
| Pan | 759 | 8252.0 | 1942.50 ± 0.40 | 1269.4 ± 0.3 |

[a] Intensity not valid, on account of leaky pixel algorithm applied.

Vega provided a very clear signal in the ALI detectors, enabling us to compare the signal profiles to the calibrated PSF's. The data for band 4 are shown in Figure 76. The abscissas are distance at the focal plane. The cross symbols are the radiometrically-calibrated detector readings. The in-scan PSF plot shows data from a single detector, and the cross-scan PSF shows data from a single frame. The solid curves are the corresponding slices through the PSF derived during pre-flight calibration. Barely visible in Figure 76 are dotted curves representing the maximum profiles of the PSF. It can be seen that at least for band 4, the data match the calibrated PSF very well.
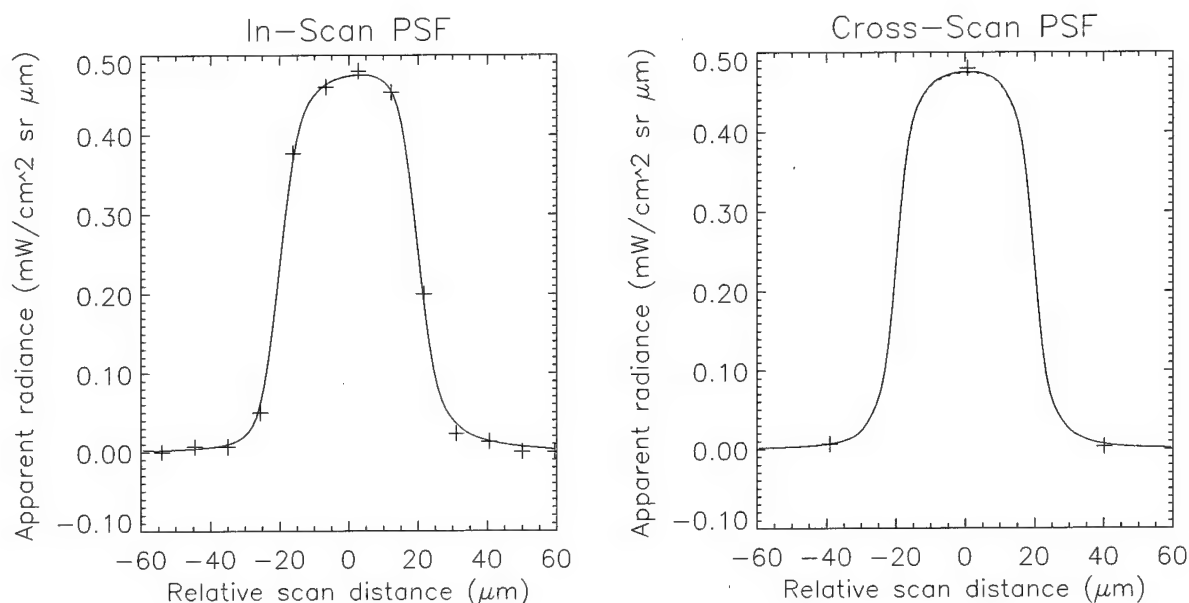
*Figure 76. Profile of Vega spatial response in Band 4.*

A similar fit to the calibrated PSF was done for the Panchromatic band. Here the PSF is less dominated by the detector size, and the optical point-spread is more significant. Figure 77 shows a fit. The PSF used here is not quite the same as the general Pan PSF from the published calibration data [3]. It was initially found that the data points show a *narrower* point spread than expected from the nominal pre-flight PSF. A specific Pan PSF was re-calculated for the SCA and detector crossed by Vega, but with the focus-error term set to zero. A noticeably better fit to the data was thus obtained, as shown in Figure 77. (At present, we lack an explanation for the small excess "tail" of the PSF seen in the in-track plot.) It appears that the instrument is in perfect focus, at least for SCA 4, and the pre-flight calibration data are sufficient to describe the on-orbit spatial response.
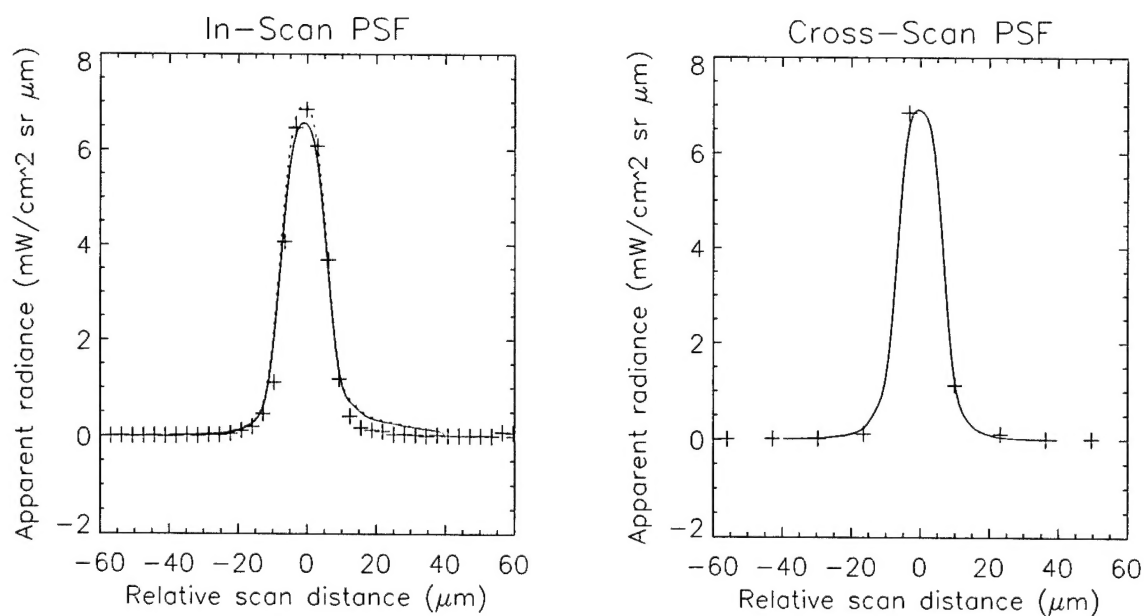
*Figure 77. Profile of Vega spatial response in Pan Band.*

### 6.2.3 Rasalhague

A further scan was done over the star Rasalhague. Those data could be analyzed as was done for Vega, if interest warrants. However, we consider the foregoing results sufficient to conclude the present study of the ALI imaging performance.

# 7. CONCLUSIONS

Upon close examination of the system-corrected reconstructed images presented in Section 3, we conclude that the correction is very accurate, to better than one pixel pitch. This applies to both band-to-band and SCA-to-SCA registration. The absence of visible seams between SCA swaths, even though the SCA sub-images were simply abutted, shows consistent radiometric calibration across the focal plane, as well as geometric precision. We also conclude that the LOS calibration technique produced good results. The attitude control of the spacecraft was very steady, since a simple reconstruction that assumes constant image velocity works well.

Our technique developed to use the 10-m Panchromatic data for sharpening multispectral images appears very promising. The natural-color images appear to have been acquired in the blue, green, and red bands by native 10 m sampling, rather than the actual 30 m. This result is probably due to the fact that the Pan band largely overlaps bands 1, 2, and 3, so it is a good proxy for the total radiance within those bands.

Profiles of bridges (Section 4) and the lunar limb (Section 5.2) show that the spatial resolution of the Advanced Land Imager is at least as good as expected. The measured profiles from on-orbit imaging match the shapes predicted from the pre-flight calibrations, down to the few-percent level. We are gratified that not only did the pre-flight MTF calibration technique work well, but that there appears to be no significant error in the (permanently fixed) focus of the instrument. The point-spread functions seen in stellar scans suggest that some parts of the focal plane have somewhat better spatial resolution than the average represented by the spatial transfer function (STF) calibration file [3]. These statements do not apply however, to the period of late December 2000 to January 5, 2001, when the focal plane was seriously contaminated.

The lunar limb profiles do reveal that the pre-flight STF calibration file does not account for weak "tail" of the observed edge-spread functions, presumably caused by optical scatter from the mirror surfaces. This effect was not modeled as part of the STF calculation. It would have been very difficult to measure it during the system-level pre-flight calibration. More serious are the weak "ghost" images seen in the SWIR bands and band 1'. While the exact mechanism for these ghosts is not clear, we do know that the SWIR ghost originates at the boundary between the VNIR and SWIR filters above the focal plane. For future systems, careful testing of focal plane modules with focused light may catch such problems while they can still be corrected. We strongly recommend the use of lunar scans to validate the edge-spread functions on-orbit.

In total, we believe that the ability of the Advanced Land Imager to acquire images of high quality has been amply demonstrated.

101

# GLOSSARY

ACS. Attitude Control System
ALI. Advanced Land Imager
DCE. Data Collection Event
Dec. declination
DN. digital number
DOF. degrees of freedom
DSTF. dynamic spatial transfer function
EO-1. Earth Observing–1
GSD. ground-sampling distance
GSFC. Goddard Space Flight Center
HDF. Hierarchical Data Format
HSV. hue, saturation, value
IDL. Interactive Data Language
JPEG. Joint Photographic Experts Group
LOS. line of sight
LSF. line-spread function
LUPI. laser unequal-path interferometer
MS. multispectral
MTF. modulation transfer function
Pan. panchromatic
PSF. point-spread function
RA. right ascension
RGB. red-green-blue
ROI. region of interest
SCA. sensor chip assembly
STF. spatial transfer function
SWIR. short-wave infrared
TIFF. Tagged-Image File Format
VNIR. visible/near infrared
WFE. wavefront error

# REFERENCES

1. W. E. Bicknell, C. J. Digenis, S. E. Forman and D. E. Lencioni, "EO-1 Advanced Land Imager," *SPIE Conference on Earth Observing Systems IV*, Denver, Colorado, Proc. SPIE, Vol. 3750, pp. 80-88, July 1999.

2. J. A. Mendenhall (Editor), "Earth Observing-1 Advanced Land Imager: Instrument and Flight Operations Overview," MIT/LL Project Report EO-1-1, 23 June 2000.

3. D. R. Hearn, "EO-1 Advanced Land Imager Modulation Transfer Functions," *MIT Lincoln Laboratory Technical Report 1061*, 22 March 2000.

4. D. R. Hearn, "Earth Observing-1 Advanced Land Imager: Detector Line-of-Sight Calibration," MIT/LL Project Report EO-1-4, 29 December 2000.

5. B. C. Willard, "Wide field-of-view Schmidt-sphere imaging collimator," *SPIE Conference on Earth Observing Systems IV*, Denver, Colorado, Proc. SPIE, Vol. 3750, pp. 286-296, July 1999.

6. J. A. Mendenhall, D. E. Lencioni and J. B. Evans, "Earth Observing-1 Advanced Land Imager: Radiometric Response Calibration," MIT/LL Project Report EO-1-3, 29 November 2000.

7. J. A. Mendenhall, C. F. Bruce, C. J. Digenis, D. R. Hearn, and D. E. Lencioni, "EO-1 Advanced Land Imager Technology Validation Report", MIT/LL Project Report EO-1-9, 4 June 2002.

8. S. Campbell, J. Lovell, D.L.B. Jupp, R. D. Graetz, P. S. Barry, P. Jarecke, and J. Pearman, "The Lake Frome Field Campaign in Support of Hyperion Instrument Calibration and Validation," IEEE 2001 International Geoscience and Remote Sensing Symposium, Sydney, Australia, 2001.

9. Storey, James C., "Landsat 7 on-orbit modulation transfer function estimation," Proc. SPIE Vol. 4540, p. 50-61, Sensors, Systems, and Next-Generation Satellites V, Hiroyuki, Fujisada; Joan B. Lurie; Konradin Weber; Eds. (Toulouse, France), 2001.

10. Kieffer, H. H, and Anderson, J. A., "Use of the Moon for spacecraft calibration over 350-2500 nm, Proc. SPIE, 2438, 325-335, 1998.